# Measurements of Neutral Multi-boson Production in Proton-Proton Collisions at $\sqrt{s} = 13$ TeV with the ATLAS Detector

**Daniel James Lewis**

*Thesis submitted for the degree of Doctor of Philosophy*


Particle Physics Group,
School of Physics and Astronomy,
University of Birmingham.

*May 4, 2022*

UNIVERSITY OF
BIRMINGHAM

## University of Birmingham Research Archive

### e-theses repository

This unpublished thesis/dissertation is copyright of the author and/or third parties. The intellectual property rights of the author or third parties in respect of this work are as defined by The Copyright Designs and Patents Act 1988 or as modified by any successor legislation.

Any use made of information contained in this thesis/dissertation must be in accordance with that legislation and must be properly acknowledged. Further distribution or reproduction in any format is prohibited without the permission of the copyright holder.

# ABSTRACT

Cross-section measurements for the production of a $Z$ boson in association with one or two photons are performed using proton-proton collisions at a centre-of-mass energy of 13 TeV. The data used correspond to an integrated luminosity of 139 fb$^{-1}$ recorded by the ATLAS experiment. The measurements are performed using the leptonic decay channels of the $Z$, and in a phase space region where the dominant photon production is from the incoming proton constituents, rather than off the leptons from the $Z$ decay. The integrated fiducial cross-sections are measured to a precision of 3% and 12% for $Z\gamma$ and $Z\gamma\gamma$ respectively, making these the most precise measurements of these processes to date. The cross-sections are also measured differentially and are compared to predictions from state-of-the-art theoretical calculations and Monte Carlo generators.

# DECLARATION OF AUTHOR'S CONTRIBUTION

The work presented in this thesis would not have been possible without the thousands of scientists, engineers and support staff whose outstanding efforts resulted in the design, construction and operation of the Large Hadron Collider and the ATLAS detector.

Chapter 1 provides a theoretical background to the physics processes studied in this thesis. Chapter 2 gives an overview of the experimental setup used to perform the measurements presented in the later chapters.

Chapter 3 is a description of technical work related to the calibration and data quality monitoring of the ATLAS semiconductor tracker (SCT). The two web displays explained in this chapter were largely the work of the author, with support and feedback from various members of the SCT group. The descriptions of the calibration tests and hit efficiency measurements are included for context and were not a result of the author's work.

Chapter 4 covers many techniques and information relevant to the two analyses described in the following two chapters. Sections 4.1 and 4.2 describe the triggering and object reconstruction used, both of which are a result of hard work from many members of the ATLAS collaboration. The remainder of this chapter provides an introduction to techniques which are well established within the field of particle physics.

The $pp \to Z\gamma$ analysis described in Chapter 5 was a collaborative effort by a small group of physicists from the Universities of Birmingham, Cambridge and the DESY Laboratory in Hamburg. The author's contribution to the analysis was primarily related to the studies of photon isolation, and these are explained in Section 5.3. The author also contributed to the estimation of the pile-up background, specifically

the calculation of the normalisation of the signal leakage into the pile-up enriched control region.

The $pp \to Z\gamma\gamma$ analysis described in Chapter 6 was almost entirely the work of the author, within an analysis team formed from the same institutions as for the $Z\gamma$ analysis together with the University of Heidelberg. The author was responsible for the optimisation of the selections (except for the trigger definitions and selections related to this), the estimation of all the background processes and their associated uncertainties, the operation of the unfolding procedure, and the propagation of the systematic uncertainties. The author produced the final cross-section measurement results, and was responsible for producing the truth-level Monte Carlo predictions for comparison to the data.

During data-taking, a team of operators monitor the various ATLAS subsystems in the ATLAS control room. The author was responsible for overseeing the inner detector subsystems during multiple runs in 2018, which amounts to a small fraction of the data analysed in this thesis. This involved monitoring the condition, readout and recorded data quality of the subsystems, as well as performing calibrations during the times when there was no beam.

# ACKNOWLEDGEMENTS

"Avoid particle physics like the plague!" was fortunately the one piece of advice from my A-level physics teachers that I chose to ignore. Little did they know that they had a huge part in inspiring me to set my sights on achieving a PhD in particle physics. It is very surreal to finally be here 10 years later, especially considering that it still felt a long way away even up until a few months ago. My experience at Birmingham has lived up to all my expectations and I am proud of what I have achieved, but it would not have been possible without the people listed below.

First and foremost I would like to thank Dave. Your enthusiasm for physics and dedication to research has been a constant source of inspiration for me throughout these four years. Thank you for your guidance and for always making time for me. Thanks also to everyone else in the Birmingham ATLAS group for your support and insights, especially to Chris who provided me with such thorough feedback on this thesis.

Thank you to the British taxpayer, via the STFC, and the School for providing the funds to carry out this research.

It has been a pleasure to work with Yee, Ruchi, Philipp, Beate and Richard from the $Z\gamma(\gamma)$ analysis teams; such a talented and friendly group of people, whose help was of course invaluable for the work presented in this thesis.

I am very fortunate to have made two exceptional friends during my PhD, but it seemed destined to be that way when I walked into the office on my first day to find two other vegetarian drummers. Gov, thanks for the constant supply of memes, and thanks for putting up with my neediness. Nandish, thanks for letting us call you Crispy and thanks for putting up with living with me for two years. It's impossible to write down all the great memories we made, but maybe that's just because we

spent all of our time together.

Thank you to all the hammer-legends who I shared various offices with for creating such stimulating and enjoyable working environments. A special thanks goes to Andy and Jamés, who took me under their wing from day one and gave me lessons in all things ranging from emacs to 'Slap the Bag'. I hope I have returned the favour somewhat by continuing the dominance of the Birmingham team in the Bubble Chambers football tournament. To the rest of you: Briglin, Kendrick, Elliot, Jack, Rob, Russell, Al, Robbie, Jonathan and Patrick, thank you all for the good times in and out of the office (e.g. Sporcle quizzes and curries at The Dilshad, respectively).

The highlight of my PhD was spending a year or so based at CERN. I greatly enjoyed doing shifts in the ATLAS control room, even when being attacked by a wasp in front of a group of tourists. I also thoroughly enjoyed working with the SCT team, particularly Dave R, Hide, Shigeki and Naoki, who helped me greatly with the work presented in Chapter 3. I also made some great friends whilst out at CERN. Thanks to Gio, Tan and Martin for the ski trips, football, beers and other adventures. And thank you to Lyla for being so caring and supportive over the last few years.

To my dearest Dreamland XL friends: Stewart, Liam, Jodie, Katie and Harry, thank you for nurturing me out of my tricky teenage years. Some of my favourite times over the course of the PhD have been when we've had our semi-regular meet-ups. And to some of my oldest friends: Tim, Hannah, Adam and Jonty, thanks for sticking by me all this time.

To Mum, Dad, Becky, Louis and Uncle Ian, this thesis is dedicated to all of you. I hope I have done you proud and I love you all so much.

*What we see before us is just one tiny part of the world. We get into the habit of thinking, this is the world, but that's not true at all. The real world is in a much darker and deeper place than this, and most of it is occupied by jellyfish and things.*

- Haruki Murakami, The Wind-Up Bird Chronicle

# Contents

# List of Tables

# List of Figures

# DEFINITIONS OF ACRONYMS

**AOD** Analysis Object Data

**aQGC** Anomalous Quartic Gauge Coupling

**aTGC** Anomalous Triple Gauge Coupling

**ATLAS** A Toroidal LHC ApparatuS

**BOC** Back Of Crate

**CERN** European Organisation for Nuclear Research

**CR** Control Region

**CSC** Cathode Strip Chambers

**CTP** Central Trigger Processor

**DAQ** Data AcQuisition

**DQ** Data Quality

**EFT** Effective Field Theory

**ENC** Equivalent Noise Charge

**EM** Electromagnetic

**EWSB** Electroweak Symmetry Breaking

**EW** Electroweak

**FCal** Forward Calorimeter

**FSR** Final State Radiation

**HL-LHC** High Luminosity Large Hadron Collider

**HLT** High Level Trigger

**HV** High Voltage

**IBL** Insertable Beam Layer

**ID** Inner Detector

**IP** Interaction Point

**ISR** Initial State Radiation

**LAr** Liquid Argon

**LHC** Large Hadron Collider

**LO** Leading order

**LUCID** Luminosity measurements Using Cherenkov Integrating Detector

**L1** Level 1

**MC** Monte Carlo

**MDT** Monitored Drift Tubes

**ME** Matrix Element

**MS** Muon Spectrometer

**NLO** Next-to-leading order

**NNLO** Next-to-next-to-leading order

**QCD** Quantum Chromodynamics

**QED** Quantum Electrodynamics

**QFT** Quantum Field Theory

**PAT** Performance Analysis Tool

**PDF** Parton distribution function

**PS** Parton Shower

**PV** Primary Vertex

**ROD** Readout Driver

**RoI** Region of Interest

**RPC** Resistive Plate Chambers

**SCT** SemiConductor Tracker

**SM** Standard Model

**SR** Signal Region

**SUC** Sensor Under Consideration

**TGC** Thin Gap Chambers

**ToT** Time over Threshold

**TRT** Transition Radiation Tracker

**VBS** Vector Boson Scattering

# Introduction

Particle physics has long been at the forefront of humanity's quest into understanding the nature of the universe. The experiments conducted in this field are continually pushing the exploration of smaller length scales and higher energy scales. At these scales, the particles being investigated are considered to be fundamental, and the interactions between them are the simplest manifestation of the forces that drive everything we observe in the macroscopic universe (with the exception of gravity). The Standard Model (SM) of particle physics describes the properties and interactions of all known fundamental particles and is arguably the most rigorously tested scientific theory of all time.

Over the last century, predictions of the SM have been confirmed by a multitude of experiments, not only in terms of describing the interactions of particles but also by predicting new particles before they are able to be observed. Despite this there are still unexplained inconsistencies, such as dark matter, baryon-antibaryon asymmetry and the aforementioned gravity problem, which show that the SM is not a complete theory. Because of this, the field is as active as ever as the SM is tested to higher levels of precision and searches are performed for new physics signals.

One category of particle physics experiments is known as collider experiments, which consists of accelerators and detectors. Two beams of particles, travelling in opposite directions, are accelerated to a desired energy by the accelerators. The two beams are then brought together at specific points where the particles in each beam collide with each other. The detectors are placed around the collision points in order to measure any particles produced in the collisions. The colliders are described in terms of their centre-of-mass energy ($\sqrt{s}$) which corresponds to the maximum energy available in each collision. The higher the value of $\sqrt{s}$ the more energy is available to produce more or heavier particles.

In 2008, the most recent hadronic collider experiment began operation and it consists of the Large Hadron Collider (LHC) and four main detectors: ATLAS, CMS, LHCb and ALICE. The LHC accelerates two beams of hadrons, typically protons, and collides them within the four detectors. At the time of writing the LHC has operated at $\sqrt{s} = 13$ TeV which is an order of magnitude higher than any previous collider. Due to advancements in detector technology, the LHC is also able to operate at a much higher rate than any previous collider, which allows much larger datasets to be collected by the experiments. The larger dataset facilitates some of the most precise tests of processes predicted by the SM as the regime is entered where statistical uncertainties become subdominant to the systematic uncertainties related to the experiment itself. The higher rates also allow for much rarer processes to be measured for the first time as the dataset is now large enough to contain processes with extremely low production rates. The higher energy potentially allows for contributions from new physics processes to be produced, which have been inaccessible at previous lower-energy colliders.

The measurements of electroweak processes at the LHC provide excellent tests of the SM. Such processes are reasonably well understood from a theoretical perspective but may provide interesting insights due to their intrinsic connection to non-Abelian couplings, electroweak symmetry breaking and the Higgs. Such measurements can be used to test state-of-the-art SM predictions and also used to constrain new physics models. Additionally, a good understanding of these processes is necessary when

searching for rarer or forbidden processes which would leave the same signal in the detector.

In this thesis, the measurements of two electroweak processes are explored, the first being the production of a $Z$ boson and a photon ($pp \to Z\gamma + X$) and the second, the production of a $Z$ boson and two photons ($pp \to Z\gamma\gamma + X$). Both measurements are made using proton-proton collisions at $\sqrt{s} = 13$ TeV with the ATLAS detector. An overview of the SM and an introduction to the theory that describes these two processes, is presented in Chapter 1 along with a discussion of previous experimental results. The ATLAS detector is described in Chapter 2 and the author's contribution to the operation of one of its subdetectors is detailed in Chapter 3. The details and techniques common to both measurements are given in Chapter 4. The methods used to perform the measurements of $pp \to Z\gamma + X$ and $pp \to Z\gamma\gamma + X$, and the results, are described in Chapters 5 and 6 respectively.

# CHAPTER 1

# Theoretical Overview and Status of Experimental Results

## 1.1 The Standard Model

The following sections (1.1 and 1.2) provide an overview of the Standard Model, with an emphasis on the areas most relevant to the processes studied in this thesis. A more complete description can be found in Reference [1].

Fundamental particles are distinguished by their observable properties, e.g. mass, and quantum numbers. A quantum number is a discrete value that describes a property of a particle, an example of which is spin, which is a measure of intrinsic angular momentum. Spin divides the complete set of SM particles into fermions which have half-integer spin values and bosons which have integer spin values, in units of Planck's constant $\hbar$. The fermions listed in Table 1.1 are further divided into quarks, which have fractional values of electric charge, and leptons which have integer values, in units of the elementary charge $e$. The quarks come in three families

of increasing mass: up/down, charm/strange and top/bottom. The leptons also have three families of increasing mass with each family consisting of an 'electron-like' particle with charge of $-1$ and an associated uncharged neutrino. All fermions have antiparticle partners which have quantum numbers of the same magnitude, but for some, the sign is inverted with respect to the original particle. For example, the positively-charged positron is the antiparticle of the electron.

| Fermion | EM Charge [e] | Mass [GeV] |
|---|---|---|
| $u$, $d$ | $+2/3$, $-1/3$ | $2.16^{+0.49}_{-0.26}\times10^{-3}$, $4.67^{+0.48}_{-0.17}\times10^{-3}$ |
| $c$, $s$ | $+2/3$, $-1/3$ | $1.27\pm0.02$, $9.3^{+1.1}_{-0.5}\times10^{-2}$ |
| $t$, $b$ | $+2/3$, $-1/3$ | $172.9\pm0.4$, $4.18^{+0.03}_{-0.02}$ |
| $e$, $\nu_e$ | $-1$, $0$ | $5.109989461\pm0.000000031\times10^{-4}$, $< 1.1\times10^{-9}$ |
| $\mu$, $\nu_\mu$ | $-1$, $0$ | $1.056583745\pm0.000000024\times10^{-1}$, $< 1.1\times10^{-9}$ |
| $\tau$, $\nu_\tau$ | $-1$, $0$ | $1.77686\pm0.00012$, $< 1.1\times10^{-9}$ |

Table 1.1: A summary of the charge and mass of all the Standard Model fermions. Values taken from Reference [2].

There are five types of fundamental boson particles in the SM; they are listed along with their basic properties in Table 1.2. The bosons are able to couple to other particles if they possess a certain type of property. The photon ($\gamma$) is a massless particle that propagates the electromagnetic (EM) interaction by coupling to particles with electric charge. A simple example of an electromagnetic interaction is bremsstrahlung radiation where a decelerating electron emits a photon: $e \rightarrow e\gamma$. The strength of an interaction is parameterised by a coupling parameter, which is an important factor when calculating the rate at which a particular process occurs. The coupling strength of the EM interaction is given by the fine structure constant, $\alpha$.

The $W^{\pm}$ and $Z$ bosons have mass and propagate the weak interaction. The weak interaction is responsible for radioactive $\beta$ decay, for example the decay of a neutron to a proton: $n \rightarrow pe\bar{\nu}_e$. The weak bosons couple to particles that carry weak isospin or hypercharge (introduced later in Section 1.2.2), which includes all fermions and the weak bosons themselves. The weak interaction coupling strength is denoted as $\alpha_W$.

The gluons are massless and exist in eight types. They are responsible for propagating the strong interaction between particles that carry colour charge, which are all quarks and the gluons themselves. Colour charge takes three values: red, green or blue, and antiparticles carry analogous anticolour charges: antired, antigreen or antiblue. The strong force keeps quarks bound in colourless combinations called hadrons. The first type of hadron is a combination of a quark and an antiquark, named a meson. Combinations of three quarks are called baryons, examples of which are the proton and neutron. Hadrons must be colourless (colour singlets), which means that mesons are formed of a colour-anticolour pair of quarks, and baryons are made of three quarks with different colours. The strong interaction coupling strength is denoted as $\alpha_s$.

The final boson in the SM is the Higgs boson which does not propagate a force but arises from electroweak symmetry breaking and in doing so provides the mechanism that gives rise to particle mass terms. The Higgs couples to all particles which have mass, and the stronger the coupling, the greater the mass. This is described in more detail in Section 1.2.3, where it is seen that the Higgs couplings to massive vector bosons arise naturally. Higgs couplings to massive fermions are added by hand and are referred to as Yukawa couplings.

| Boson | EM Charge [e] | Mass [GeV] | Spin [$\hbar$] | Coupling |
|---|---|---|---|---|
| $\gamma$ | 0 | 0 | 1 | Electromagnetic ($\alpha$) |
| $Z^0$ | 0 | 91.1876±0.0021 | 1 | Weak ($\alpha_W$) |
| $W^{\pm}$ | ±1 | 80.379±0.012 | 1 | Weak ($\alpha_W$) |
| $g$ | 0 | 0 | 1 | Strong ($\alpha_s$) |
| $H$ | 0 | 125.25±0.17 | 0 | Vector boson/Yukawa ($v$) |

Table 1.2: A summary of the basic properties of all the Standard Model bosons. Values taken from Reference [2].

## 1.2 Quantum field theory (QFT)

The mathematical framework behind the SM relies on treating particles as excitations of fields. The interactions between particle fields are also described by fields themselves. A key concept for understanding the interactions described by the SM is Noether's theorem, which states that "For every continuous symmetry of a system, there exists a corresponding conserved quantity". This applies to classical systems as we observe that invariance with respect to translational, temporal and rotational transformations correspond to the conservation of momentum, energy and angular momentum respectively. By investigating symmetries of fields under certain transformations, the conserved quantities and nature of the different interactions in the SM can be derived.

### 1.2.1 Quantum electrodynamics (QED)

A simple example of a QFT is the investigation of fermion fields, represented by $\psi$, under U(1) gauge transformations. The U(1) symmetry group corresponds to a complete set of rotations which take the form $e^{i\rho(x)}$ where $\rho(x)$ is the phase of the rotation and $x$ is any point in space-time. The fermion fields therefore transform as:

$$\psi \rightarrow e^{i\rho(x)}\psi. \tag{1.1}$$

The transformation can vary at any point in space-time, and hence this is a local gauge transformation. Here it is appropriate to introduce the Lagrangian formalism. The Lagrangian of a system is the difference between its kinetic and potential energy, and the equations of motion for the system can be calculated from it using the Euler-Lagrange equations. In QFT, the Lagrangian density ($\mathcal{L}$) is used, from which the Lagrangian can be calculated by integrating over all space. The Lagrangian density can be split into different terms which describe different aspects of the kinematics,

e.g.

$$\mathcal{L} = \mathcal{L}_{kinetic} + \mathcal{L}_{mass} + \mathcal{L}_{interaction}. \tag{1.2}$$

The Lagrangian for a fermion is described by the Dirac form

$$\mathcal{L} = \bar{\psi}(i\gamma^{\mu}\partial_{\mu} - m)\psi, \tag{1.3}$$

where $\gamma^{\mu}$ are the set of matrices which account for fermion spin. This simply describes a freely propagating fermion as it only contains kinetic ($\bar{\psi}\gamma^{\mu}\partial_{\mu}\psi$) and mass ($m\bar{\psi}\psi$) terms. However, this Lagrangian is not invariant under local gauge transformations due to the derivative of the locally-dependent phase $\rho(x)$. To force invariance it is necessary to modify the derivative to

$$\partial_{\mu} \rightarrow \partial_{\mu} - i\alpha A_{\mu}. \tag{1.4}$$

This introduces a vector field $A_{\mu}$. The additional term which arises in the Lagrangian due to this modification describes the interaction between the fermion fields and this vector field, which has an associated coupling strength $\alpha$. The vector field is also required to transform, in order to ensure gauge invariance, as:

$$A_{\mu} \rightarrow A_{\mu} + \frac{1}{\alpha}\partial_{\mu}\rho(x). \tag{1.5}$$

An additional gauge invariant term for the propagation of the vector field is also added to the Lagrangian using the field strength tensor $F_{\mu\nu}$. The form of this field strength tensor, the vector field, and its conserved current, is analogous to that of electrodynamics. In this context, the vector field can be interpreted as a photon and hence the conserved quantity in this gauge theory can be attributed to electric charge. This is therefore an example of how forcing local gauge invariance introduces a gauge field ($A_{\mu}$) which represents an interaction (electromagnetic) that has an associated conserved quantity (electric charge).

It is useful to represent these interactions between fermions and photons using Feynman notation, which serves as a visual representation of the interaction and also as

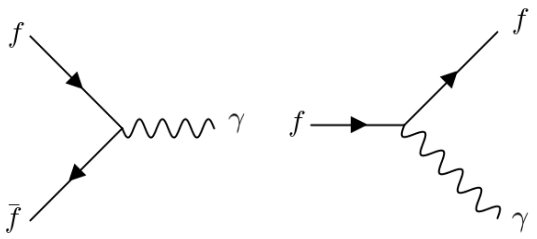


(a) (b)

Figure 1.1: Examples of QED interaction vertices.

a mathematical tool used to calculate the probability for a particular interaction to occur. Examples of the QED vertices are given in Figure 1.1, where the annihilation of two fermions into a photon and the radiation of a photon off a fermion can be seen. Both of these interactions have the same QED coupling strength of $\alpha$.

### 1.2.2 Electroweak physics

Electroweak (EW) theory is described by invariance under $\mathrm{SU}(2)_L \otimes \mathrm{U}(1)_Y$ transformations. The combination of the two groups manifests itself physically as the unification of the electromagnetic and weak forces. The index $L$ indicates that the SU(2) sector of this interaction couples only to left-handed chiral fermions. The $Y$ index refers to weak hypercharge, which is related to the electric charge ($Q$) in QED by the relationship $Q = T_z + \frac{Y}{2}$, where $T_z$ is the third component of weak isospin, which is the conserved quantity in weak interactions.

Requiring local gauge invariance with respect to $\mathrm{SU}(2)_L \otimes \mathrm{U}(1)_Y$ transformations produces a complete theory of electroweak physics, except it predicts massless gauge bosons which is not what is seen in nature. In order for the gauge bosons to have mass, the electroweak symmetry must be broken. To demonstrate this, a doublet of complex scalar fields ($\phi$) is considered under a local $\mathrm{SU}(2)_L \otimes \mathrm{U}(1)_Y$ transformation. The doublet has the form

$$\phi = \begin{pmatrix} \phi_1 + i\phi_2 \\ \phi_3 + i\phi_4 \end{pmatrix}. \tag{1.6}$$

The Lagrangian of these fields is given by

$$\mathcal{L} = (\partial_\mu \phi)^\dagger (\partial^\mu \phi) - \mu^2 \phi^\dagger \phi - \lambda (\phi^\dagger \phi)^2, \tag{1.7}$$

where † represents the Hermitian adjoint. Analogous to the QED case, the derivative has to be modified in order to maintain gauge invariance:

$$\partial_\mu \rightarrow D_\mu = \partial_\mu + ig\frac{\tau_a}{2} W_\mu^a + i\frac{g'}{2} B_\mu, \tag{1.8}$$

where $g$ and $g'$ are respectively the weak isospin and weak hypercharge couplings. This introduces three vector gauge fields $W_\mu^a$ $(a = 1, 2, 3)$ corresponding to the weak interaction and $B_\mu$ which corresponds to the electromagnetic interaction. The generators of the SU(2) group are the Pauli spin matrices $(\tau_a)$ which do not commute, making this a non-Abelian interaction. Similarly to the QED case, the fields themselves are also required to transform to ensure gauge invariance. The resulting Lagrangian is as follows:

$$\mathcal{L} = (D_\mu \phi)^\dagger (D_\mu \phi) - V(\phi) - \frac{1}{4} W_{\mu\nu}^a W_a^{\mu\nu} - \frac{1}{4} B_{\mu\nu} B^{\mu\nu}, \tag{1.9}$$

$$V(\phi) = \mu^2 \phi^\dagger \phi + \lambda (\phi^\dagger \phi)^2. \tag{1.10}$$

Analogous to the QED case, the field strength tensors $W_{\mu\nu}^a$ and $B_{\mu\nu}$ are introduced for the weak isospin and weak hypercharge fields, respectively. The Lagrangian contains bosonic self-interaction terms for the fields (contained within $W_{\mu\nu}^a W_a^{\mu\nu}$, which represent the transformed weak gauge fields) due to the non-Abelian nature of the SU(2) group. Examples of the weak interaction vertices predicted by the theory are shown in Figure 1.2. However, the EW Lagrangian does not contain mass terms for the weak bosons which is not what is seen experimentally.

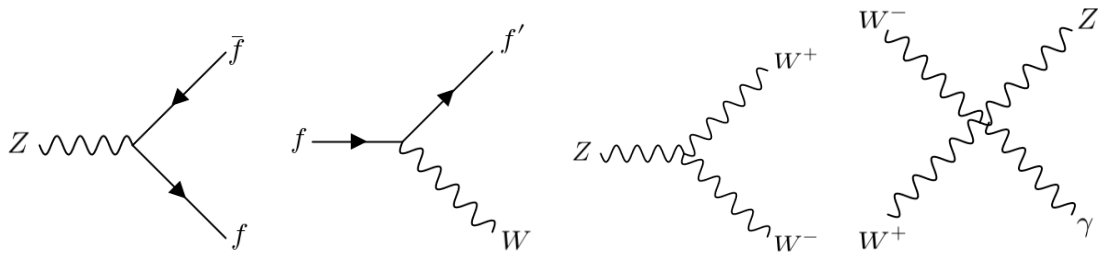


(a) (b) (c) (d)

Figure 1.2: Examples of EW interaction vertices. (a) and (b) are examples of the interaction of fermions with weak gauge bosons. (c) and (d) are examples of the triple and quartic weak boson self-interactions.

### 1.2.3 Electroweak symmetry breaking

To see how the mass terms arise the form of the potential $V(\phi)$ is considered. In the case where $\mu^2 > 0$, the potential has a trivial minimum at $\phi^\dagger\phi = 0$. However, the more interesting case where $\mu^2 < 0$, results in a series of minima satisfied by $\phi^\dagger\phi = -\frac{\mu^2}{2\lambda}$. This means that one can arbitrarily choose any combination of $\phi_i$ which satisfies the minimum requirement, and hence the symmetry is broken as the form of the potential varies depending on which minimum is chosen. A simple solution is to set one of the fields to $v = \sqrt{-\mu^2/\lambda}$, and set the rest of the fields to zero. Expanding about this minimum, the solution for the field is

$$\phi_0 = \frac{1}{\sqrt{2}} \begin{pmatrix} 0 \\ v \end{pmatrix} \tag{1.11}$$

Substituting this solution into the Lagrangian gives rise to mass terms:

$$\left(\frac{vg}{2}\right)^2 W_\mu^+ W^{-\mu} + \frac{v^2}{8}(g^2 + g'^2) Z_\mu Z^\mu + 0(g^2 + g'^2) A_\mu A^\mu. \tag{1.12}$$

This correctly predicts three massive mediators of the weak interaction and one massless mediator of the electromagnetic interaction. The physical bosons are de-

scribed by a combination of the original $\mathrm{SU}(2)_L \otimes \mathrm{U}(1)_Y$ gauge fields:

$$W_\mu^\pm = \frac{1}{\sqrt{2}}(W_\mu^1 \mp iW_\mu^2), \qquad m_W = \frac{vg}{2}, \tag{1.13}$$

$$Z_\mu = \cos(\theta_W)W_\mu^3 - \sin(\theta_W)B_\mu, \qquad m_Z = \frac{m_W}{\cos(\theta_W)}, \tag{1.14}$$

$$A_\mu = \sin(\theta_W)W_\mu^3 + \cos(\theta_W)B_\mu, \qquad m_A = 0, \tag{1.15}$$

where $\theta_W$ is the weak mixing angle, defined as $\tan(\theta_W) = g'/g$. This demonstrates the mixing of the electromagnetic and weak neutral currents.

The non-zero scalar field is known as the Higgs field. Hence it is through interactions with this field that the gauge bosons acquire their mass. The three remaining scalar fields are known as Goldstone bosons which are absorbed by the weak bosons and provide the extra degree of freedom needed for their mass terms. The Higgs field also couples to fermions via Yukawa couplings which are proportional to the mass of the fermion. The discovery of a massive scalar boson, consistent with the SM Higgs boson, was announced by the ATLAS and CMS Collaborations in 2012 [3, 4].

### 1.2.4 Quantum chromodynamics

The strong interaction is described by quantum chromodynamics (QCD), which is responsible for the couplings between quarks and gluons. The theoretical description comes from requiring local gauge invariance under SU(3) transformations which take the form

$$q_j \to e^{i\rho_a(x)\frac{\lambda_a}{2}} q_j, \tag{1.16}$$

where $q_j$ are the quark fields, $j$ is the index for colour charge and $\lambda_a$ are the eight matrices which are the generators of the SU(3) group. These generators do not commute with each other, making this a non-Abelian transformation, i.e.

$$[\lambda_a, \lambda_b] = 2if_{abc}\lambda_c \neq 0 \quad (\text{if } a \neq b), \tag{1.17}$$

where $f_{abc}$ are the structure constants of SU(3). Transformations of this form do not leave the Lagrangian for the quark fields unchanged, therefore the derivative must transform as

$$\partial_\mu \rightarrow \partial_\mu + i\alpha_s \frac{\lambda_a}{2} G^a_\mu. \tag{1.18}$$

There are eight gluon fields $G^a_\mu$, introduced due to the more complex form of the generators $\lambda_a$, which couple to quarks with strength $\alpha_s$. The gluon fields are also required to transform to maintain invariance:

$$G^a_\mu \rightarrow G^a_\mu - \frac{1}{\alpha_s}\partial_\mu \rho_a - f_{abc}\rho_b G^c_\mu. \tag{1.19}$$

The fully expanded QCD Lagrangian contains cubic and quartic terms in $G^a_\mu$ which describe self interactions between gluons. The QCD interaction vertices are summarised in Figure 1.3.

The QCD coupling, $\alpha_s$, varies with the energy scale of the interaction, which is referred to as a running coupling. Colour charged particles constantly emit and absorb virtual $q\bar{q}$ pairs and gluons. The self interaction of these gluons results in the effective coupling strength, at short distance scales or high energy scales, being reduced due to an anti-screening effect.

Strong interactions are well understood within the context of perturbation theory, which starts with the simplest manifestation of a particular process, with the minimum allowed number of QCD vertices, known as leading order (LO). If perturbation theory holds then higher-order corrections to this process, involving more vertices, get progressively smaller. At high energy scales, such as those at the LHC, $\alpha_s \ll 1$ which means that perturbation theory is valid. At low energy scales, this assumption does not hold and QCD is non-perturbative. The coupling strength is a free parameter in the SM, so the value at various scales is extracted from measurements of sensitive variables [5] or through analytical methods such as Lattice QCD [6].

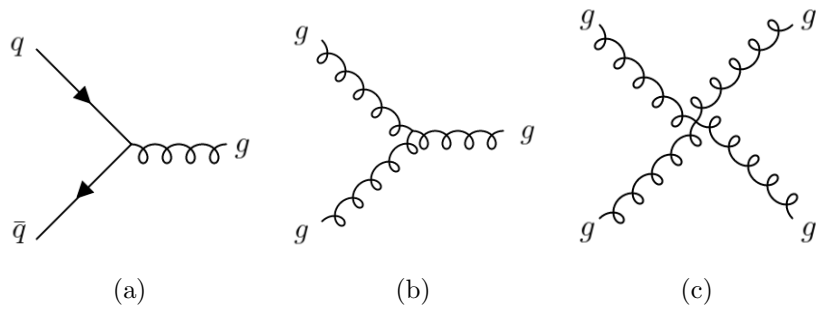


(a) (b) (c)

Figure 1.3: Examples of QCD interaction vertices.

## 1.3 Proton-proton collisions

Due to the fact that protons are composite particles, modelling the collision dynamics for proton-proton interactions is much more complicated than, for example, in an $e^+e^-$ collider where the incident particles are fundamental and point-like. Protons are made up of partons which constitute valence quarks: two up and one down, as well as a sea of gluons and virtual $q\bar{q}$ pairs. The cross-section for the production of a certain set of final-state particles, $X$, from the collision of two protons can be factorised into an integral over the individual partonic cross-sections for the production of the same final state, and parton density distributions. The partonic production cross-sections make up the perturbative hard scattering part of the interaction and can hence be expanded in orders of $\alpha_s$:

$$\sigma_{q_1 q_2 \to X}(\mu_R) = \sigma_0 + \alpha_s(\mu_R)\sigma_1 + \alpha_s^2(\mu_R)\sigma_2 + ... \quad , \tag{1.20}$$

where $q_i$ are partons and the expansion is shown up to next-to-next-to-leading order (NNLO, $\sigma_2$) in $\alpha_s$. The value of $\alpha_s$ in the cross-section is affected by divergences at low energy scales due to the running of the coupling discussed in the previous section. To remove these divergences the coupling is redefined at some understood energy scale $\mu_R$, called the renormalisation scale [7]. The value of the cross-section obtained from a calculation is hence dependent on the choice of $\mu_R$.

The partonic cross-sections are weighted by parton distribution functions (PDFs)

which describe the fraction of the proton energy that a particular parton carries. The length scales of the individual protons are large enough for QCD to be non-perturbative, therefore the PDFs cannot be calculated directly. Instead, the PDFs are inferred by fits to experimental data, an example of which is described in Reference [8]. The PDFs are measured at some energy scale ($\mu_0$), then extrapolated to the desired scale ($\mu_F$), using the perturbative DGLAP equations [9, 10, 11]. $\mu_F$ is the factorisation scale which separates the non-perturbative regime used for the PDFs, and the perturbative regime of the partonic cross-sections.

The cross-section for the production of the final state $X$ from two protons ($p_1$, $p_2$) colliding is therefore given by

$$d\sigma_{p_1p_2\to X} = \int dx_1 dx_2 \sum_{q_1,q_2} f_{q_1}(x_1,\mu_F) f_{q_2}(x_2,\mu_F) d\sigma_{q_1q_2\to X}(x_1x_2s,\mu_F,\mu_R), \quad (1.21)$$

where $x_i$ is the momentum fraction of parton $q_i$ in proton $p_i$, and $f_{q_i}(x_i,Q^2)$ is the PDF at some energy scale $Q^2$.

## 1.4 Standard Model predictions

Using the theoretical input of the SM, processes can be simulated using a number of techniques. These simulations are used by particle physics experiments in order to interpret the measurements performed. The following section covers two techniques used to predict the cross-sections and distributions of particle physics processes: Monte Carlo simulations and fixed-order calculations.

### 1.4.1 Monte Carlo simulations

Monte Carlo (MC) simulation programs are used to generate events which reflect those that are observed in data. The following section outlines the different stages of the generation. A comprehensive overview of MC simulations can be found in

Reference [12].

The first part of the simulation consists of the hard scatter, where the incoming partons are described by the PDFs and the kinematics of the outgoing products are determined by the quantum mechanical matrix element (ME) of the desired process, at a particular order of QCD. Random values of the outgoing particle's momenta are drawn according to the matrix element. When a large enough number of events is produced, the result is an integration over the available incoming energy and the outgoing parton's momenta.

The next stage of the process is referred to as the parton shower (PS) which simulates the propagation of the partons in the interaction. The partons are subject to QCD showering from gluon radiation and splitting as well as the production of $q\bar{q}$ pairs. QED radiation is also included within the PS modelling. The propagation is performed according to a Markov chain algorithm [12], which handles the stepwise probability of a parton to undergo an emission. These emissions increase the number of outgoing particles and hence spread out the available energy and momentum in the interaction. Eventually, the regime is reached where perturbation theory breaks down and the partons can no longer be treated as free particles.

The interplay of the ME and PS becomes complicated when considering higher-order predictions. For example, a next-to-leading order (NLO) ME for a process may include a gluon radiated from an initial-state quark. However, this may lead to double counting, as such processes are also included in the PS. In order to avoid any overlap, MEs are calculated separately for each desired final-state parton multiplicity. Additionally, a momentum scale is set to clearly define which partons are handled by the ME (hard) and which by the PS (soft).

As the non-perturbative regime is reached, the quarks and gluons hadronise to form particles which may decay further or which may be stable enough to go on to interact with the detector. Different models which describe the hadronisation process exist [13, 14] and are based on the observed properties of QCD.

As well as the hard scatter, there are other interactions which occur in proton-proton collisions that must also be simulated in order to provide a fair comparison to data. These softer processes arise from the interactions of other partons within the protons or the protons themselves, and are referred to as the underlying event. At the LHC, the protons are collided in bunches which leads to approximately 30 proton-proton interactions in each bunch crossing on average. Each MC event is overlaid with multiple minimally biased events, i.e. events which best represent the majority of the proton-proton collisions. The MC is then reweighted such that the distribution of the average number of interactions per bunch crossing matches that of the data.

The simulation-level (truth-level) objects are subject to further selection requirements which define a common phase space for comparison to other predictions or with unfolded data (described in Section 4.4.1). The events can be histogrammed to provide distributions for any variables of interest. Also, MC predictions are able to provide a direct comparison to data by passing each event through a detector simulation and reconstruction. This allows the tuning of parameters such as detector response, reconstruction resolutions and selection efficiencies between data and simulation. The ATLAS detector is simulated using the GEANT4 [15] program.

The MC generators used to produce the samples in the analyses detailed in this thesis, at the matrix element level, are Sherpa [16], MadGraph [17] and Powheg [18]. The most precise and commonly available ME accuracy for MC generators is next-to-leading order in QCD. The matrix element level particles are interfaced to a parton shower program. These programs simulate the underlying event, parton shower and hadronisation stages, and are provided by Sherpa [19] and PYTHIA [20].

### 1.4.2 Fixed-order calculations

The second type of predictions that can be used to compare with measurements are direct calculations of cross-sections at a fixed order of QCD. These predictions differ

significantly from MC programs as they provide cross-section calculations only as opposed to being event generators. The calculations are performed at the parton level which avoids the complications related to the PS and hadronisation mentioned above. However, additional corrections are needed to extrapolate to a common phase space for comparison to data. Instead of using the available computing power to generate events, it is instead utilised to perform the calculations at as high an order as possible, which is typically NNLO in QCD for most processes. Although more accurate than MC generators, the fixed order calculations are still subject to uncertainties originating from the choice of PDF, energy scales and $\alpha_s$.

Two programs are used which have the capability to perform calculations of the cross-sections of the processes studied in this thesis: MATRIX [21] and MCFM [22].

### 1.4.3 Electroweak corrections

The state-of-the-art predictions now typically also include NLO EW corrections. The interplay of these corrections with the QCD corrections is ambiguous due to the existence of a finite number of terms in the cross-section expansion. Currently, there are two treatments. The first includes the corrections additively to the NLO QCD cross section:

$$\sigma^{NLO}_{QCD+EW} = \sigma^{LO} + \delta\sigma^{NLO}_{QCD} + \delta\sigma^{NLO}_{EW} = \sigma^{NLO}_{QCD} + \delta\sigma^{NLO}_{EW}. \tag{1.22}$$

In the second method, the corrections are applied multiplicatively:

$$\sigma^{NLO}_{QCD\times EW} = \sigma^{LO}\left(1 + \frac{\delta\sigma^{NLO}_{QCD}}{\sigma^{LO}}\right)\left(1 + \frac{\delta\sigma^{NLO}_{EW}}{\sigma^{LO}}\right) = \sigma^{NLO}_{QCD}\left(1 + \frac{\delta\sigma^{NLO}_{EW}}{\sigma^{LO}}\right). \tag{1.23}$$

In practice the difference between the two calculations is small, although the multiplicative corrections tend to be slightly larger due to the fact that $\sigma^{NLO}_{QCD}/\sigma^{LO} > 1$. The difference between the two provides an estimate of mixed QCD-EW corrections (e.g. $\mathcal{O}(\alpha_s\alpha_{EW})$). The calculation of NLO EW corrections for $Z\gamma$ production is

described in Reference [23].

## 1.5 Multiboson processes

Figure 1.4 shows results from some of the cross-section measurements performed by the ATLAS Collaboration. As can be seen from the right-hand side of this plot, generally, the more particles in the process being studied, the lower the cross-section. This is due to the additional vertices in the interaction which reduce the amplitude. The cross-section is also dependent on the coupling between the particles which are produced and the initial-state partons, which is typically smaller for higher mass particles, with the exception of the Higgs. Additionally, the cross-section is dependent on the phase space in which the measurements are made. Processes with extremely low cross-sections, such as the production of three gauge bosons, are just becoming available to measure for the first time, thanks to the high energy and vast luminosity provided by the LHC.

The production of multiple bosons from $pp$ collisions is of interest for multiple reasons. Firstly, there is the connection with the non-Abelian triple and quartic gauge boson couplings predicted by the SM (e.g. Figure 1.2(c) and 1.2(d)). Measurements of multi-boson processes can also be used to constrain new physics which may manifest itself as anomalous couplings between gauge bosons. These couplings are separated into anomalous triple gauge couplings (aTGCs) and anomalous quartic gauge couplings (aQGCs), depending on the number of interacting bosons. These anomalous couplings can be searched for in a general way using an effective field theory (EFT) framework [25]. An EFT assumes the current understanding of the SM is a low-energy approximation of a higher dimensional theory, the effects of which become present at an energy scale $\Lambda$. The higher dimensional theory may contain additional operators which violate the conservation laws of the SM in its current understanding. These operators are suppressed by the new physics scale, $\Lambda$, so their effects may not necessarily be seen at current collider energies.

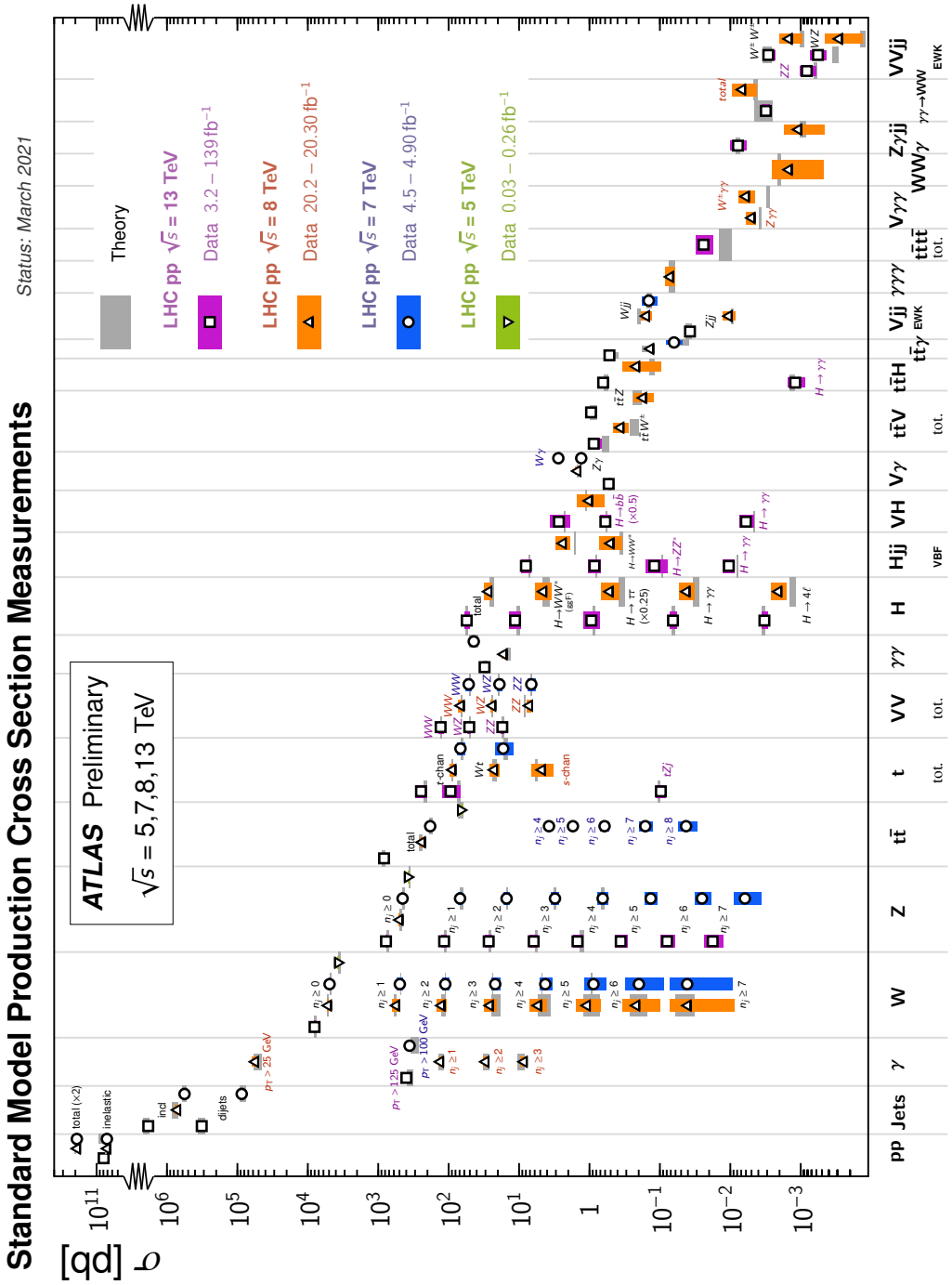


Figure 1.4: Summary of cross-section measurements made by the ATLAS experiment [24].

Precise measurements of multi-boson processes can also be used to test state-of-the-art predictions which include higher order corrections. By measuring these processes differentially we can test these calculations further in regions of phase space where the corrections are large. Finally, multi-boson processes contribute irreducible backgrounds to rare and new physics searches so it is important that they are well understood for this reason also.

The two multi-boson processes studied in this thesis are the production of $Z\gamma$ and $Z\gamma\gamma$. The $Z\gamma$ process is only sensitive to one SM-allowed EW coupling at first order which is the quartic $WWZ\gamma$ vertex (Figure 1.5(c)). For the $Z\gamma\gamma$ process, no SM EW vertices are allowed at first order, as a charged boson is needed to couple to the photons, but to include one would violate charge conservation. Both processes can be used to search for anomalous couplings, which may include more vertices e.g. $ZZ\gamma$ or $ZZ\gamma\gamma$.

In both analyses, the leptonic decay channels $Z \to ee$ and $Z \to \mu\mu$ are considered despite their lower branching fractions ($\sim$3% each), compared to the $Z \to qq$ ($\sim$70%) or $Z \to \nu\nu$ ($\sim$20%) channels. The leptonic channels benefit from the high efficiency and resolution of the reconstruction of electrons and muons, and also from lower backgrounds. For resonant $Z$ production, the dilepton invariant mass ($m_{\ell\ell}$) is peaked around the $Z$ mass of 91 GeV. There is also an indistinguishable background contribution from virtual photons $\gamma^* \to \ell\ell$ which is dominant at the lower end of the $m_{\ell\ell}$ spectrum.

## 1.6 $Z\gamma$ production

### 1.6.1 $Z\gamma$ phenomenology

The process $pp \to \ell\ell\gamma + X$, where $X$ is any additional object(s) in the event, proceeds at LO via the two $q\bar{q}$ initiated diagrams shown in Figures 1.5(a) and (b). In

Figure 1.5(a) the production of the photon is referred to as initial state radiation (ISR), where the photon is radiated off an initial-state quark. In contrast, in Figure 1.5(b) the photon is radiated off a final-state lepton and is referred to as final state radiation (FSR). These two production mechanisms produce indistinguishable signals as they consist of the same final state ($\ell\ell\gamma$). However, FSR production is kinematically similar to single $Z$ production with QED radiation from a lepton, which makes it less interesting to study as a diboson process. Figure 1.6 shows the dilepton invariant mass ($m_{\ell\ell}$) as a function of the three-body invariant mass ($m_{\ell\ell\gamma}$) for $\mu\mu\gamma$ events in data. The two populations correspond to the ISR ($m_{\ell\ell} \sim m_Z$) and FSR ($m_{\ell\ell\gamma} \sim m_Z$) production of $\ell\ell\gamma$. The FSR events can be removed experimentally by requiring $m_{\ell\ell} + m_{\ell\ell\gamma} > 2m_Z$ [26], because for FSR events $m_{\ell\ell} < m_Z$ and $m_{\ell\ell\gamma} \sim m_Z$. The cut is represented by the red dashed line in Figure 1.6, where it is seen that it distinguishes well between the two populations.

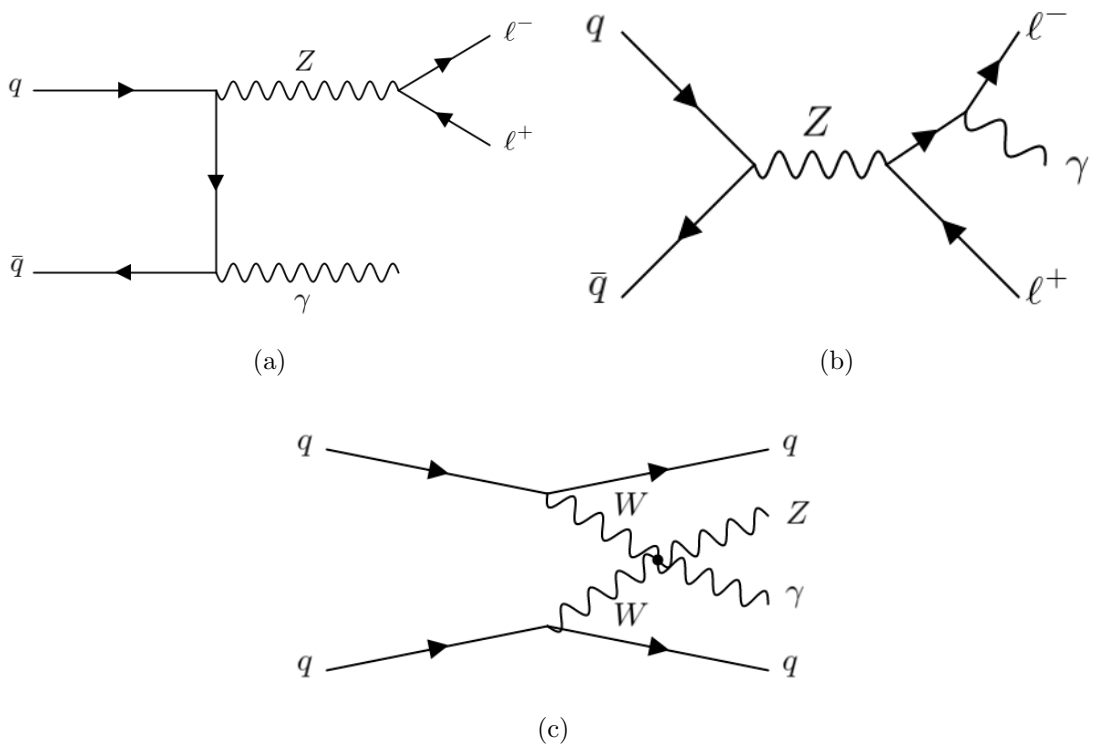


Figure 1.5: (a) ISR production of $\ell\ell\gamma$. (b) FSR production of $\ell\ell\gamma$. (c) EW vector boson scattering production of $Z\gamma$.

Also shown in Figure 1.5(c) is an example of pure electroweak production of $Z\gamma$ in

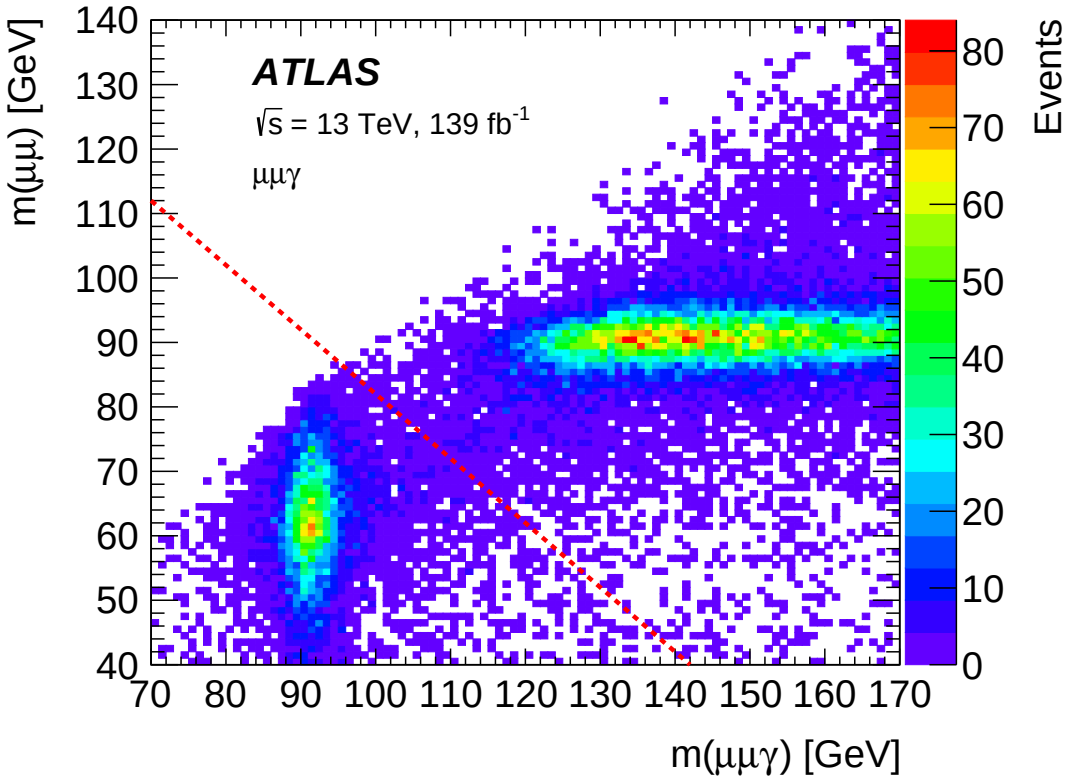


Figure 1.6: The dilepton invariant mass versus the three-body invariant mass for $\mu\mu\gamma$ events in data [26]. The ISR population is centred around 91 GeV in $m_{\mu\mu}$, and the FSR population is centred around 91 GeV in $m_{\mu\mu\gamma}$. The red dashed line corresponds to the function $m_{\mu\mu} + m_{\mu\mu\gamma} = 2m_Z$.

association with two jets. This specific diagram represents vector boson scattering (VBS) which is directly sensitive to the $WWZ\gamma$ quartic coupling. It is not expected that the $Z\gamma + X$ analysis presented in this thesis will be particularly sensitive to this process as it is dominated by QCD production processes (e.g. Figure 1.5(a)). Stand-alone analyses exist which attempt to measure the purely EW production of $Z\gamma$ in isolation [27, 28, 29].

### 1.6.2 $Z\gamma$ predictions

Three MC generator predictions for the $Z\gamma$ process are considered. As the ISR and FSR production are theoretically indistinguishable, inclusive $\ell\ell\gamma$ events are generated, and the FSR events are removed using the selection criteria defined above.

The first prediction is generated with Sherpa version 2.2.4 [16] at LO with up to three additional partons in the final state. A second is generated with Sherpa 2.2.8 at NLO with up to one additional parton at NLO accuracy and up to three with LO accuracy. The major difference between the two predictions from Sherpa is due to the different accuracy, the differences due to the different software versions are minor. Both the predictions from Sherpa use the NNPDF3.0 NNLO PDF set [30] and are merged with the Sherpa parton shower [19]. The final prediction is produced with MadGraph5 [17] at NLO with up to one additional parton in the final state. This generator uses the NNPDF3.0 NLO PDF set and is merged to PYTHIA8 [20] for parton shower and hadronisation.

Fixed-order calculations of the $Z\gamma$ cross-section are provided by MATRIX [21]. The integrated cross-section and differential cross-sections, are calculated according to a set of requirements which define a fiducial phase space (see Section 4.4). These parton-level predictions are provided at NLO and NNLO in QCD and use the CT14nnlo PDF set [31]. NLO EW corrections [23, 32, 33] are also included for the integrated cross-section and some of the differential cross-section predictions.

The contribution from the electroweak production of $Z\gamma$ (e.g. Figure 1.5(c)) is not included in the MC predictions or fixed-order calculations for $Z\gamma$. Instead, it is modelled separately by MadGraph [17] and added to all the available predictions. The size of the EW contribution compared to the total predicted cross-section is about 1% but it has a more significant contribution in the high-$p_{\mathrm{T}}$ regions of phase space.

### 1.6.3 Previous $Z\gamma$ measurements

$Z\gamma$ production has been extensively studied with experiments at the LEP [34, 35, 36] and Tevatron [37, 38, 39] colliders.

In the LHC era, both the ATLAS and CMS experiments have published measurements. The ATLAS measurements at centre-of-mass energies of both 7 TeV [40]

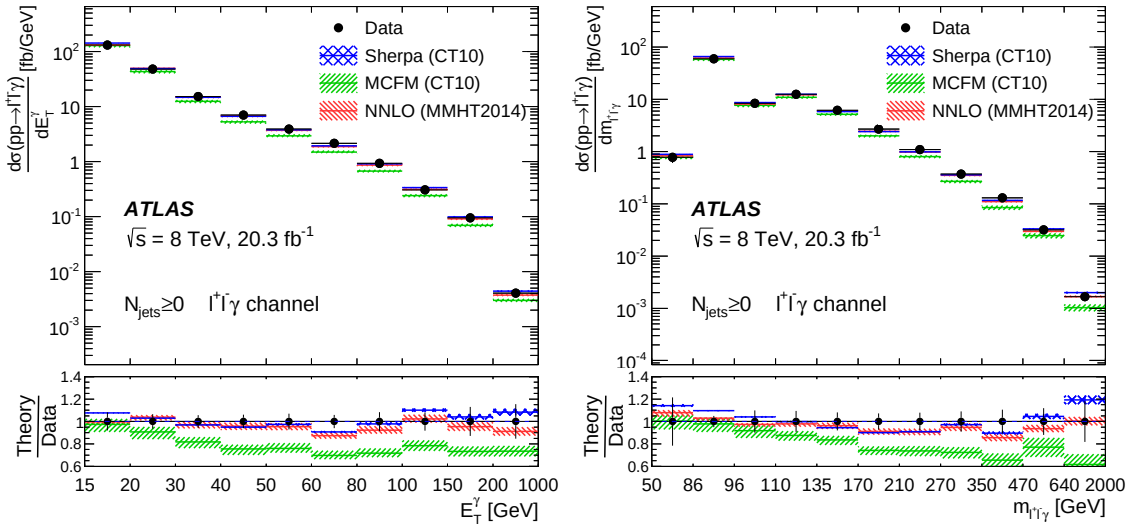


(a) (b)

Figure 1.7: The measured differential cross-sections of inclusive $\ell\ell\gamma$ production at a centre-of-mass energy of 8 TeV as a function of (a) the photon transverse energy and (b) the invariant mass of the three-body system [41]. The data are compared to predictions from the Sherpa MC generator [42] and fixed-order calculations from MCFM [43] and at NNLO [44].

and 8 TeV [41] presented differential cross-sections and set limits on anomalous triple gauge couplings. The couplings were constrained using both the $\ell\ell\gamma$ and $\nu\nu\gamma$ channels; the latter is more sensitive to aTGCs due to its higher branching fraction. In the latter of these two papers, the integrated $\ell\ell\gamma + X$ fiducial cross-section was measured to a precision of 6%. The uncertainty was dominated by systematic effects, with the largest coming from the background estimation. The differential cross-sections were reported as a function of the transverse energy of the photon and the invariant mass of the three-body system, as seen in Figure 1.7.

Similar measurements have been made with the CMS experiment at centre-of-mass energies of 7 TeV [45, 46] and 8 TeV [47]. In the latter of these papers, the integrated $\ell\ell\gamma + X$ cross-section was measured to a precision of 6%, which was dominated by systematic uncertainty, and limits were set on anomalous gauge boson couplings.

All of the previous measurements discussed here studied the inclusive $\ell\ell\gamma$ final state, i.e. the measurements included both the ISR and FSR production of $\ell\ell\gamma$. This can be

seen clearly in the $m_{\ell\ell\gamma}$ distribution in Figure 1.7(b), where there are two components to the overall spectra. Whilst these measurements include a contribution from $Z\gamma$ diboson production, the analysis presented in this thesis is the first measurement of the $Z(\rightarrow \ell\ell)\gamma$ process in isolation. Such measurements are more easily interpretable as there is only one process contributing. It also provides higher sensitivity to anomalous couplings as the production of the photon is directly connected to the hard scale of the interaction.

The EW production of $Z\gamma$ in association with two forward jets has also been searched for with the ATLAS [27] and CMS [28] detectors at $\sqrt{s} = 13$ TeV. The process has recently been observed with the CMS experiment [29].

## 1.7 $Z\gamma\gamma$ production

### 1.7.1 $Z\gamma\gamma$ phenomenology

The process $pp \rightarrow \ell\ell\gamma\gamma + X$ can proceed via a number of diagrams. A $q\bar{q}$ initiated, fully ISR, process is shown in Figure 1.8(a), and two processes involving FSR photon production are shown in Figures 1.8(b) and (c). In order to isolate the triboson production of $Z\gamma\gamma$, the FSR contributions can be removed in a similar fashion to the $Z\gamma$ case by requiring $m_{\ell\ell} + \min(m_{\ell\ell\gamma_1}, m_{\ell\ell\gamma_2}) > 2m_Z$. The subscript $\gamma_1$ refers to the higher $p_{\mathrm{T}}$ (leading) photon and $\gamma_2$ refers to the lower $p_{\mathrm{T}}$ (subleading) photon. This selection is discussed in more detail in Section 6.1.

### 1.7.2 $Z\gamma\gamma$ predictions

Two MC generator predictions for $\ell\ell\gamma\gamma$ production are provided by Sherpa [16]. The first is at NLO accuracy with Sherpa version 2.2.10. No additional partons are included in the final state at NLO accuracy, but up to two additional partons are included at LO accuracy. The second is produced with version 2.2.4 at LO accuracy

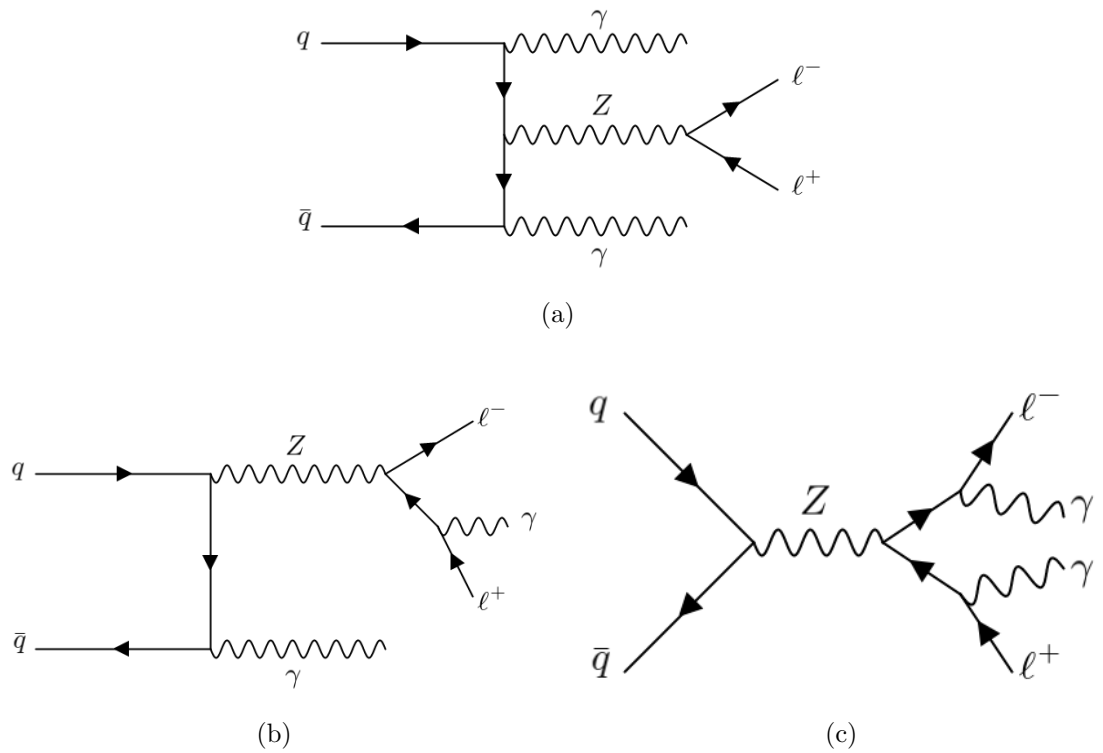


Figure 1.8: (a) Pure ISR production of $\ell\ell\gamma\gamma$. (b) Mixed ISR and FSR production of $\ell\ell\gamma\gamma$. (c) Pure FSR production of $\ell\ell\gamma\gamma$.

with up to two additional partons in the final state. Similarly to $Z\gamma$, the main difference between the two predictions from Sherpa arises due to the accuracy of the matrix element. Both predictions use the NNPDF3.0 NNLO PDF set [30] and are merged to the Sherpa parton shower [19].

### 1.7.3 Previous $Z\gamma\gamma$ measurements

The $Z\gamma\gamma$ process was first studied at a centre-of-mass energy of 8 TeV by the ATLAS experiment [41]. Integrated fiducial cross-sections were reported in the $\ell\ell\gamma\gamma$ and $\nu\nu\gamma\gamma$ channels, and these measurements were consequently used to set limits on anomalous quartic couplings. The integrated $\ell\ell\gamma\gamma + X$ cross-section was measured to a precision of 16%, where the uncertainty was statistically dominated. Detector-level distributions for the diphoton and four-body invariant masses, in the muon channel, are shown in Figure 1.9. Only 37 $\mu\mu\gamma\gamma$ events are selected in data

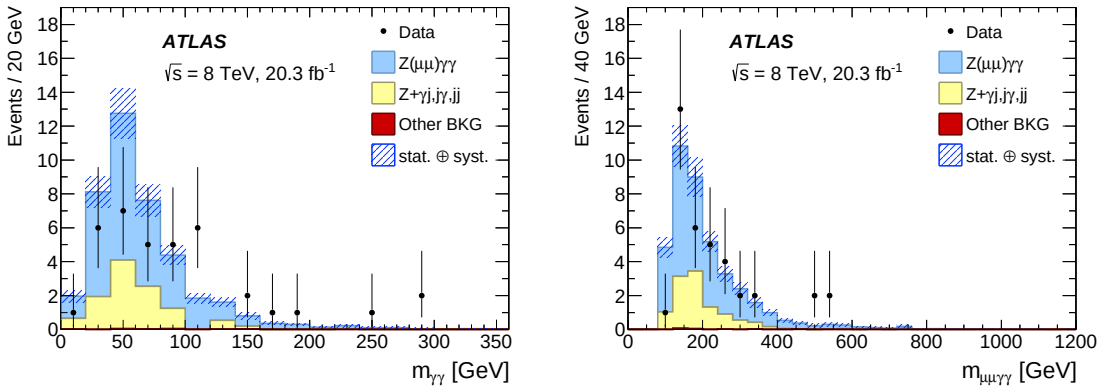


(a) (b)

Figure 1.9: The detector-level distribution of the (a) diphoton and (b) four-body invariant masses for $Z(\rightarrow \mu\mu)\gamma\gamma$ production from proton-proton collisions at a centre-of-mass energy of 8 TeV, compared to predicted signal plus background distributions [41].

for these distributions but the predictions provide a reasonable description, within uncertainty.

The CMS experiment performed similar $\ell\ell\gamma\gamma$ measurements at 8 TeV [48]. The CMS experiment has also measured $\ell\ell\gamma\gamma$ production at 13 TeV [49]. These measurements consisted of integrated fiducial cross-section measurements and limits on anomalous quartic couplings. The integrated $\ell\ell\gamma\gamma+X$ cross-section was measured to a precision of 16%.

Similarly to the $Z\gamma$ case, the previous measurements of $\ell\ell\gamma\gamma$ were performed in a phase space which included the ISR and FSR production of photons. The analysis presented in this thesis is the first measurement in proton-proton collisions of the triboson production of $Z(\rightarrow \ell\ell)\gamma\gamma$ in isolation, which has the same benefits as mentioned for the $Z\gamma$ measurements.

# CHAPTER 2

# The Large Hadron Collider and the ATLAS Detector

## 2.1 The Large Hadron Collider

The LHC[50] is located at the European Organization for Nuclear Research (CERN) near Geneva, Switzerland. The 27 km circumference accelerator is capable of accelerating and colliding two beams of protons (or heavy ions) travelling in opposite directions. The source for the protons is hydrogen gas that is passed through a strong electric field which removes the electrons from the hydrogen atoms. The protons are then accelerated in a series of smaller accelerators, gradually increasing in energy before they are injected into the LHC. The layout of this series of accelerators can be seen in Figure 2.1.

The two beams of protons are guided along a roughly circular trajectory by helium-cooled superconducting dipole magnets which produce a magnetic field of 8.3 T. The beam is focussed at various points around the ring by quadrupole magnets.

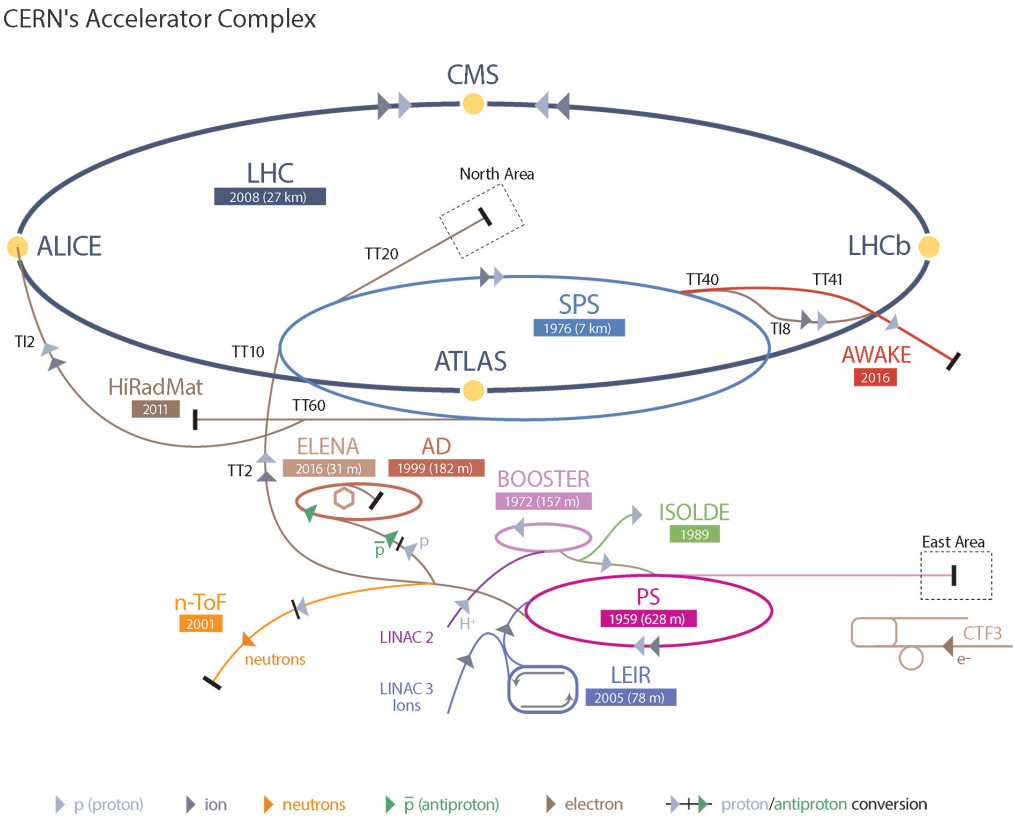


Figure 2.1: An overview of the CERN accelerator complex [51].

The acceleration is provided by superconducting radio-frequency cavities which allow each beam to be accelerated to a design energy of 7 TeV, resulting in a total available centre-of-mass energy ($\sqrt{s}$) of 14 TeV. For proton-proton collisions, each beam consists of up to 2808 bunches of $\sim 10^{11}$ protons which are separated by 25 ns. The two beams are brought together at four points on the LHC ring where detectors are situated to measure the particles which come from the resultant collisions. The instantaneous luminosity ($L$) of the collisions is given in units of $\mathrm{cm}^{-2}\mathrm{s}^{-1}$ and is defined as:

$$L = \frac{N_p^2 n_b f_r \gamma}{4\pi\epsilon_n \beta^*} F, \tag{2.1}$$

where $N_p$ is the number of protons per bunch, $n_b$ is the number of bunches per beam, $f_r$ is the frequency of the beams, $\gamma$ is the relativistic factor, $\epsilon_n$ and $\beta^*$ describe the beam optics and $F$ accounts for the crossing angle of the two beams. The instantaneous luminosity relates the rate ($\Gamma$) of a particular process to its cross-section ($\sigma$), $\Gamma = L\sigma$. The LHC has a design luminosity of $1.0 \times 10^{34}$ $\mathrm{cm}^{-2}\mathrm{s}^{-1}$. Integrating the instantaneous luminosity over a particular time period, gives the integrated luminosity which is a measure of the total amount of collisions (or data) available and is quoted in units of inverse cross-section (e.g. inverse femtobarns, $\mathrm{fb}^{-1}$). Due to the large number of protons in each bunch, multiple $pp$ collisions occur during each bunch-crossing. This effect is quantified using the average number of interactions per bunch-crossing which is referred to as pile-up, $\langle\mu\rangle$, and gives a measure of how populated the detector environment is.

The schedule for the LHC consists of running periods separated by technical shutdowns when extensive maintenance and upgrade work can be performed. Run-1 of the LHC was conducted over a period of three years between 2010-2012 where the operation was well below the design configuration, most notably the centre-of-mass energy was only 7-8 TeV and the peak instantaneous luminosity $7.7\times10^{33}$ $\mathrm{cm}^{-2}\mathrm{s}^{-1}$. The total integrated luminosity recorded by the ATLAS detector during Run-1 was approximately 36 $\mathrm{fb}^{-1}$. During the first technical shutdown, the LHC magnets were upgraded to cope with a higher centre-of-mass energy and luminosity. The data analysed in this thesis was recorded during Run-2 of the LHC which occurred be-

tween 2015-2018 at a centre-of-mass energy of 13 TeV and during which time the instantaneous luminosity exceeded twice the design value, as can be seen in Figure 2.2(a). The integrated luminosity delivered and measured as a function of time is shown in Figure 2.2(b). It is seen that a total dataset of 139 fb$^{-1}$ of data was recorded for analysis during these four years by the ATLAS detector. The higher luminosity results in much harsher pile-up conditions, shown in Figure 2.3.

Run-3 of the LHC will begin in 2022 and last until 2024. During this time, it is anticipated that the LHC will operate at a slightly higher centre-of-mass energy of 13.6 TeV and a dataset of similar size to that of Run-2 will be collected. After this time, there will be a two and a half year shutdown where major upgrade work will take place in preparation for the high-luminosity LHC [52] (HL-LHC). The HL-LHC is expected to run at up to 10 times the instantaneous luminosity of the LHC. Over its eight year operation period, the HL-LHC is expected to deliver an integrated luminosity of 3000 fb$^{-1}$ to the ATLAS detector.

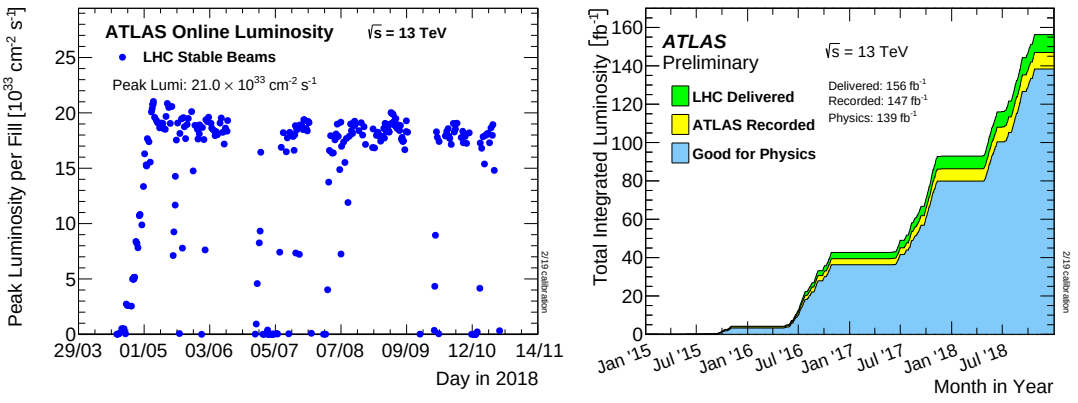


(a) (b)

Figure 2.2: (a) The peak instantaneous luminosity per LHC fill during 2018 operation. (b) The cumulative integrated luminosity, delivered by the LHC and recorded by ATLAS, over the course of LHC Run-2. Both figures are taken from Reference [53].

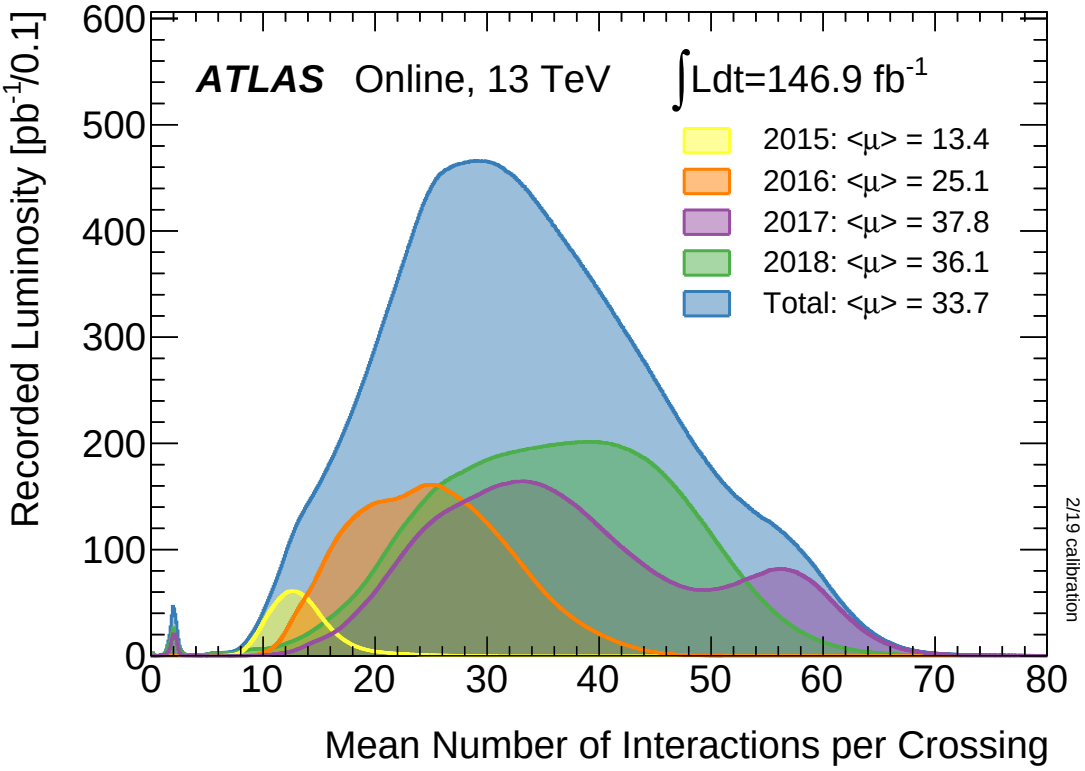


Figure 2.3: The average number of interactions per bunch crossing recorded by the ATLAS detector for each year of LHC Run-2 [53].

## 2.2 The ATLAS detector

The ATLAS (A Toroidal LHC ApparatuS) detector [54] (Figure 2.4) is a multi-purpose detector which is approximately uniform in azimuthal angle. Positions inside the detector are described by a right-handed coordinate system where the z-axis points along the beam line, the x-axis towards the centre of the LHC ring and the y-axis upwards. The point in the centre of the detector where the beams collide is referred to as the interaction point (IP), which also defines the origin of the coordinate system. The half of the detector in the forward z direction is known as the A-side, and the backward half is the C-side. In the transverse plane cylindrical coordinates $(r, \phi)$ are used to reflect the symmetry of the detector. To describe the angle made with the z-axis, the pseudorapidity, $\eta = -\ln(\tan(\theta/2))$, is preferred over the polar angle ($\theta$) as differences in this observable ($\Delta\eta$) are Lorentz invariant with respect to boosts along the beam axis. This is useful because, as

protons are composite particles, each parton-parton collision system has a different momentum component along the beam line. By considering the pseudorapidity, the collision products can be fairly compared regardless of the longitudinal boost. For the same reason, when considering the momentum of a particle within the ATLAS detector volume, only the component perpendicular to the z-axis is considered: the transverse momentum; $p_T = \sqrt{p_x^2 + p_y^2}$. Similarly, the transverse energy is also used: $E_T = \sqrt{m^2 + p_T^2}$, where $m$ is the rest mass of the particle. Angular separations between two points within the detector volume are described by the quantity $\Delta R = \sqrt{\Delta\eta^2 + \Delta\phi^2}$.

Moving radially outward from the IP, the first subsystem of the detector is the inner detector (ID) which measures the trajectories of charged particles and provides information on particle identification. The ID sits inside a thin superconducting solenoid magnet which bends the paths of charged particles and hence provides momentum measurements and charge identification. Outside the solenoid is the calorimeter system which provides energy measurements of both neutral and charged particles (excluding muons and neutrinos). Finally, the outermost subsystem is the muon spectrometer (MS) which provides triggering and tracking information on muons, which typically pass through the calorimeter system. The MS is interweaved in a toroidal air-core magnet system which provides the bending of the muon trajectories, which is needed to make momentum measurements. Each of the three subsystems is arranged in cylindrically concentric barrel layers which sit around the beam axis, and endcap layers which sit in the $r$-$\phi$ plane, the combination of which provides approximately $4\pi$ solid angular coverage. Each of the subsystems is described in greater detail in the following sections.

### 2.2.1 Inner detector

The inner detector [55] contains three sub-detectors that sit in a 2 T magnetic field which is provided by the superconducting solenoid magnet. A cross-section of the inner detector can be seen in Figure 2.5. As a charged particle traverses the

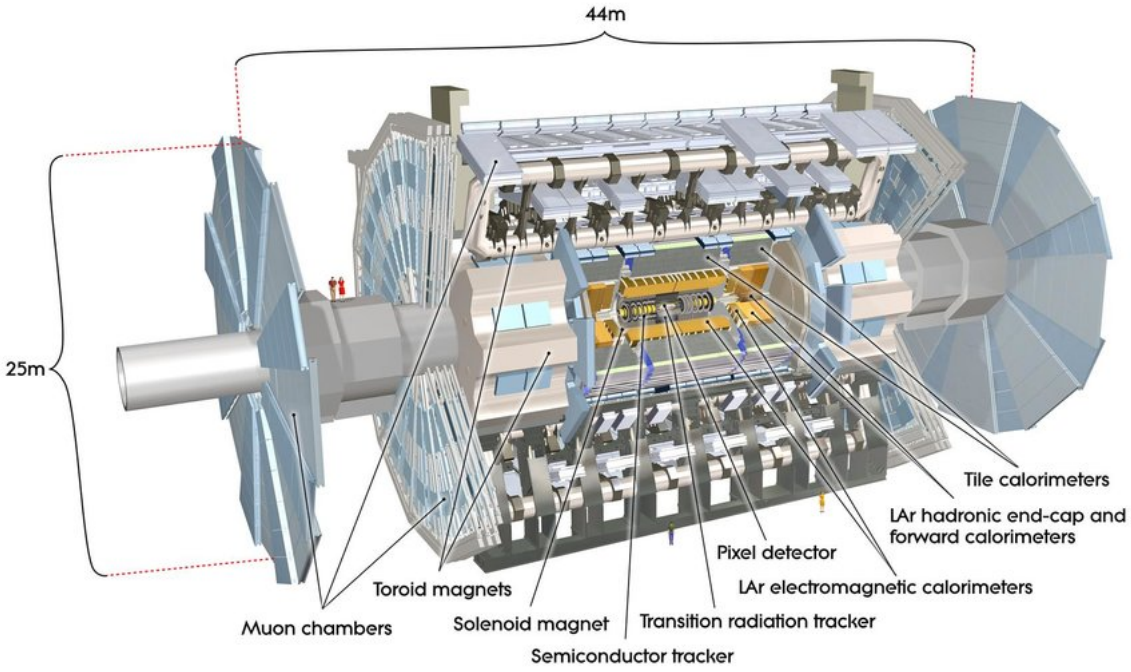


Figure 2.4: An overview of the ATLAS detector [54].

inner detector it leaves hits in each layer of the sensitive regions which can then be associated together to form tracks. The radial arc of this track can then be used to determine the momentum of the particle and the direction of the bend is used to deduce the sign of its charge. The tracks are also extrapolated back to the beam line to determine the point of origin of reconstructed particles. Overall, the inner detector provides a pseudorapidity coverage of $|\eta| < 2.5$.

#### 2.2.1.1 Pixel detector

The pixel detector covers the radii 33.25-122.5 mm and operates by detecting the charge which is generated by a charged particle moving through a silicon sensor. The charged particle produces electron-hole pairs which then flow due to a bias voltage which is applied to the sensor. The pixel detector sensors are typically $50\times400$ $\mu$m in size and are arranged in modules which contain about $4.6\times10^4$ individual pixels. A total of 80.4 million readout channels are spread across 2024 modules which are arranged in four barrel layers and three endcap disks on either side. The innermost

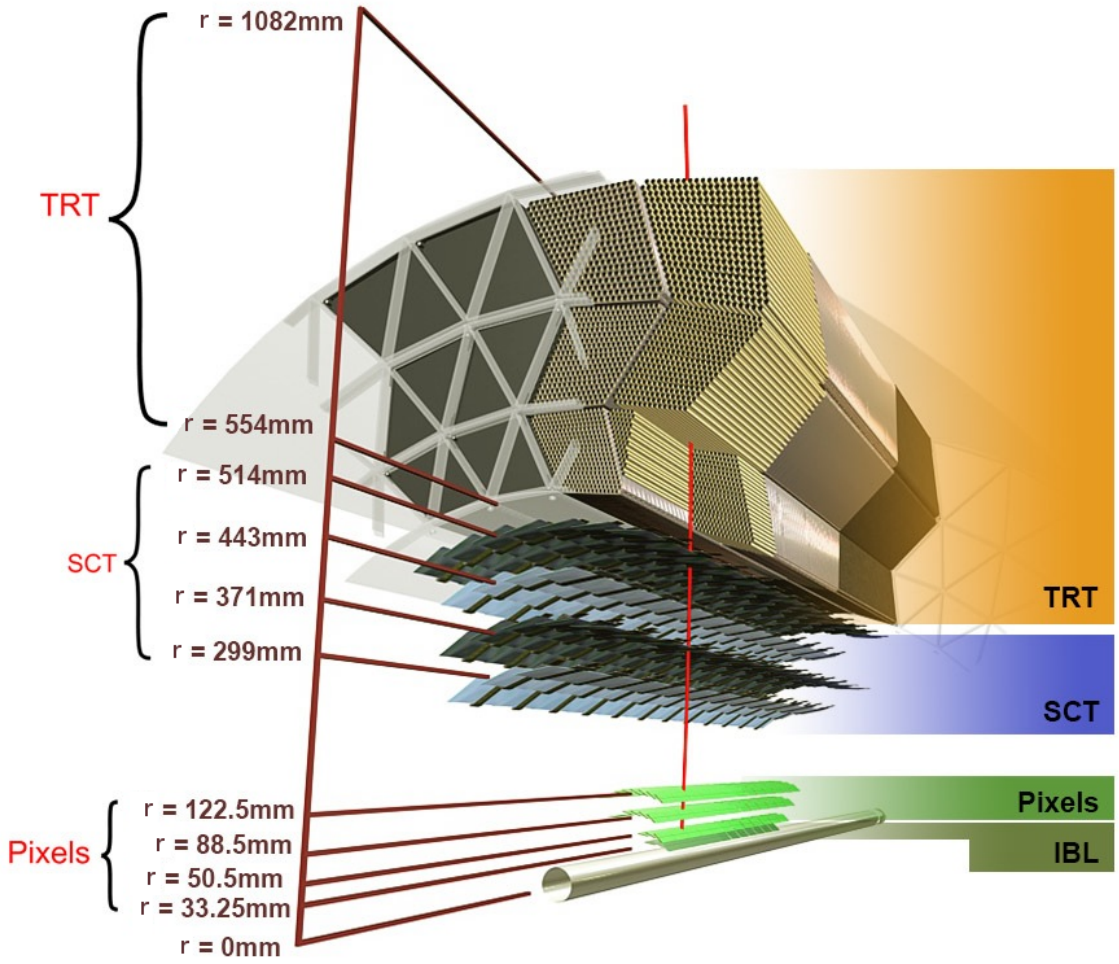


Figure 2.5: A cross-section of the ATLAS inner detector [56].

barrel layer is referred to as the insertable B-layer (IBL) [57] which sits at a radius of 33 mm away from the beam axis. The IBL was added to the ATLAS detector between Run-1 and Run-2 to improve the impact parameter resolution needed for reconstructing secondary vertices produced by decaying particles. The signal recorded by the pixel detector is the time over threshold and is read out by radiation hard front-end chips. The intrinsic $r$-$\phi \times z$ resolution of the IBL is 8×40 $\mu$m and it is 10×115 $\mu$m in the rest of the pixel barrel.

#### 2.2.1.2 SemiConductor Tracker

The SemiConductor Tracker (SCT) is a silicon strip tracker which covers the radii 299-514 mm. The arrangement of the silicon sensors in strips as opposed to pixels

allows for a greater coverage at the expense of the loss of resolution in one direction. This is the z-direction in the barrel and the r-direction in the endcaps. The strip sensor elements are typically 6.4 cm long with a pitch of 80 $\mu$m. A total of 4088 modules are arranged in four barrel layers with the strips approximately parallel to the beam line and nine endcap disks on each side with the strips perpendicular to the beam line. Each module consists of two layers of back-to-back strips which are offset by a stereo angle of 40 mrad which markedly improves the resolution in the z-direction in the barrel and in the r-direction in the endcaps. The readout principle of the SCT is binary, meaning a hit is registered if the collected charge exceeds a threshold which is typically set to 1 fC. A charged particle traversing the SCT typically registers hits in eight layers. The SCT provides a $r$-$\phi$ resolution of 17 $\mu$m and has 6.3 million readout channels. The operation of the SCT is described in more detail in Section 3.

#### 2.2.1.3 Transition Radiation Tracker

The final layer of the inner detector is the transition radiation tracker (TRT) which covers the radii 554-1082 mm. It consists of an array of 4 mm diameter straw tubes which are filled with a gas mixture, and contain a gold-plated tungsten wire which runs through the centre. Polymer fibres fill the space between the straws, which act as transition material. As a charged particle traverses a boundary it emits transition radiation photons, proportional to $\gamma = E/m$. These photons ionise the gas mixture, and the drift of the electrons and ions is then detected as a signal on the wire. The gas mixture contains xenon (or argon) which acts as the absorber of the transition radiation, and $O_2$ and $CO_2$ which improve the latency by increasing the drift velocity. As the transition radiation is higher for lower mass particles, the TRT provides useful information for the identification of electrons.

The tubes are arranged in two barrel segments with the tubes parallel to the beam line and two endcaps with the tubes perpendicular, providing a total coverage of $|\eta| < 2$. The $r$-$\phi$ resolution of 130 $\mu$m is a lot lower compared to the silicon systems,

primarily driven by the larger element size (4 mm), but this is compensated by the larger number of hits per track which is typically 36.

### 2.2.2 Calorimeter system

The ATLAS calorimeter system (Figure 2.6) is made up of an inner electromagnetic (EM) calorimeter surrounded by a hadronic calorimeter, both of which are sampling calorimeters that consist of alternating layers of passive and active materials. Particles traversing the calorimeters interact with the passive material causing them to shower, and this energy is measured in the active layers. In the EM calorimeter the passive material stimulates electrons to emit bremsstrahlung radiation, or photons to pair-produce, which initiates a shower. A hadron typically encounters 2 hadronic interaction lengths of material by the end of the EM calorimeter, which is not sufficient to stop the particle and measure its total energy. Therefore a different passive material, and more of it, is used in the hadronic calorimeter which causes the production of showers via strong interactions. A significant proportion of the energy of a hadronic shower is deposited in the EM calorimeter due to the presence of photons from light meson decays and electrons from weak decays of hadrons. A particle will deposit its energy in multiple neighbouring cells, so the cells need to be algorithmically combined into clusters in order to reconstruct the total energy of the particle. The calorimeter allows for the detection of neutral particles that do not interact with the tracking system and the shapes of the clusters are used in particle identification.

#### 2.2.2.1 Electromagnetic calorimeter

The EM calorimeter [58] uses lead as the passive material and liquid argon (LAr) as the active material. It is made up of a barrel section which provides coverage of $|\eta| < 1.475$ and endcaps either side which cover $1.375 < |\eta| < 3.2$. The sampling layers are arranged in an accordion geometry, as shown in Figure 2.7, which negates

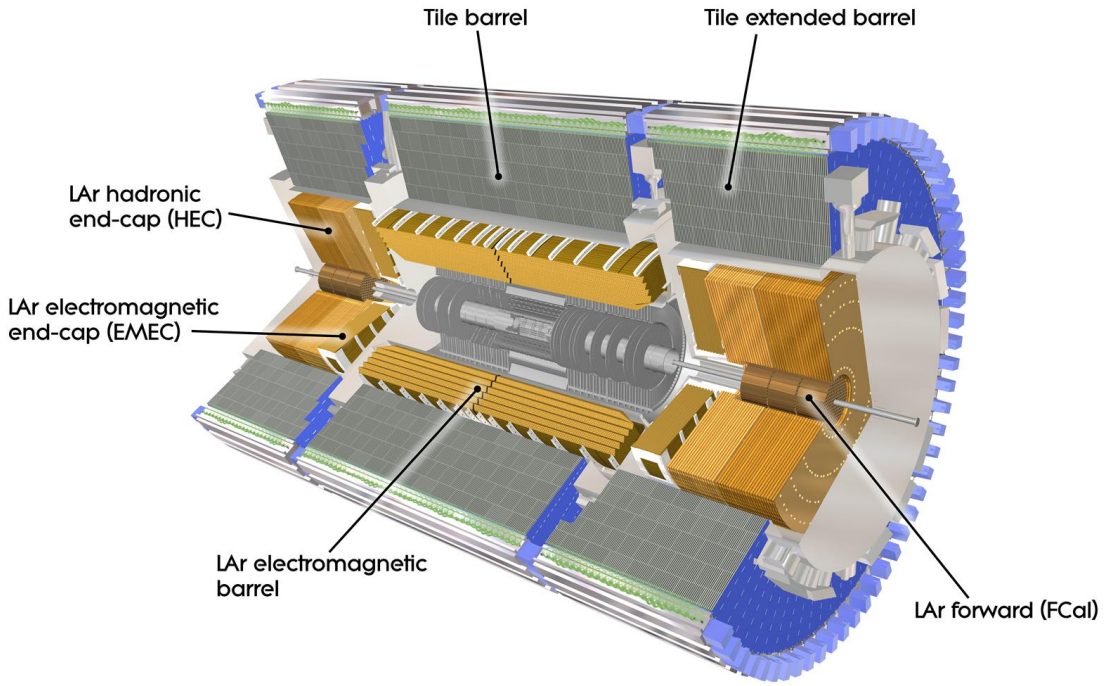


Figure 2.6: A cut-away view of the ATLAS calorimeter system [54].

the need for azimuthal gaps and so provides a uniform coverage in $\phi$. Each segment is split into three layers, the first of which is a very fine granularity strip layer that has cells of size $0.0031 \times 0.0982$ in $\eta \times \phi$ and provides coverage up to $|\eta| = 2.4$. These narrow cells are primarily used to distinguish between prompt photons and photons from light meson decays (e.g. $\pi^0 \to \gamma\gamma$), the latter producing two close-by peaks which would be measured as one in the main bulk of the calorimeter. The second layer has a coarser cell size of $0.025 \times 0.0245$, and the third layer $0.05 \times 0.025$. The third layer is used to correct for leakage into the hadronic calorimeter. Before the strip layer there is a presampling (PS) layer which is used to estimate the energy lost by particles before the calorimeter. The total longitudinal length of the EM calorimeter is 22 radiation lengths, which is sufficient to provide complete measurements of the energies of photons and electrons.

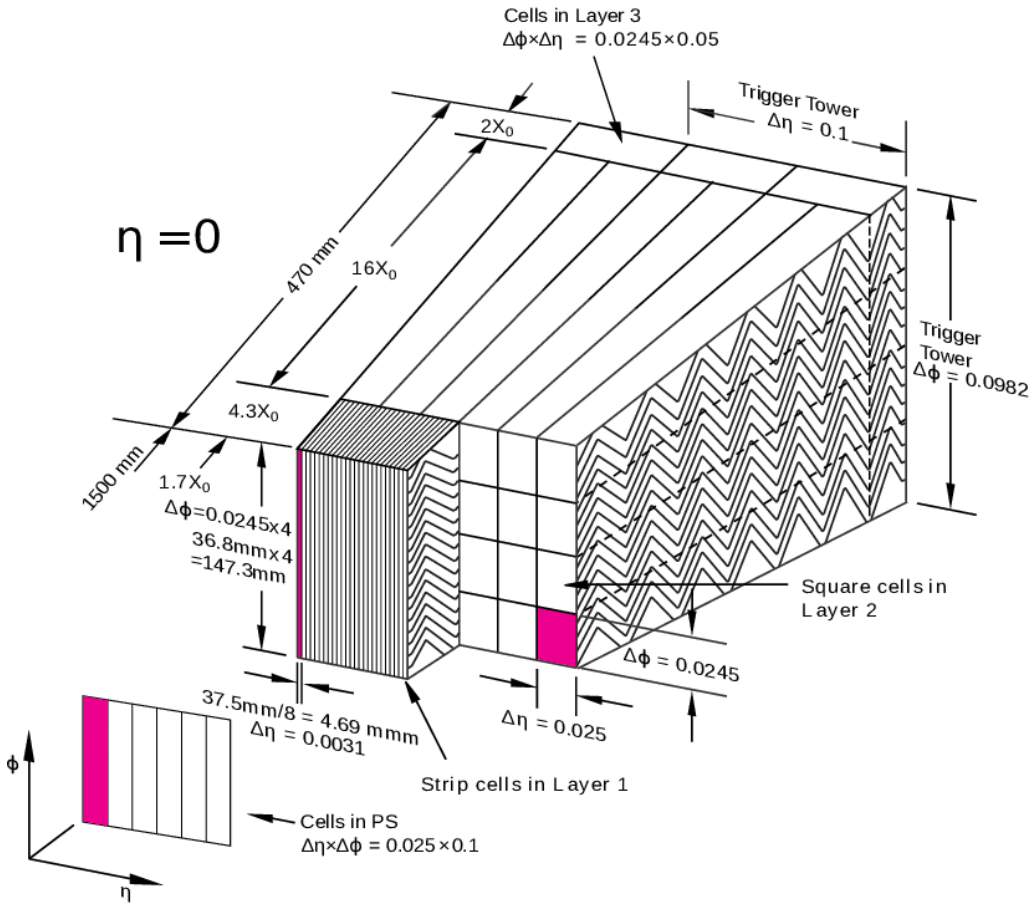


Figure 2.7: Sketch of an EM calorimeter barrel module. The sections highlighted in pink represent one cell of each layer [59].

#### 2.2.2.2 Hadronic calorimeter

The hadronic calorimeter [60] uses both LAr and tile sampling calorimeters. The tile calorimeters are used in the barrel region, $|\eta| < 1.0$ and extended barrel region $0.8 < |\eta| < 1.7$ and use steel as the passive material and scintillating plastic tiles as the active material. It is also split into three layers and requires a larger cell size compared to the EM calorimeter as a much larger volume is covered, $0.1 \times 0.1$ in the first two layers and $0.1 \times 0.2$ in the third.

LAr calorimeters are used in the hadronic endcaps with copper used as the passive material. The two endcaps per side provide coverage of $1.5 < |\eta| < 3.2$. Inside these endcaps sits the forward calorimeter (FCal) which covers the range $3.1 < |\eta| < 4.9$. The FCal also has LAr layers, the first of which uses copper as the passive material

and is primarily intended for electromagnetic calorimetry and the final two use tungsten as the passive material for hadronic calorimetry.

### 2.2.3 Muon Spectrometer

Muons typically pass through the ID and calorimeter systems without being stopped so a separate system, the muon spectrometer (MS) [61], is used to measure their trajectory after the calorimeter system. The MS consists of triggering and tracking chambers interspersed within and around the toroidal magnet system. The layout is shown in Figure 2.8. The magnet system consists of a barrel toroid ($|\eta| < 1.4$) and two endcap toroids ($1.6 < |\eta| < 2.7$) which produce a toroidal magnetic field that bends the paths of muons, allowing momentum measurements to be made. Most of the coverage for the tracking system is provided by monitored drift tubes (MDT) which have an operation principle similar to that of the TRT and provide a resolution of 80 $\mu$m per tube. The MDTs are arranged in three barrel layers and three endcaps which cover the full $|\eta| < 2.7$ range. In the innermost layer of the endcap ($2.0 < |\eta| < 2.7$), the MDTs are replaced by cathode strip chambers (CSC). The CSCs provide higher granularity position measurements and better timing resolution which assist with higher muon rates in this region. The CSCs consist of anode wires suspended between two cathode plates, one of which is segmented in the direction parallel to the wires and one of which is perpendicular. The signal is read out from the cathode plates meaning that both $\eta$ and $\phi$ coordinates are measured. The CSCs have a resolution of 60 $\mu$m in the $\eta$ direction and 5 mm in the $\phi$ direction.

The first of the trigger chambers consists of the resistive plate chambers (RPC) which cover the barrel region, $|\eta| < 1.05$. The RPCs are made of two resistive plates separated by a gap of 2 mm which is filled with a gas mixture. As with the CSCs, the readout strips on each plate are perpendicular to each other, allowing for an $\eta$ and $\phi$ measurement. In the endcaps, thin gap chambers (TGC) are used which operate in a similar way to the CSCs but with a faster readout suitable for triggering. The TGCs also provide $\phi$ coordinate measurements which complement

the position measurements made in the endcaps by the MDTs. The muon triggering systems provide signals in a time range of 15-25 ns meaning that the muons can be matched to the correct bunch-crossing.

The reconstruction of muon tracks relies on the combination of measurements from both the tracking and triggering chambers, which are grouped together in pairs in each layer such that each trigger chamber corresponds to a certain set of tracking channels. The tracking chambers provide a well resolved coordinate of the track in the bending plane. This is then combined with the hit in the corresponding trigger chamber, which is taken as the coordinate in the non-bending plane. This operation principle relies on the assumption that there is not more than one muon per trigger chamber per event, the probability of which has been determined from simulation to be 0.0015% and so is negligible [54].

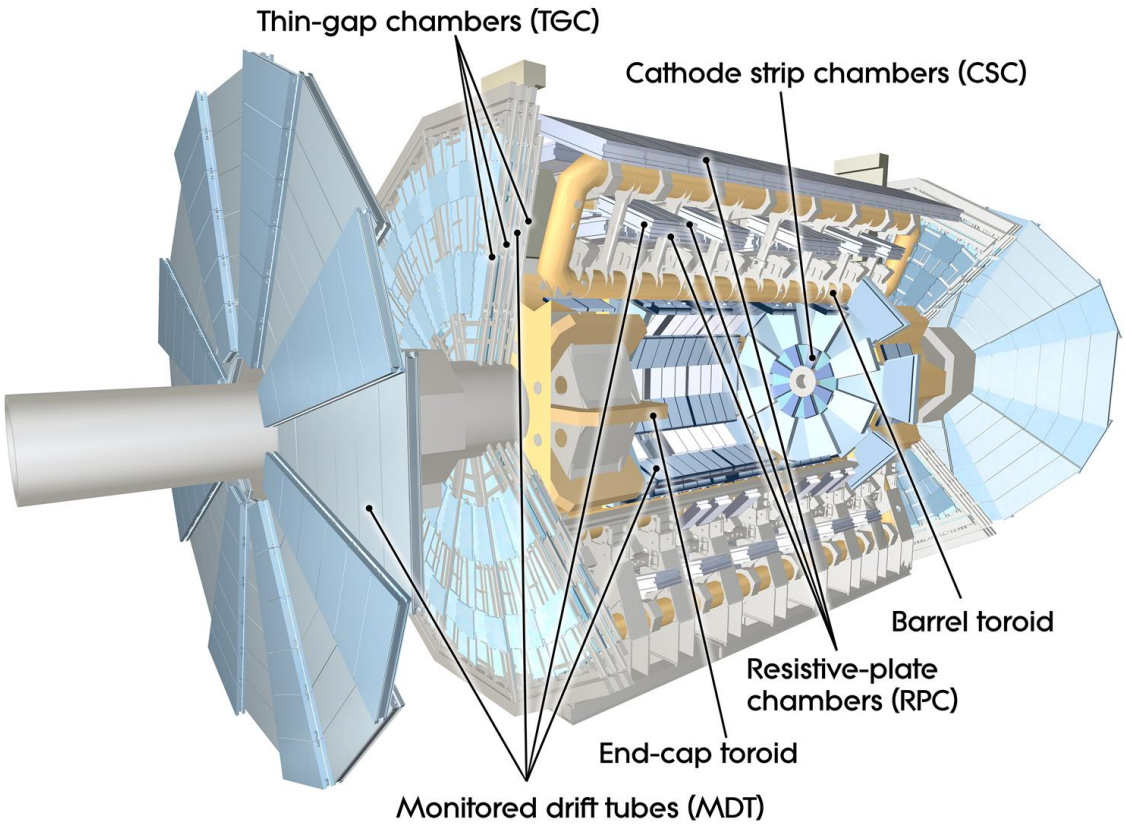


Figure 2.8: A cross-section of the ATLAS muon spectrometer [54].

### 2.2.4 Luminosity measurement

Knowing the delivered integrated luminosity precisely is essential for most physics analyses. For example, the measured cross-section of a process is calculated from the number of events divided by the luminosity $\sigma = N/L$, so large uncertainties in the luminosity reduce the precision of such measurements. The primary luminosity measurement in ATLAS is provided by the LUCID detector [62], which uses two stations located at 17 m either side of the interaction point. These stations consist of an array of Cherenkov tubes which detect protons that have been inelastically scattered, from which the relative luminosity can be calculated. The LUCID detector is calibrated using van der Meer scans, where the separation of the beams is varied independently in the $x$ and $y$ directions. These scans allow the beam size to be determined, which can then be used to calculate the instantaneous luminosity. The full description of the luminosity measurement can be found in Reference [63].

A set of data quality (DQ) criteria is defined which requires all of the subsystems to be functioning properly so that the data is suitable for physics analysis. This is why the total Run-2 luminosity used is lower than what was recorded by the ATLAS detector, as can be seen in Figure 2.2(b).

### 2.2.5 Data acquisition and trigger

The information from the ATLAS detector subsystems is read out by the data acquisition (DAQ) system [64]. Due to the extremely high LHC bunch crossing rate of 40 MHz, it is impossible to record every event. Therefore, a trigger system is used to quickly choose which events to save and to disregard non-interesting events. The trigger system has two levels, the Level-1 (L1) which is a hardware trigger and the high level trigger (HLT) which is a software trigger.

The L1 trigger [65] decides within 2.5 $\mu$s whether an event is given to the HLT or whether it is neglected. In order to do this, it searches for interesting physics

signals in the calorimeters and muon systems, which are then labelled as regions of interest (RoI). The L1Calo trigger uses energy deposits in coarse regions called trigger towers which are a group of calorimeter cells that cover $0.1\times0.0982$ in $\eta \times \phi$ and span both calorimeter systems. The deposits are then linked to physics objects (electron, photon, jet etc.) based on their estimated $E_T$ values. The L1Muon system uses the approximate position information gained from the muon trigger chambers to quickly estimate the transverse momentum of muons. A muon is identified by coincidences in two chambers that are roughly consistent with a particle coming from the interaction point. The information from L1Calo and L1Muon is then passed to the topological processor, L1Topo, which combines the given information to compute topological variables which aid in determining the significance of an event, for example, the invariant masses of different objects. The information from L1Calo, L1Muon and L1Topo is sent to the central trigger processor (CTP) where the decision is made whether to keep an event for further processing. This decision is made based on the number of high $p_T$ objects, topological features and the total energy measured in the event. The L1 trigger reduces the event rate to 100 kHz.

The HLT [64] performs a finer granularity reconstruction using the full precision of the detector, including tracking information. This can be done either in the RoIs highlighted by the L1 trigger or using the full detector. The identified physics objects must pass a more stringent set of cuts in order for the event to be saved. These cuts correspond to various trigger streams that look for certain objects, the total group of which is referred to as the trigger menu. The HLT reduces the rate down to 1 kHz which is sufficiently low for the full event information to be written to disk. The raw detector output is then processed at the CERN Tier-0 computing facility and is saved in a format which contains all the detector-level information.

This detector information is then processed in order to reconstruct physics objects which are saved in a format called the analysis object data (AOD). The AOD information can be processed further into derived analysis object data (DAOD) which includes further reconstruction, and only keeps information necessary for studying certain physics processes. The DAOD format is the typical input into user-level

analyses. The processing and storage of ATLAS data utilises the Worldwide LHC Computing Grid [66] which is a network of many different computing sites across the globe.

# CHAPTER 3

# SCT Calibration and Performance Monitoring

A charged particle moving through the ATLAS detector typically produces eight hits in the SCT which are used in reconstructing the trajectory of the particle (track). Generally, there are two categories of problem with the SCT sensors that can degrade the reconstruction of these tracks. The first comes from sensors that register a hit without the passage of a charged particle; this is typically caused by electronic noise. The second is where the sensor does not register a hit when a charged particle passes through it. The components of the SCT are expected to deteriorate over time, particularly due to the high radiation levels which they are exposed to during data-taking. Therefore, the monitoring of the two types of problem is crucial to ensure optimal performance of the SCT. This was particularly important during Run-2 as the SCT ran with occupancy and pile-up more than twice as high as it was designed to cope with [55]. The effects of radiation damage in the SCT were measured during Run-1 [67] and showed good agreement with the predictions. However during Run-2 the effects of the higher-than-design luminosity and pile-up resulted in significant

radiation damage to the SCT sensors [68], indicating that care must be taken in order for the SCT to perform well until the end of Run-3 (2022-2024) after which it will be decommissioned.

During data-taking periods the detector is calibrated frequently in order to achieve the best performance. The calibration procedure is used to tune various parameters and to identify defective areas of the detector. As well as calibration, analysis of the data quality recorded by the SCT during running is needed to further diagnose problematic areas of the detector. One such analysis involves measuring the hit efficiency of SCT sensors. Two web displays have been implemented by the author, one which is used to monitor the SCT calibration results and one which is used to investigate the efficiency of SCT modules.

The operation of the SCT detector is outlined in Section 4.1. The calibration procedure for the SCT is described in Section 4.2 along with an overview of the calibration web display. The calculation of the SCT hit efficiency and implementation of the Performance Analysis Tool, used for efficiency monitoring, are described in Section 4.3.

## 3.1 SCT operation

The SCT comprises about 6.2 million silicon strip sensors arranged on 4088 modules, as described in Section 2.2.1.2. Silicon can be doped with donors (acceptors) to become n-type (p-type), meaning that free electrons (holes) are added to the lattice. Heavily doped silicon has enough charge carriers to exhibit similar conductivity to metals and is denoted as $n^+$-type and $p^+$-type. Silicon of this type is useful for providing an ohmic contact between silicon sensors and readout electronics. The SCT sensors are made of p-in-n silicon where $p^+$-type strips sit on an n-type bulk as can be seen in Figure 3.1. In the region where the two silicon types meet, the free charge carriers combine to form a stable region that contains an electric field, called the depletion region. Any persistent current that flows in this region is referred

to as the leakage current. A 150 V reverse bias is applied across the sensors that increases the size of the depletion region which constitutes the active volume of the sensor. The voltage required to fully deplete a silicon sensor is known as the depletion voltage ($V_{FD}$). A sufficiently energetic charged particle moving through the depletion region produces electron-hole pairs which drift due to the electric field. Aluminium strips are placed on top of the $p^+$-type strips which act as electrical contacts to the front-end of the chips. The chips perform the charge collection, amplification, discrimination and readout of the data. The chips can also inject a known amount of charge into the readout channels in order to calibrate the response. A block diagram displaying the components of the chips can be seen in Figure 3.2.

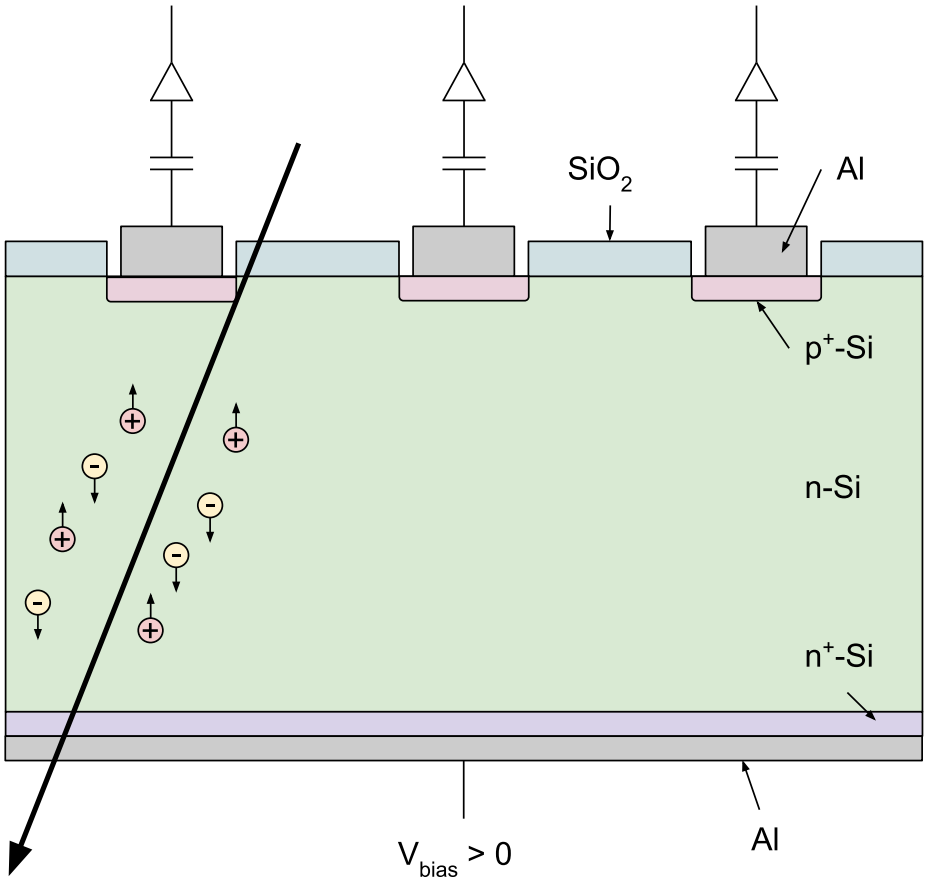


Figure 3.1: A schematic diagram of a p-in-n silicon strip sensor. A charged particle (large black arrow) produces electron-hole pairs when passing through the n-type bulk. These drift due to the electric field and are collected on the $p^+$-type strips. The aluminium strips provide electrical contacts to the front-end of the chips.

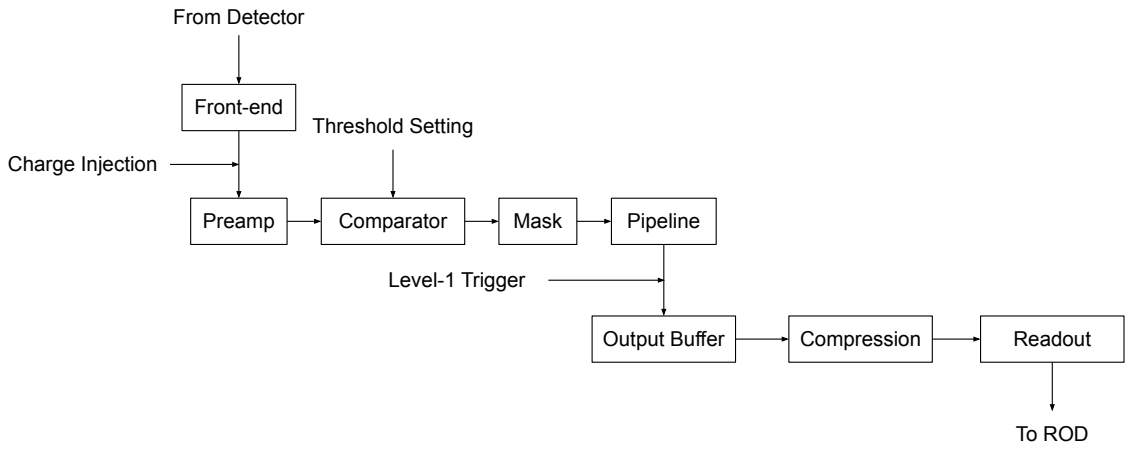


Figure 3.2: The components of the SCT readout chips.

The channels use a binary readout; a hit is registered if the signal recorded by a channel exceeds a certain threshold and this typically corresponds to 1 fC of collected charge. The readout of the channels uses a '01X' scheme, which means that if a signal is read out from one bunch crossing, then any signal from that channel during the next bunch crossing is rejected in order to avoid the overlap of two signals. As the occupancy of the detector is around 1% this only has a small effect on the efficiency. Each side of a module has 6 chips which are in turn connected to 128 channels each, resulting in $2\times6\times128 = 1536$ channels per module. A photograph of a barrel module is shown in Figure 3.3, where it can be seen that the two sides of the module are offset by a stereo angle of 40 mrad. This stereo angle enables a measurement of tracks in the direction along the length of the strips. Each module is connected to the readout system by two optical fibre links. The readout system consists of back of crate (BOC) cards which connect directly to the modules, and readout drivers (RODs) which link the BOCs to the ATLAS trigger system. The combination of one BOC and one ROD processes data from up to 48 modules. The RODs are arranged across eight crates, each of which contain slots for 768 RODs, but are optimised so that a power outage of a single crate has the smallest possible effect on the coverage of the detector.

During data-taking runs, the bias voltage applied across the SCT sensors is kept at a low level until the LHC declares stable beams. This is so that if there are

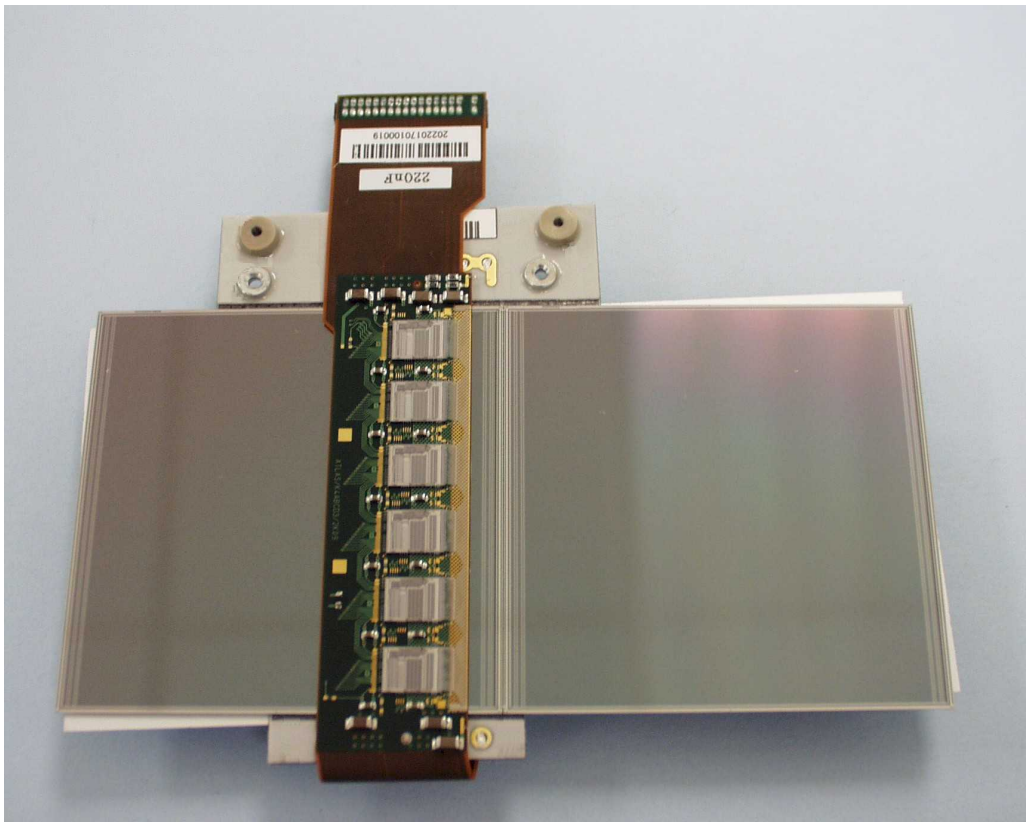

Figure 3.3: An SCT barrel module [69].

unexpected beam losses into the detector, the damage to the SCT sensors would be minimised. Once stable beams are declared, the detector control system ramps up the voltage across the sensors automatically and begins to take data. When the experiment is not taking data, the SCT is calibrated as often as possible, typically a few times per week. The calibration procedure is described in the following section.

## 3.2 Calibration

Various calibration tests are performed which probe and optimise the performance of the silicon sensors and the detector readout. In a standard calibration sequence, the performance of the optical links and the digital performance of the chips are first verified, in order to establish reliable communication and readout of the modules. After this is done, the sensors themselves can be calibrated. These calibration tests aim to ensure that the SCT sensors maintain a high efficiency and low noise. Two

such tests are used: the N-point gain test and the noise occupancy test. These are described in the following sections.

The results of the calibration tests are stored in a database which is typically only used by the SCT operations team. This is referred to as the SCT calibration database. The results include a list of strips which have been identified as defective during the calibration tests and these are known as defects. The defects are uploaded to the central ATLAS conditions database which contains conditions data for all sub-detectors. The ATLAS conditions database uses a COOL [70] schema which is accessed by analysis software in order to get the run-by-run conditions data. The SCT calibration defects are used to flag faulty SCT sensors (e.g. dead strips) during the offline reconstruction of events.

### 3.2.1 N-point gain

The main feature of this calibration test is the threshold scan, where the occupancy of each sensor is measured whilst varying the threshold to register a hit. The threshold is measured in mV and corresponds to the average channel output for a particular value of injected charge. Each sensor is injected with a certain amount of charge multiple times for each threshold value, and the fraction of these charges which register a hit is the measured occupancy. As the threshold is reduced, the occupancy increases from zero until a plateau is reached. A typical example of this distribution can be seen in Figure 3.4(a) and is described by a complementary error function. From a fit to the data points, the threshold value at which 50% occupancy is achieved ($V_{t50}$) and the width are extracted. The width of the distribution gives a measure of the amount of noise in the sensor. The value of the threshold used when the detector is running is taken from the threshold scan at 1 fC of injected charge. This value is chosen as it is above the typical electronic noise for a sensor, and below the typical charge deposited by a minimum-ionising particle.

For the N-point gain test, the threshold scans are repeated with N different values

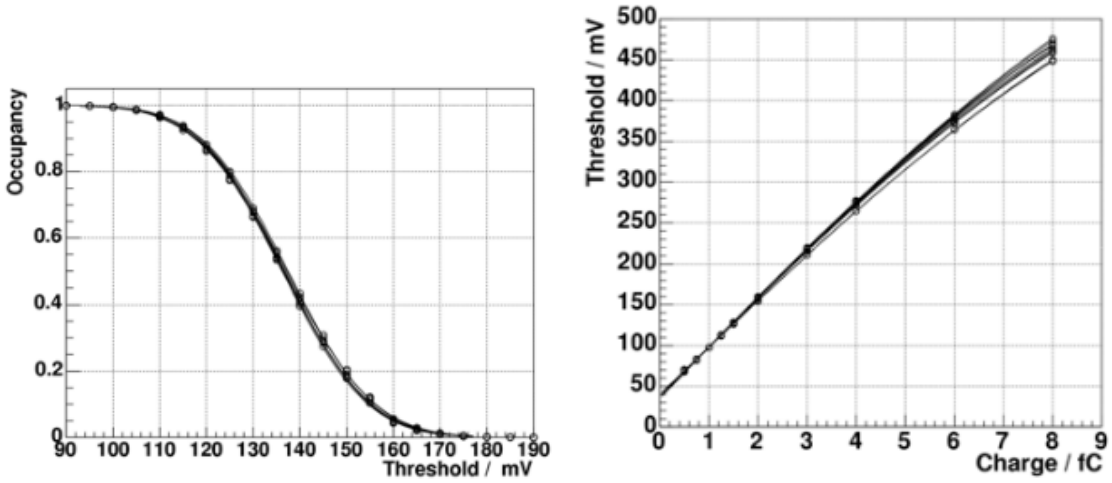


(a) (b)

Figure 3.4: (a) The mean occupancy of 6 chips as a function of threshold. (b) The response curves of the mean 50% occupancy threshold value versus the value of the injected charge for 12 chips. Both figures are taken from Reference [71].

of injected charge, typically ranging from 0.5 fC to 8 fC. A 10-point gain test is performed occasionally to fully update the configuration information of the detector, whereas a 3-point gain test is used regularly to get a quick snapshot of the performance of the detector. The value of $V_{t50}$ is measured as a function of the injected charge from which the response of the sensor can be extracted; an example is shown in Figure 3.4(b). The relationship between the injected charge and $V_{t50}$ is linear at low values of injected charge but becomes non-linear at high values due to the preamplification of the signals. From the curve, the gain of the channel is extracted as the gradient measured at 2 fC injected charge (in the linear regime) and the offset (y intercept). The output noise extracted from the response curve is divided by the gain in order to estimate the input noise, typically quoted in units of equivalent noise charge (ENC). The parameters extracted from the fit are used to define defects, typically requiring that a parameter (occupancy, noise, gain or offset) is above or below a certain threshold. A full list of the N-point gain defects and their definitions can be found in Appendix A.

### 3.2.2 Noise occupancy

The noise occupancy test is similar to the N-point gain test, with the exception that no charge is injected into the chip front-ends. Therefore any hits which are recorded are produced by noise. At high threshold values, the number of hits recorded is very low, which means that a large number of samples are required in order to accurately measure the occupancy. The measured noise occupancy of a channel is required to be smaller than 0.05% at a threshold of 1 fC, otherwise a defect is assigned. The noise occupancy test also investigates the generation of noise due to the readout by sending two samples in quick succession. If the noise occupancy is consistently higher in the second sample then this could be due to noise effects generated by the first. A full list of the noise occupancy defects and their definitions can be found in Appendix A.

### 3.2.3 Conditions database display

The first web display mentioned in the introduction to this chapter is used to display the SCT calibration defect information that is stored in the ATLAS conditions database. Screenshots of the display can be seen in Figures 3.5 and 3.6. A menu is displayed on the main page in which input parameters are defined that are used to construct queries to be sent to the conditions database. The main input parameters are the type of defect to be displayed (N-point gain or noise occupancy), the display layout and the run number. The display layout can be chosen to represent a particular geometrical layer of the detector, either a barrel layer or an endcap disk, or a particular ROD crate. The run number corresponds to a period of time for which the defects returned by the query are applicable. The number of defects for each selected module is displayed in the desired layout and is colour-coordinated so that the modules with the most defects can be identified by eye. When clicking on a module, the user is taken to a history page for that module, which displays all the information on the conditions database uploads made for that module. The modules

can also be individually searched for from the main page. A 'worst offenders' button is also implemented that finds the modules that currently have the largest number of combined defects (N-point gain and noise occupancy).

After a calibration sequence, the display can be used to quickly check that the results have been uploaded to the ATLAS conditions database. Problematic modules with large numbers of defects can be easily identified and investigated further to see whether the problems are new or the module is historically problematic. The display can also be used to search for modules with another known problem (e.g. low efficiency) to understand whether the cause can be attributed to the defects identified during the calibration.

## 3.3 SCT performance

Monitoring of the data recorded by the SCT is vital to ensure that it is good for use in physics analysis. This monitoring is done as the detector records data (online) and also through fast analysis of the reconstructed data for each run (offline). The hit efficiency of the SCT modules is one of the parameters which is measured during the offline analysis. The efficiency is required to be >99% to ensure that the SCT provides enough hits for all the charged particle tracks in each event. Over time the efficiency of SCT modules is expected to drop due to the presence of noisy strips, which arise due to radiation damage, however the efficiency is mostly recovered by performing regular calibrations as described in Section 3.2. The long-term degradation of the hit efficiency can also be caused by radiation damage effects [67]. In 2018, a drop in the efficiency was observed in the innermost barrel layer of the SCT which was not able to be recovered by calibration. As the inner barrel layer receives the highest radiation dose, it was anticipated that this was due to radiation damage effects, and this was confirmed by measuring the efficiency as a function of the supplied voltage (HV) to the sensors. Such a measurement gives an indication of $V_{FD}$ as the efficiency plateaus once the applied voltage is high enough to fully

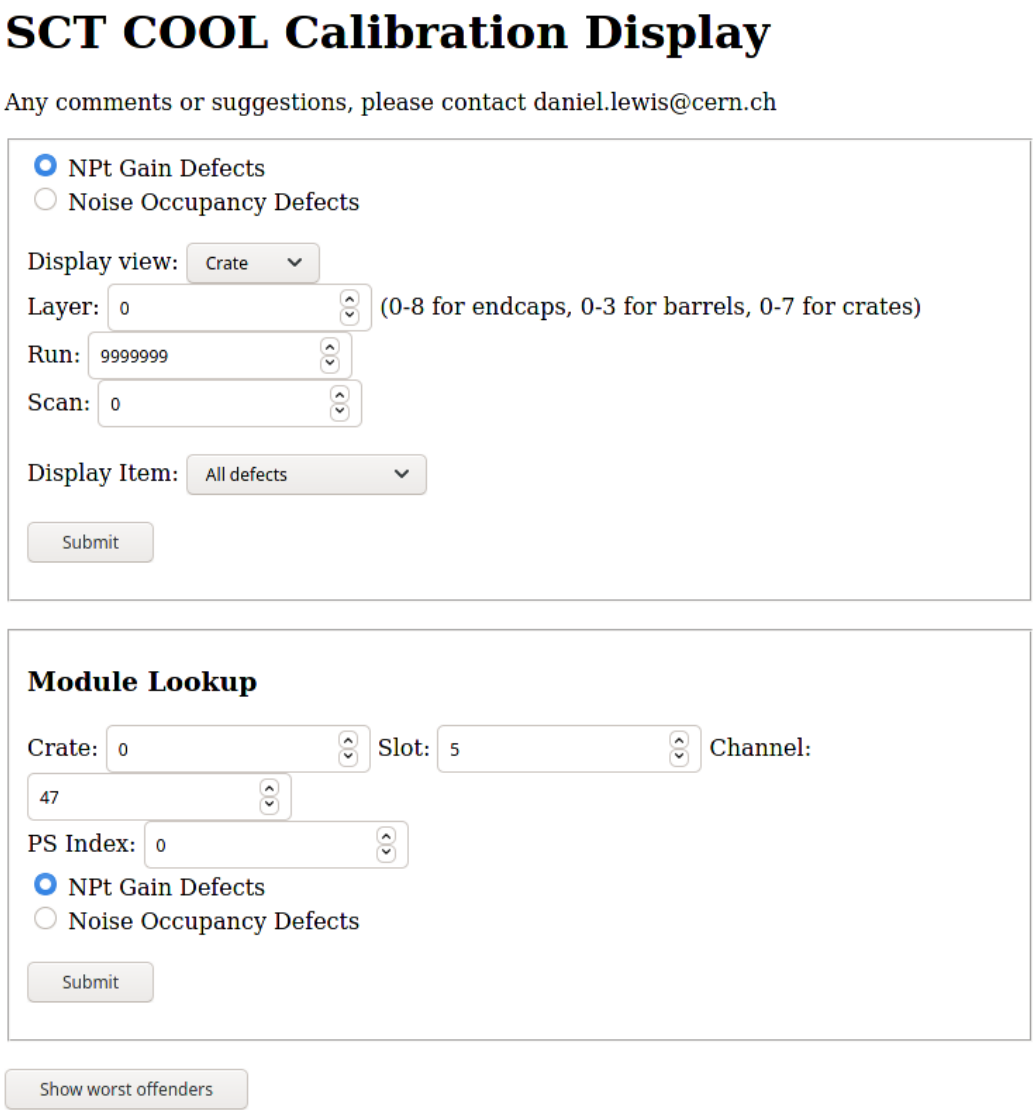


Figure 3.5: The menu for the SCT conditions database display.

deplete the sensors and hence maximise the active volume. The inferred $V_{FD}$ was larger than was predicted by models, so the cause of the inefficiency was attributed to the under-depletion of the sensors. The efficiency was recovered by raising the applied voltage on the sensors from 150 V to 250 V.

As the SCT continues operation in Run-3, it is vital to continue to monitor and diagnose the causes of inefficiency as the radiation damage has already been shown to be significant. The radiation damage increases the depletion voltage of the sensors, meaning that a higher voltage has to be applied in order to maximise efficiency. The HV has a limit of 500 V so it is important that the radiation damage effects

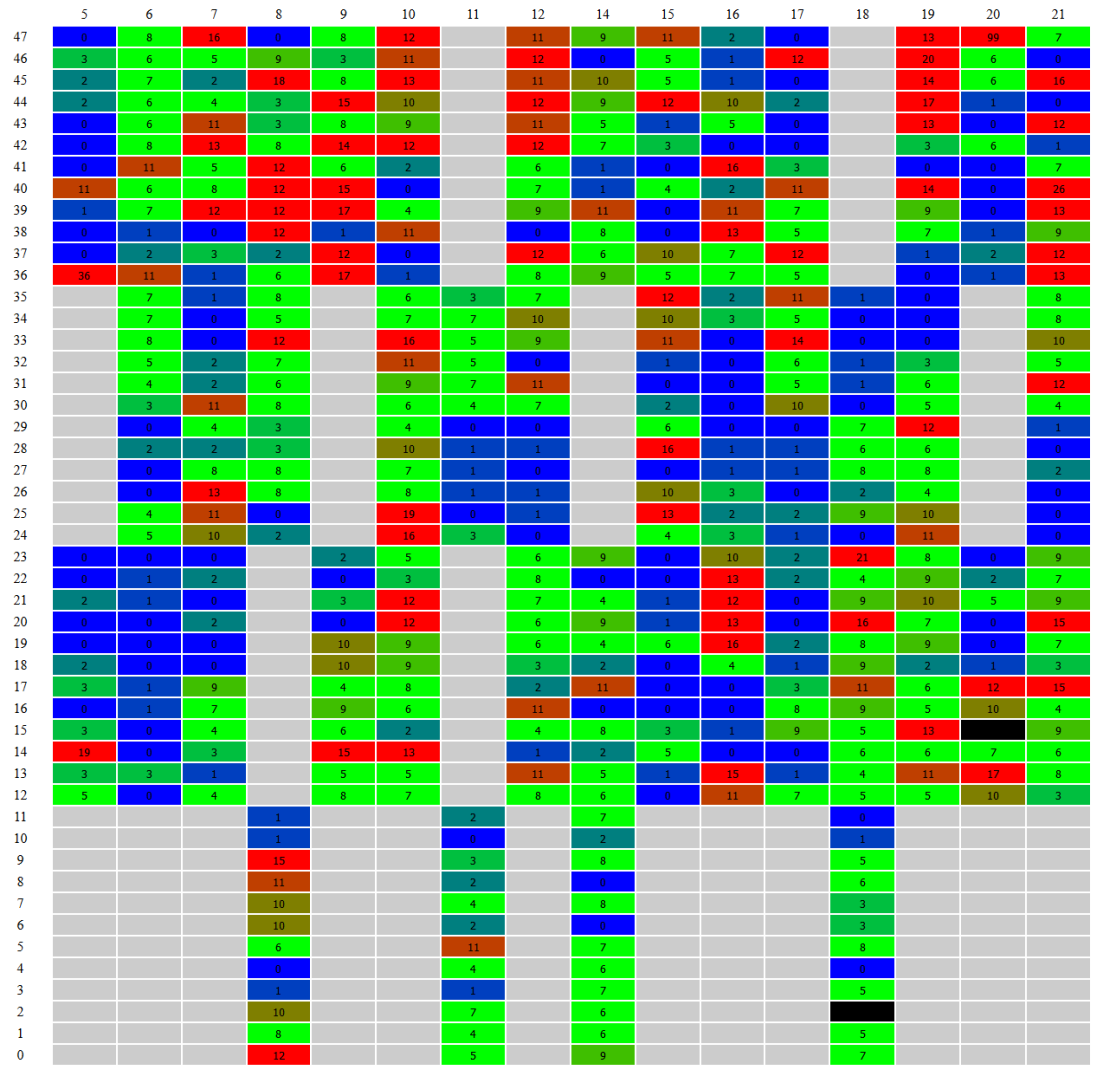


Figure 3.6: An example output of the SCT conditions database display. The number of defects is shown per module for an entire ROD crate. The horizontal direction refers to the ROD slot number and the vertical direction refers to the ROD channel number. The modules are colour-coordinated from blue (good) to red (bad) based on the number of defects. A grey entry indicates an empty ROD channel and a black entry indicates a disabled module.

are closely monitored so this limit is not reached. The implementation of the Performance Analysis Tool has been established towards the end of Run-2. This tool is designed to quickly check for modules with poor efficiency and see whether the cause is known, for example, from noisy or defective strips, or whether it is possibly related to radiation damage.

### 3.3.1 Efficiency calculation

The efficiency of SCT sensors is measured using reconstructed tracks and is defined to be simply the number of hits divided by the number of holes and hits. Hits are determined from SCT clusters which are formed of contiguous hits on SCT strips. Holes arise when a reconstructed track intersects with a sensor but no hit is recorded. Holes that are present due to disabled modules or chips are not included in the efficiency calculation, as their cause is well understood. The tracks used to calculate the efficiency are selected using the cuts listed and defined in Table 3.1. The $N_{trk}$ cut is introduced to reduce the overlap between multiple tracks in events being considered. The $p_T$, $\chi^2/N_{dof}$, $|d_0|$, $N_{hit}^{SCT}$, $N_{hit}^{Si}$, $N_{hit}^{IBL}$ and $N_{hole}^{Pixel}$ cuts reduce contamination from fake tracks. The $N_{hole}^{Si}$ cuts then ensures that there can be a maximum of one additional hole together with possibly one that is caused by the sensor under consideration (SUC). A particle with a trajectory that makes a large incident angle with respect to the surface of a module typically leads to the distribution of its signal across many channels. The $\phi_{inc}$ cut limits the cases in which this happens, meaning that the efficiency of the SUC is really being probed. With these tracks, the efficiency can be computed for each SCT sensor, but it is typically quoted per module. A complete description of the calculation can be found in Reference [68].

### 3.3.2 Causes of inefficiency

The calibration defects discussed in Section 3.2 are one possible cause of inefficiency due to unreliable response from the sensors. For example, if the gain of a channel is too low then a particle may not produce enough charge to exceed the threshold to register a hit. The calibration defects are used to mask strips in offline reconstruction for use in analysis, but are not masked in the efficiency calculation meaning that a loss in efficiency can be attributed to calibration defects.

Another source of inefficiency comes from noise. Some calibration defects are at-

| Parameter | Description | Cut value |
|---|---|---|
| $N_{trk}$ | Number of reconstructed tracks in event | $< 500$ |
| $p_T$ | Transverse momentum of tracks | $> 1$ GeV |
| $\chi^2/N_{dof}$ | Track fit quality | $< 3$ |
| $\|d_0\|$ | Track transverse impact parameter | $< 10$ mm |
| $N_{hit}^{SCT}$ | Number of SCT hits, excluding SUC | $\geq 6$ |
| $N_{hit}^{Si}$ | Number of total silicon hits, excluding SUC | $\geq 7$ |
| $N_{hole}^{Si}$ | Number of total silicon holes, excluding SUC | $\leq 1$ |
| $N_{hole}^{Si}$ | Number of total silicon holes, including SUC | $\leq 2$ |
| $N_{hit}^{IBL}$ | Number of hits in the Pixel IBL or B-layer | $\geq 1$ |
| $N_{hole}^{Pixel}$ | Number of holes in Pixel layers | 0 |
| $\|\phi_{inc}\|$ | Incident angle between track and sensor surface | $< 40°$ |
| $D_{cut}$ | Distance of an unassociated cluster from a reconstructed track to be considered as a hit rather than a hole | $< 200$ $\mu$m |

Table 3.1: The track selection cuts used in the SCT sensor efficiency calculation. SUC refers to the sensor under consideration.

tributed to noise but the identification of noisy strips is also performed on a per-run basis. This is done by analysing SCT hits when there is a gap in the bunch structure of the LHC beam, meaning no collisions occur (called empty bunch crossings). If the occupancy of an SCT sensor is higher than 1.5% during the empty bunch crossings in a run, then it is labelled as a noisy strip during that run. Noisy strips can be a source of inefficiency due to the '01X' readout of the SCT. For example, if an SCT sensor registers a hit due to noise in one bunch crossing, then it may miss a genuine hit in the next bunch crossing because of the veto. The noisy strip information is also used to mask strips in offline analysis.

The loss of efficiency due to the two types of problematic strips, described above, can be calculated. A simple correction factor can be defined for each module as

$$\frac{N_{total}^{strips}}{N_{total}^{strips} - N_{problem}^{strips}}, \tag{3.1}$$

where $N_{total}^{strips}$ is equal to 1536 and $N_{problem}^{strips}$ is the number of strips with a calibration defect or labelled as noisy. However this correction factor is only a simple approximation as it provides no constraint to keep the corrected efficiency below 100%. A more thorough method is to look at the overall trend of the modules in each layer

of the SCT and define a global correction. This is demonstrated in Figure 3.7 for the barrel layers of the SCT, where the measured inefficiency is plotted against the fraction of problematic strips for each module. The inefficiency is measured in a low $\langle\mu\rangle$ run in order to remove inefficiencies due to pile-up. The distribution is fitted with a straight line which is seen to well describe the relationship as the average data points for each barrel layer agree very well with the fit. Outliers which have efficiency <95% or a number of problematic strips >20 have been excluded from the fit to avoid any bias due to very problematic modules which do not reflect the general trend. This linear trend between the fraction of problematic strips and the inefficiency is used to calculate the corrected efficiency. This correction is calculated separately in the barrel and endcaps as the efficiency varies due to the larger cluster size in the barrel.

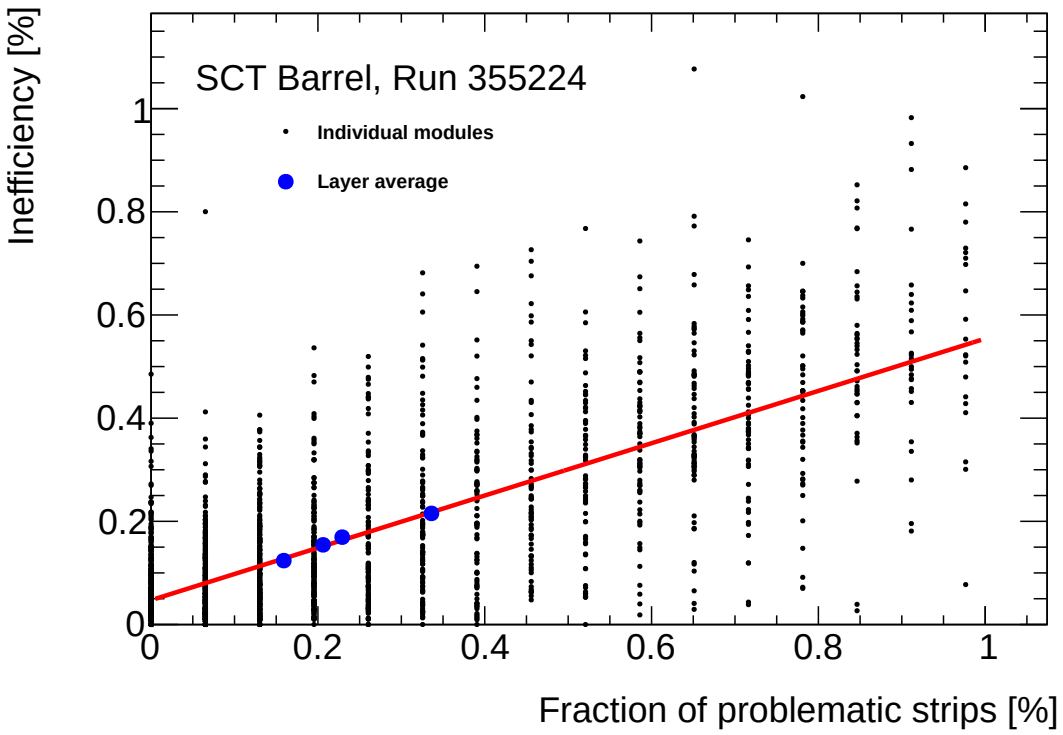


Figure 3.7: The inefficiency versus the fraction of problematic strips for the SCT barrel modules. The small black data points represent measurements from each module whereas the large blue data points represent the average for each of the four barrel layers. The red line is the fit calculated using all of the individual modules.

If the corrected efficiency of a module remains low then the source of inefficiency

could be attributed to radiation damage effects, prompting a further investigation into that particular module. A HV scan of that module could therefore be used to see whether the voltage applied to the sensors needs to be increased.

### 3.3.3 Performance Analysis Tool

The Performance Analysis Tool (PAT) compiles the information from the offline efficiency calculation, offline noisy strip calculation and online calibration defects database into one central database. The calculation of the corrected efficiency is also performed during the upload to the central database. The database can then be queried to investigate individual modules or produce summary plots, for example Figure 3.7.

A web display is also provided which gathers information from the database and displays it in a readable way. A screenshot of the display is shown in Figure 3.8. The web display is intended for regular use during data-taking periods in order to catch inefficient modules as quickly as possible and prompt investigation into understanding the inefficiency.

**SCT Performance Analysis Tool**

Run: 364292
Order by: Efficiency
Submit

**Run: 364292 2018-10-23 12:56:06**

Hitmaps ROOT file: /home/sctcalib/Results/data18_13TeV/calibration_SCTNoise/00364292/data18_13TeV.00364292.calibration_SCTNoise.sctcal.NOISYSTRIP.c0_c0
/data18_13TeV.00364292.calibration_SCTNoise.sctcal.NOISYSTRIP.c0_c0._0001.SCTHitMaps.root.1

| Serial | Efficiency | Corrected Efficiency | Dead Strips | Bad Strips | Noisy Strips | Problem Strips | Hitmaps |
|---|---|---|---|---|---|---|---|
| 20220380200227 → | 0.489920 | 0.491211 | 1 | 1 | 0 | 2 | SCTB/0_3_22_3_0, SCTB/0_3_22_3_1 |
| 20220170200584 → | 0.551107 | 0.695249 | 2 | 414 | 0 | 416 | SCTB/0_1_20_4_0, SCTB/0_1_20_4_1 |
| 20220240100642 → | 0.594693 | 0.612095 | 30 | 5 | 0 | 34 | SCTEA/2_2_8_2_0, SCTEA/2_2_8_2_1 |
| 20220270300235 → | 0.809230 | 0.817842 | 6 | 8 | 4 | 16 | SCTEC/-2_2_21_1_0, SCTEC/-2_2_21_1_1 |
| 20220130000521 → | 0.860625 | 1.022560 | 10 | 321 | 0 | 330 | SCTEC/-2_0_1_0_0, SCTEC/-2_0_1_0_1 |
| 20220330200305 → | 0.871215 | 0.967739 | 9 | 269 | 0 | 278 | SCTB/0_0_15_1_0, SCTB/0_0_15_1_1 |
| 20220270300301 → | 0.908247 | 0.911001 | 3 | 0 | 1 | 4 | SCTEA/2_2_10_1_0, SCTEA/2_2_10_1_1 |
| 20220240100552 → | 0.911226 | 0.975991 | 2 | 250 | 5 | 131 | SCTEC/-2_0_25_1_0, SCTEC/-2_0_25_1_1 |
| 20220390001004 → | 0.919069 | 0.984322 | 3 | 180 | 57 | 132 | SCTEC/-2_2_11_0_0, SCTEC/-2_2_11_0_1 |
| 20220130000368 → | 0.923166 | 0.975236 | 1 | 104 | 0 | 105 | SCTEC/-2_3_9_0_0, SCTEC/-2_3_9_0_1 |
| 20220040200242 → | 0.925625 | 0.983159 | 4 | 161 | 0 | 165 | SCTB/0_0_30_-2_0, SCTB/0_0_30_-2_1 |
| 20220240100539 → | 0.925728 | 0.929946 | 4 | 1 | 2 | 7 | SCTEC/-2_3_34_2_0, SCTEC/-2_3_34_2_1 |
| 20220170200324 → | 0.937941 | 1.003410 | 21 | 165 | 3 | 188 | SCTB/0_1_29_-6_0, SCTB/0_1_29_-6_1 |
| 20220130000261 → | 0.939206 | 1.009830 | 6 | 135 | 2 | 143 | SCTEA/2_7_12_0_0, SCTEA/2_7_12_0_1 |
| 20220240100334 → | 0.939458 | 0.940746 | 0 | 1 | 0 | 1 | SCTEA/2_0_11_1_0, SCTEA/2_0_11_1_1 |
| 20220130000232 → | 0.940013 | 0.981340 | 81 | 1 | 1 | 83 | SCTEA/2_7_51_0_0, SCTEA/2_7_51_0_1 |

Figure 3.8: A screenshot of the Performance Analysis Tool display. The worst offending modules, in terms of low efficiency, are displayed for run 364292. For some modules it is seen that the efficiency is recovered when taking into account the problematic strips, i.e. the corrected efficiency.

# CHAPTER 4

# Common Analysis Methods

This chapter covers the areas of data analysis which are common between the $pp \to Z(\to \ell\ell)\gamma + X$ and $pp \to Z(\to \ell\ell)\gamma\gamma + X$ analyses. Commonalities include both analyses having the same final state objects, and that both analyses perform fiducial cross-section measurements. The full chain of how to get from the data recorded by ATLAS to fiducial cross-section measurements will be outlined, starting with how events are triggered in the detector. The reconstruction of electrons, muons and photons will be described along with how these objects are calibrated and corrected in data and simulation. An overview of the selections applied to the data will be given along with an introduction to the backgrounds which contribute to both processes. The methods for extracting the cross-sections from the selected data will then be described. Finally, there is a discussion of the uncertainties which are considered in both analyses.

## 4.1 Triggers

In order to select $\ell\ell\gamma(\gamma)$ events, at least one of the particles must fire a trigger so that the event is saved to disk. Both analyses use single lepton triggers in order to tag the $Z$ boson. A selection of different single lepton triggers is used, and the ones with the lowest $p_{\mathrm{T}}$ threshold define the minimum $p_{\mathrm{T}}$ for leptons used in the analysis. For both channels this is 26 GeV, which is expected to be suitable as leptons coming from $Z$ decays typically have large $p_{\mathrm{T}}$ values. However, in order to keep the rates low enough to be able to save every event, the triggers must also include additional identification or isolation cuts. These additional cuts can affect the trigger efficiency at higher $p_{\mathrm{T}}$, so supplementary triggers are included which have higher $p_{\mathrm{T}}$ cuts but looser identification and isolation cuts.

Lepton triggers are preferred over photon triggers as the rates of single photon processes are much larger, meaning that higher photon $p_{\mathrm{T}}$ cuts or tighter object identification cuts are introduced at the trigger level, which brings in complications to the fake photon background estimations, which are described in Sections 5.2.1 and 6.2. The triggered events in data define a very loose sample, which is common to both analyses, to which further selection requirements are applied in order to select the photons and to emphasise the process of interest.

### 4.1.1 Electron trigger

The electron trigger [72] begins at L1, where coarse regions of the EM calorimeter are used to identify regions of interest (RoI) based on transverse energy ($E_{\mathrm{T}}$) measurements. A sliding window algorithm scans regions of 4×4 cell trigger towers, which correspond to 0.1×0.1 in $\eta \times \phi$. If the $E_{\mathrm{T}}$ measurement in the core (2×2) of the window exceeds a certain threshold (typically 22 GeV) then a RoI is identified. To reject RoIs initiated by hadronic signatures, an isolation requirement can be imposed on the outer 12 trigger towers, and a cut on the leakage into the hadronic calorimeter can also be included at L1.

The RoIs are then passed to the HLT, which uses information from the tracking systems and a finer granularity in the calorimeter. EM clusters are seeded from the cell with the largest $E_{\mathrm{T}}$ measurement in the second layer of the EM calorimeter, in the RoI. A sliding window of size $3\times7$ ($0.075\times0.175$ in $\eta\times\phi$), centred on the seed cell and all its immediate neighbours, is used to confirm that the local maximum is found. The largest $E_{\mathrm{T}}$ value from the sliding window is then taken as the energy of the cluster. The clusters are required to be matched to a track to within $|\Delta\eta| < 0.05$ and $|\Delta\phi| < 0.05$. A likelihood discriminant is used to identify electrons based on shower shapes, which is similar to the offline reconstruction described later in Section 4.2.5.1. A track-based isolation variable can also be included at the trigger level, which requires the sum of track $p_{\mathrm{T}}$ around the electron to be less than 10% of the electron track $p_{\mathrm{T}}$.

The efficiency of the trigger is measured using a tag-and-probe method in $Z \to ee$ decays [73]. In this method, two electrons are required to be selected, with an invariant mass within 15 GeV of the $Z$ mass. One of the electrons must be matched to the trigger object which fired the trigger (within $\Delta R < 0.07$) and pass Tight identification requirements (described in Section 4.2.5.1). This electron is referred to as the tag, making the other the probe, which is used to evaluate an unbiased estimate of the trigger selection efficiency. The single electron trigger efficiencies are shown as a function of $E_{\mathrm{T}}$ in Figure 4.1 for each year of data-taking in Run-2, and compared to simulation. The trigger efficiency is not expected to be modelled perfectly in simulation due to the fact that the exact run conditions cannot be reproduced in simulation. The mismodelling is most prominent at low $E_{\mathrm{T}}$ values which are more sensitive to pile-up and resolution mismodelling effects. The ratio of data to simulated efficiency (i.e. the lower panel of Figure 4.1) is used to define scale factors, which are used to correct simulations involving electrons. In order to avoid the turn-on region, where the efficiency varies rapidly as a function of $p_{\mathrm{T}}$, leading electrons used for analysis are typically required to have $p_T > 30$ GeV.

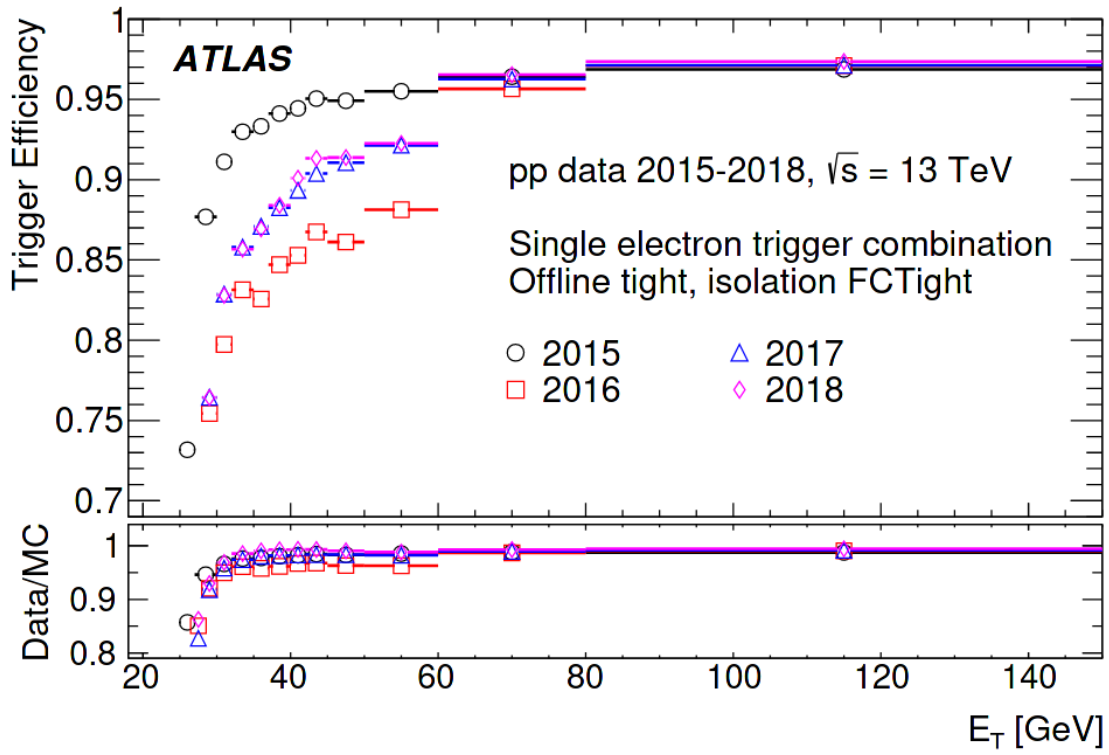


Figure 4.1: The single electron trigger efficiency as measured in $Z \to ee$ decays for each year of data-taking in Run-2 [72]. The ratio to the efficiency prediction from simulation is shown in the bottom panel.

### 4.1.2 Muon trigger

At L1, the muon trigger [74] uses coincidences among the RPCs in the barrel region and among the TGCs in the endcap regions to form RoIs. The coincidences can be used to calculate a very coarse estimate of the muon momentum which can be subject to various $p_{\mathrm{T}}$ thresholds defined at L1. The muon RoIs outlined at L1 are then reconstructed in the HLT using at first measurements from the MS only, and rejected if they are not above the required $p_{\mathrm{T}}$ threshold. The MS tracks are then extrapolated and matched to tracks in the ID, allowing for an improved reconstruction of the muon momentum. An isolation variable is constructed for the muon, using the sum of the $p_{\mathrm{T}}$ of tracks close to the muon vertex. This isolation variable is used to reduce the trigger rate of low $p_{\mathrm{T}}$ muons.

The trigger efficiency for muons is measured in data using $Z \to \mu\mu$ decays in a

similar tag-and-probe technique to that described for the electron trigger. The muon trigger efficiency as a function of muon $p_{\mathrm{T}}$ and $|\eta|$ is shown in Figure 4.2. The muon trigger efficiency is lower in the central region ($|\eta| < 1.05$) due to the limited coverage of the trigger chambers in this region. The ratio of data to simulation, shown in the lower panels of Figure 4.2, are used to define scale factors to correct the muon trigger efficiency in simulation [74].

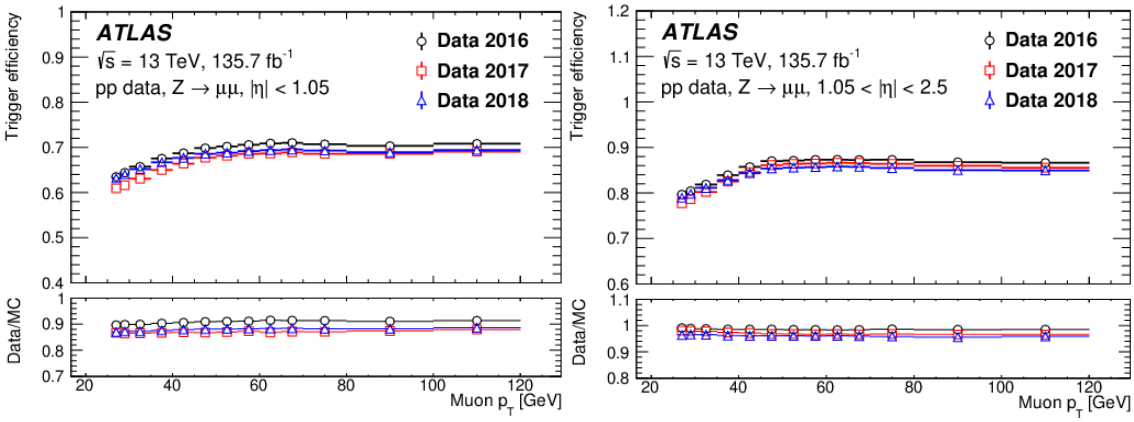


(a) (b)

Figure 4.2: The single muon trigger efficiency in the regions (a) $|\eta| < 1.05$ and (b) $1.05 < |\eta| < 2.5$ as measured in $Z \to \mu\mu$ events for separate data-taking years [74]. The ratio to the efficiency prediction from simulation is shown in the bottom panel.

## 4.2 Object reconstruction

For the events selected by the trigger, the full detector information can be processed to reconstruct the physics objects which are contained in each event. In the following, the reconstruction of photons, electrons and muons are described, which are used in the analyses presented in this thesis. In order to explain the reconstruction of these objects, the lower-level objects called tracks, vertices and calorimeter clusters are described first. The same reconstruction is performed on objects in data and simulation, and corrections are applied to simulation in order to improve the agreement between the two.

### 4.2.1 Tracks

The trajectories of charged particles in the ID are used in the reconstruction of electrons, muons and converted photons. These particles register hits in the ID sub-detectors, which are associated together to form tracks [56].

Hits on adjacent channels in the silicon trackers are grouped together to form clusters. These clusters are then turned into space-points; in the pixel detector the average position of a cluster is used, whereas in the SCT, clusters on both sides of a module are averaged to form the space-point. Combinations of three space-points are used to form seeds for the tracks themselves. From the three space-points, an approximation of the track momentum and impact parameter can be calculated and cuts are placed on these quantities along with the requirement that the seed is compatible with at least one other space-point. A combinatorial Kalman filter [75] is used to connect the seed to all other space-points which are compatible with its trajectory.

The track candidates in an event are given a ranking based on the quality of the fit, the momentum, the number of clusters and the number of holes (defined in Section 3.3.1). Momentum is used in the ranking as low $p_{\mathrm{T}}$ tracks are more likely

to have wrongly assigned clusters. Basic selection requirements are placed on the tracks, which can be found in Reference [56].

The remaining tracks are fully reconstructed using all the available silicon tracking information. These tracks are then extended into the TRT system using a simple road finding algorithm [76] to associate TRT hits to tracks. Finally, any remaining hits in the TRT are used to build track candidates from the outside-in, in order to recover tracks that are missed by the nominal tracking algorithms. This is particularly useful for photon conversions as the tracks from such a process are not compatible with originating from the primary vertex.

### 4.2.2 Vertices

Due to the high level of pile-up at the LHC in Run-2, around 30 proton-proton interactions occur during every bunch crossing. It is important to be able to reconstruct as many of the separate vertices in an event as possible, in order to determine which particles come from which interaction. The z position of a reconstructed track is used to seed a vertex and it is tested for compatibility with nearby tracks. At least one other track is required to be consistent with the seed vertex [77]. The position of the beam spot is also used to constrain the positions of the vertices. In an event, the primary vertex (PV) is selected as that which has the highest $\Sigma p_T^2$ summed over the associated tracks.

### 4.2.3 EM clusters

Clusters of energy deposits in the calorimeters are used in the reconstruction of electrons and photons [78]. A cluster is seeded by any cell which has a signal that is larger than four times the expected noise for that cell. Neighbouring cells are then added to the cluster if they have over twice the expected noise in their respective cells. Once the cluster growth is finished, a final layer of all neighbouring cells to

the finished cluster is added, regardless of the energy measurement of those cells. If two clusters overlap, then they are merged into a single cluster. Clusters are rejected if their energy is below 400 MeV or the fraction of energy in the cluster in the EM calorimeter is less than 50%, which helps to reject clusters from pile-up. The adaptive nature of these clusters, compared to the fixed-size windows used in, for example, the electron trigger, allows for the recovery of energy lost via bremsstrahlung or photon conversions.

Clusters can then be matched to tracks to reconstruct higher-level objects. A track is considered matched to a cluster if $|\Delta\eta| < 0.05$ and $-0.10 < q(\phi_{track} - \phi_{cluster}) < 0.05$. The cut on the separation in $\phi$ is asymmetric as the direction of the track will not account for any photons which are radiated after the tracking systems, and hence will be captured by the cluster. If more than one track is matched to a cluster, the tracks are ranked firstly on whether they have hits in the pixel detector and secondly by their $\Delta R$ matching to the EM cluster.

### 4.2.4 Photons

Photons are neutral particles and do not leave any hits in the tracking systems. Hence the simplest signature for a photon is an EM cluster with no associated track. However, some photons convert into an $e^+e^-$ pair when interacting with material in the tracking systems. These photons can still be reconstructed as two electron candidates of opposite sign where the two tracks form a vertex within the tracking system. Such photons are referred to as converted photons, whereas photons which enter the calorimeter without interacting are referred to as unconverted.

Clusters with no associated tracks are used to seed unconverted photons. Two track-cluster pairs which form a vertex consistent with a massless particle are used to seed converted photons. All tracks are considered, even those with only TRT hits; however these tracks must have a high probability of being an electron based on the transition radiation information from the TRT [79]. This requirement is based on

having a larger number of hits in the TRT passing a higher threshold, due to the larger amount of transition radiation emitted by electrons. Single track conversions are also formed from tracks which have a very high probability of being an electron but have no hits in the innermost silicon layers. This is done to recover photon conversions where the tracks are very close together or one of the electrons is very soft and is hence not reconstructed.

Photon candidate clusters with $E_{\mathrm{T}} > 1.5$ GeV are used to seed superclusters. Any additional cluster falling within a $0.075 \times 0.125$ ($\eta \times \phi$) cell window around the seed cluster is added to it. For converted photons, any cluster which has an associated track with the same conversion vertex as the seed is added to it.

The energy measurements of photons are calibrated in order to correct for non-uniform detector response and to align the measurements in data and simulation [80]. The corrections are applied to improve the scale and resolution of the energy measurements. The impact of the uncertainties associated with these corrections are considered in the final results.

#### 4.2.4.1 Photon identification

Further requirements are placed on photon objects to separate prompt photons from jets faking photons. The separation is based on certain shower shape variables determined in the calorimeters. The distinction relies on the facts that prompt photons tend to produce more collimated deposits and these deposits have a smaller leakage into the hadronic calorimeter. The strip layer of the EM calorimeter is also used to reject photons coming from $\pi^0 \to \gamma\gamma$ decays, as the finer granularity in $\eta$ allows the identification of two close-by energy peaks. The variables used and their definitions are given in Table 4.1. The working points which place cuts on the various variables are also given. The cut values used for each variable are optimised separately for unconverted and converted photons, for different $\eta$ ranges and for different photon $E_T$ values.

| Variable | Description | Working points |
|---|---|---|
| $R_{had}$ | Ratio of $E_T$ in the hadronic calorimeter to $E_T$ of the EM cluster | *Tight, LP2, LP3, LP4, LP5, Loose* |
| $R_\eta$ | Ratio of 3×7 to 7×7 cell energies ($\eta \times \phi$) | *Tight, LP2, LP3, LP4, LP5, Loose* |
| $w_{\eta 2}$ | Lateral width of the shower in second calorimeter layer | *Tight, LP2, LP3, LP4, LP5* |
| $w_{tots1}$ | Total lateral shower width in strip calorimeter layer | *Tight, LP2, LP3, LP4* |
| $E_{ratio}$ | Ratio of energy difference between largest and second largest deposits to the sum of these energies | *Tight, LP2, LP3* |
| $\Delta E$ | Difference between the energy of the second maximum and the lowest energy between the first and second maximum in the strip layer | *Tight, LP2* |
| $F_{side}$ | Energy outside the central three strips but within seven strips, divided by the energy within central three strips | *Tight* |
| $w_{s3}$ | Lateral shower width calculated from three strips around the strip with the highest energy deposit in strip layer | *Tight* |
| $R_\phi$ | Ratio of 3×3 to 3×7 cell energies ($\eta \times \phi$) | *Tight* |

Table 4.1: The shower shape variables used to define the various photon ID working points. *LP* is shorthand for *LoosePrime*.

The photon identification requirements are used to study the rates at which jets are misidentified as photons, the techniques for which are first introduced in Section 4.3.1. Jet-enriched control regions are defined by inverting the *Tight* identification cuts, i.e one of the cuts listed in Table 4.1 must fail. However, some of these cuts are particularly correlated with the photon isolation cuts, introduced in the next section, primarily those based on larger areas of the calorimeter (for example $w_{\eta 2}$ and $R_\eta$). Therefore a jet which fails one of these cuts is more likely to fail the photon isolation cuts. In order to reduce the correlation between the photon identification and isolation for jets misidentified as photons, the *LoosePrime* working points are introduced which require the most correlated cuts to be satisfied. The closer to *Tight* the working point is, the less correlated it is at the expense of a smaller sample size.

#### 4.2.4.2 Photon isolation

The photon isolation requirements are motivated by the fact that there should be little activity near to a prompt photon in the tracking and calorimeter environments. The calorimeter isolation is intrinsically correlated with some of the variables used in the definition of the identification working points as discussed in the previous section. However in general, the isolation variables are calculated over a much larger area surrounding the photon. These analyses use the *FixedCutLoose* isolation working point, which is chosen as it is robust to the effects of high pile-up. Two variables are used in the definition of the working point:

- $p_T^{cone20}$, the scalar $p_{\mathrm{T}}$ sum of $p_T > 1$ GeV tracks which originate from the PV and are within a cone of $\Delta R < 0.2$ around the photon direction.
- $E_T^{cone20}$, the sum of $E_T$ of calorimeter clusters within a cone of $\Delta R < 0.2$ around the photon direction. The energy of the photon itself is subtracted by summing the energy deposits in a $5 \times 7$ cell window centred on the photon, which is itself corrected with a $p_T$-dependent leakage correction. Finally an $\eta$-dependent correction is applied to account for ambient activity in the calorimeter using the median jet energy density of all EM clusters in the event, with no $p_{\mathrm{T}}$ threshold.

The cuts which define the *FixedCutLoose* working point scale with the transverse momentum of the photon ($p_T^\gamma$), and they are $p_T^{cone20} < 0.05 \times p_T^\gamma$ and $E_T^{cone20} < 0.065 \times p_T^\gamma$. Further details of the detector-level photon isolation are given in Section 5.3.

#### 4.2.4.3 Scale factors

Some properties of photons in the simulation do not match those which are measured in data, e.g. the photon isolation and identification efficiencies. In order to correct for this mismodelling, scale factors are derived which can be applied as weights in

simulation to better describe the data. Scale factors are derived using $Z \to \ell\ell\gamma$ events which are a clean source of photons due to the $m_{\ell\ell\gamma} \sim m_Z$ requirement. Inclusive photon events (i.e. $\gamma + X$) are also used, which provide significantly more events but suffer from larger backgrounds that result in larger systematic uncertainties. The scale factors are derived as functions of photon $p_{\mathrm{T}}$, $\eta$ and conversion type. An example is shown in Figure 4.3, where it is seen that the isolation efficiency scale factors are small for the *FixedCutLoose* (*Loose*) working point. The systematic uncertainties associated to the scale factors are discussed in Reference [78].

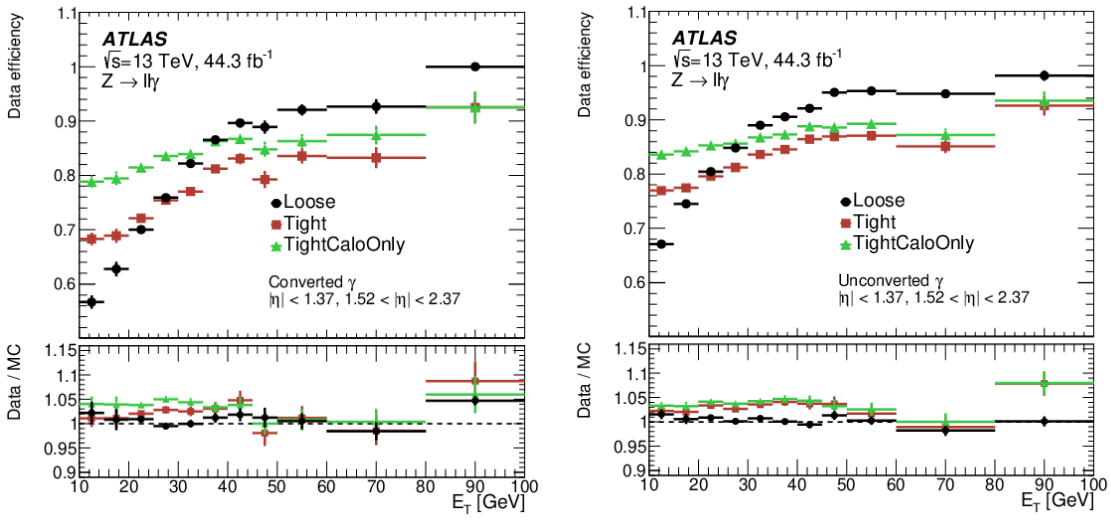


(a) (b)

Figure 4.3: The photon isolation efficiency as a function of $E_T$ for (a) converted and (b) unconverted photons [78]. The lower panels display the ratio of the efficiency in data to the efficiency in simulation.

### 4.2.5 Electrons

The reconstructed tracks and EM clusters are used as input to the electron reconstruction [81]. Of the reconstructed cluster-track pairs, the ones with $E_{\mathrm{T}} > 1$ GeV and hits in at least 4 silicon layers are used as electron seed clusters, to which additional clusters are added to form superclusters. Any additional clusters that fall within a 3×5 cell window of the seed cluster are added to the energy measurement in order to recover energy dispersed in the EM shower. In addition to this, any other

cluster which is matched to the same track as the seed is also added to the electron supercluster. The energy measurements of electrons are then calibrated in a similar way to photons but instead using $Z \to ee$ decays in data, which are used as a clean source of electrons.

#### 4.2.5.1 Electron identification

Further requirements can be placed on the electron objects in order to distinguish prompt electrons from jets faking electrons, and electrons from heavy hadron decays. A likelihood discriminant is formed using variables characterising the impact parameter, EM shower shape and TRT transition radiation of the electron. From this discriminant, three working points are defined in order of electron quality: *Loose*, *Medium* and *Tight*, which have increasing background rejection at the expense of signal efficiency [81].

#### 4.2.5.2 Electron isolation

The electron calorimeter isolation variable is built in the same way as for photons. The track-based isolation variable is constructed using tracks which are selected using the same requirements as for the photon track isolation variable. However, a variable cone size is used which is inversely proportional to the electron $p_{\mathrm{T}}$, meaning that the requirement becomes tighter for lower $p_{\mathrm{T}}$ electrons. This improves the rejection against jet misidentified as electron backgrounds which are more prominent at low $p_{\mathrm{T}}$. However, electrons from heavy hadron decays are more prominent at high-$p_{\mathrm{T}}$, so above 50 GeV a fixed cone of size $\Delta R < 0.2$ is used which stops the isolation cut becoming too loose.

### 4.2.6 Muons

For the analyses presented in this thesis, muons are only considered in the region $|\eta| < 2.5$ and are reconstructed with information from the MS and ID. Such muons are referred to as *Medium* quality, but other working points are available [82, 83]. Track segments in the MS are required to have at least three hits on at least two layers of the MDT, except in the $|\eta| < 0.1$ region, where this requirement is only for one layer as the MDT coverage in this region is hampered by services to the ID and calorimeters. The MS track segments are required to be spatially compatible with a track in the ID after extrapolation, and the muon momentum measurements of the tracks are required to be consistent. The reconstruction efficiency of muons is measured using a tag-and-probe method. The momentum scale and resolution of muons in simulation are corrected by comparison with $Z \to \mu\mu$ and $J/\psi \to \mu\mu$ decays in data [83].

#### 4.2.6.1 Muon isolation

Muons are required to be isolated from other physics objects in an event in order to reject muons originating from hadron decays. The isolation variable constructed has a neutral term and a charged term. The charged term consists of the scalar sum of the $p_{\mathrm{T}}$ of all tracks with $p_T > 500$ MeV and consistent with originating from the same vertex as the muon. For muons with $p_T < 50$ GeV, this is calculated in a variable sized cone, which is inversely proportional to the muon $p_{\mathrm{T}}$. For muons with $p_T > 50$ GeV, a fixed cone size of $\Delta R < 0.2$ is used, which ensures the isolation requirement does not get too loose for muons from heavy hadron decays. The neutral component to the isolation variable comes from the sum of $E_T$ of all clusters which are not matched to a track in a cone of $\Delta R < 0.2$ around the muon. The ratio of this variable to the measured $p_{\mathrm{T}}$ of the muon can then be used to define different muon isolation working points. The muon isolation efficiency is calculated using a tag-and-probe method in $Z \to \mu\mu$ decays.

## 4.3 Selection and backgrounds

Using the physics objects detailed in the previous section, further selection requirements can be implemented in order to enhance the process of interest. Some of the selection requirements are chosen to reflect the limits of the detector, for example the geometrical acceptance or ensuring the lepton $p_{\mathrm{T}}$ is above the trigger threshold. The final set of selection criteria defines a region of phase space which is known as the signal region (SR), and this is detailed for the separate analyses in their respective chapters. Both analyses presented in this thesis use inclusive final states, i.e. no further requirements are placed on other objects within the event. For example, the process being studied in the $Z\gamma$ analysis is really $pp \to Z(\to \ell\ell)\gamma + X$, where $X$ denotes any other particles. This avoids the introduction of large uncertainties due to the reconstruction of other objects, such as jets.

The SR will inevitably contain contributions from other processes besides the desired process, which are referred to as backgrounds. Backgrounds which contain exactly the same final state as the process of interest and originate from the primary vertex, but are produced via a different interaction, are known as prompt backgrounds. An example of a prompt background for $Z\gamma(\gamma)$ is $t\bar{t}\gamma(\gamma)$, where the top quarks decay leptonically to an opposite-sign same-flavour (OSSF) lepton pair. This produces the $\ell\ell\gamma(\gamma)$ signal final state so its contribution to the SR is unavoidable. The other category of background events is known as non-prompt backgrounds. These types of processes involve the mis-identification of objects and can therefore be suppressed by introducing selection cuts. Three types of backgrounds which are common to both analyses are introduced in the following sections. There are other smaller backgrounds included in both analyses which are estimated directly from simulation.

### 4.3.1 Fake photon backgrounds

The main source of background in both analyses is from jets misidentified as photons (fake photons). These processes are not well modelled by simulation, so methods

which estimate these backgrounds using data are deployed. The methods make use of jet-enriched samples where the photon isolation and identification cuts are removed. The photon candidates are required to pass the *LoosePrime4* identification working point (defined in Section 4.2.4.1) in order to reduce the correlation between identification and isolation of the fake photon candidates. Each photon candidate can then be placed into one of four categories:

- A: The candidate passes both the isolation and identification cuts
- B: The candidate fails the isolation cut but passes the identification cut
- C: The candidate passes the isolation cut but fails the identification cut
- D: The candidate fails both the isolation and identification cuts

Region A contains mostly prompt photons and some fake photons, whereas B, C and D consist mainly of fake photons. In order to reduce signal photons leaking into the background control regions, a buffer labelled $E_{gap}$ is added to the requirement to fail the isolation cut: $E_T^{iso} > 0.065 \times E_T^{\gamma} + E_{gap}$. This therefore reduces the leakage into regions B and D only. A nominal value of $E_{gap} = 2$ GeV is used. Events containing photons which have a value of $E_T^{iso} - 0.065 \times E_T^{\gamma}$ between 0 and 2 GeV are hence not used in the estimation of the fake photon backgrounds.

The methods deployed are fully described in Sections 5.2.1 and 6.2 respectively.

### 4.3.2 Pile-up backgrounds

Many photons, particularly unconverted photons, suffer from poor vertex resolution due to the fact that only calorimeter information is available. For this reason, no primary vertex compatibility requirement is placed on the photon in these analyses. This does however introduce another source of background where the photon(s) comes from a different vertex to the $Z$ in the same LHC bunch crossing. This

happens at a non-negligible rate (accounts for a few percent of events in the signal region) due to the high pile-up environment in LHC Run-2.

Data-driven methods can be explored which utilise converted photons, that have good vertex resolution, in order to estimate the rate at which such overlaps occur. The distributions associated with these processes can be modelled by randomly overlaying simulated events from each process. For example, for $Z\gamma$ this would be an inclusive $Z$ event overlapping with an inclusive $\gamma$ event. The overlay is done at the truth level (see Section 4.4), then events are required to pass the same selection as the signal process.

### 4.3.3 Top backgrounds

The largest prompt background for both $Z\gamma$ and $Z\gamma\gamma$ comes from $t\bar{t}+\gamma(\gamma)$ processes where both top quarks decay leptonically. In both analyses, the normalisation of this background is estimated with a data-driven approach and the distributions are taken from simulation. The normalisation is constrained in a control region where an opposite-sign different-flavour lepton pair ($e^{\pm}\mu^{\mp}$) is selected that removes any contribution from the signal process. The derived normalisation is then applied to the $t\bar{t}\gamma(\gamma)$ MC in the signal region.

## 4.4 Cross-section extraction

The total number of events selected in data is denoted as $N_{data}$. To extract the number of events corresponding to the signal process, the total number of predicted background events, $N_{bkg}$, is subtracted from the data: $N_{sig} = N_{data} - N_{bkg}$. In order to make a measurement easily comparable to results from other experiments and various theoretical predictions, the measured number of signal events is converted to a cross-section measurement. In addition to this, the cross-section is corrected to a fiducial phase-space which reduces effects from the inefficiency, acceptance and

resolution of the detector. The integrated fiducial cross-section ($\sigma_{fid}$) is calculated as:

$$\sigma_{fid} = \frac{N_{data} - N_{bkg}}{C \times L}, \tag{4.1}$$

where $L$ is the measured integrated luminosity and $C$ is the factor used to correct the data yield from the detector level to the fiducial level. The fiducial-level phase space is defined in terms of particles in the simulation, which are also referred to as truth-level particles. The truth-level particles used in the fiducial selection are required to be stable, meaning that they have a mean lifetime of $c\tau > 10$ mm. The fiducial-level selection is defined so as to resemble the detector selection as closely as possible, to minimise the dependence on the model used for the simulation of the signal events. The factor $C$ is then simply the ratio of the number of events in the signal MC selected using the detector-level selection on reconstructed objects, to the number of selected events using the fiducial-level selection on truth-level particles. Not all fiducial-level events will pass the detector-level selection due to inefficiencies, which results in $C$ being less than one. It also accounts for the much smaller contribution of detector-level events which do not pass the fiducial-level selection.

### 4.4.1 Unfolding

The fiducial cross-sections of processes are also measured differentially, in order to test regions of phase space which are, for example, poorly modelled or particularly sensitive to contributions from higher order QCD corrections or new physics. To do this, both $N_{data}$ and $N_{bkg}$ need to be estimated in bins of each variable of interest. A simple way of calculating the differential fiducial cross-section would then be to calculate values of $C$ in each of the bins and apply these corrections to the background-subtracted yields; this is known as the bin-by-bin approach. This, however, does not take into account fiducial events which are reconstructed in a different bin from that in which they were generated due to migrations arising from resolution effects.

The number of events measured in bin $i$ of a detector-level variable is given by $d_i$, and the number of events in bin $j$ of the corresponding fiducial-level variable is given by $f_j$. The relationship between the two is given by $d_i = R_{ij} f_j$ where $R_{ij}$ is the response matrix, which includes the bin migrations in the off-diagonal elements. The response matrix can be calculated from the signal MC, which contains both truth-level and detector-level objects. The response matrix can be inverted in an iterative Bayesian unfolding approach detailed in References [84, 85, 86]:

$$f_j^{r+1} = f_j^r \sum_{i=1}^{n} \frac{R_{ij}}{\epsilon_j} \frac{d_i}{\sum_{k=1}^{n} R_{ik} f_k^r}, \tag{4.2}$$

where $i, j \in 1, n$ represents the number of bins in the distributions, and $r$ is the number of iterations. An efficiency factor, $\epsilon_j$, accounts for acceptance losses. The 'best guess' of the fiducial distribution for each iteration $r$ is given as $f_j^r$ and is used as the input to the $r + 1^{th}$ iteration, along with $d_i^r$ which is this fiducial distribution multiplied by the response matrix. The iterative approach implies that there is an initial version of the truth distribution, i.e. $r = 0$, and this is typically taken from the signal MC, although the bias in using this is checked. The unfolded distributions can then be compared to predictions and experiments in a phase space where any biases due to the detector are reduced.

### 4.4.2 Uncertainties

The uncertainties on the measured cross-sections which are considered are listed below. The uncertainties due to MC statistics, pile-up reweighting and physics object reconstruction are assessed by varying features of the signal MC simulation and propagating these to the integrated cross-section through the correction factor $C$. They are fully propagated through the unfolding procedure to estimate uncertainties for the differential cross-sections.

Data statistical uncertainty: The Poisson statistical uncertainty on $N_{data}$ can be directly propagated through the calculation of the integrated cross-sections. For the differential cross-sections, the data statistical uncertainty is estimated by repeating the unfolding procedure on $N$ sets of data which are formed by randomly sampling from the original distributions. The standard deviation of the $N$ results in a particular bin is taken as the statistical uncertainty in that bin.

Background uncertainties: The uncertainty on the number of background events in each bin, $N_{bkg}$, is taken as the quadrature sum of the uncertainties of the individual sources of background. The uncertainties for each background are discussed in Sections 5.2, 6.2 and 6.3.

Luminosity uncertainty: The integrated luminosity of 139 $\text{fb}^{-1}$and its corresponding 1.7% uncertainty are measured according to the procedure detailed in Reference [63].

Monte Carlo statistical uncertainty: The uncertainty due to the limited number of signal MC events is included. This is particularly important for the differential measurements as the generation of MC events is not uniform across all bins.

Pile-up reweighting uncertainty: The distribution of the pile-up in the MC is reweighted such that it matches that of the data. This is done separately for the periods of 2015-2016, 2017 and 2018, as the pile-up profiles were significantly different in these three periods (Figure 2.3). The uncertainty associated with this reweighting is considered.

Physics object reconstruction uncertainties: The uncertainties on the reconstruction, isolation and identification efficiencies of electrons, muons and photons are considered by varying the scale factors related to these objects. The uncertainty on the trigger efficiencies of electrons and muons are also considered. Additionally, the uncertainty on the energy scale and resolution corrections applied to EM clusters

are propagated by varying the scale factors within their uncertainties.

#### 4.4.2.1 Channel combination

To improve the precision of the measurements and to provide a simpler interpretation, the measurements in the electron and muon channels are combined into $\ell\ell\gamma(\gamma)$ measurements. In order to do this, the uncertainties are divided into those which are correlated between the channels and those which are uncorrelated. The statistical uncertainties and those specific to the reconstruction of electrons or muons are uncorrelated, and the rest, primarily the uncertainties related to the backgrounds, are correlated. A $\chi^2$ minimisation is performed whilst allowing the average value, and each of the correlated uncertainties to float, so that the average value determined best describes the data in each channel. The uncorrelated uncertainties are naturally constrained in the averaging procedure. A full description of the method can be found in Reference [87].

# CHAPTER 5

# Measurements of $Z(\rightarrow \ell\ell)\gamma$ Production

This chapter presents the selection of $Z(\rightarrow ee)\gamma$ and $Z(\rightarrow \mu\mu)\gamma$ events from $pp$ collision data, the estimation of the backgrounds contributing to these processes and the fiducial cross-section results.

The detector and fiducial selections are detailed in Section 5.1 along with a description of the data and signal samples used. The backgrounds and techniques used to estimate them are given in Section 5.2. The role of photon isolation in the analysis is explained in Section 5.3. Finally, the results are given in Section 5.4.

## 5.1 Selections and samples

### 5.1.1 Detector-level selection

The following describes the signal region (SR) selection. As explained in Section 4.1, events are selected which fire one of the single lepton triggers. These events are required to have at least one vertex reconstructed (as detailed in Section 4.2.2), and the one with the highest $\Sigma p_T^2$ is chosen as the primary vertex (PV).

The preselection requirements placed on all electron objects are:

- $p_{\mathrm{T}} > 25$ GeV
- $|\eta| < 2.47$ and not within $1.37 < |\eta| < 1.52$
- consistency with tracks originating from the PV
- *Medium* electron identification criteria
- *Loose* electron isolation criteria

The preselection requirements placed on all muon objects are:

- $p_{\mathrm{T}} > 25$ GeV
- $|\eta| < 2.5$
- consistency with tracks originating from the PV
- *Medium* muon identification criteria
- *Loose* muon isolation criteria

The preselection requirements placed on all photon objects are:

- $p_{\mathrm{T}} > 15$ GeV

- $|\eta| < 2.37$ and not within $1.37 < |\eta| < 1.52$

- *Loose* photon identification criteria

The pseudorapidity preselection requirements reflect the geometrical acceptance of the detector. The region $1.37 < |\eta| < 1.52$ is excluded for electrons and photons as this corresponds to the transition region between the barrel and endcap coverage of the EM calorimeter. In this region, there is a lot of additional material in front of the calorimeter, so the energy measurements are not accurate. The remaining preselection criteria for leptons are chosen such that they are not tighter than the requirements placed at the trigger level, which results in the most inclusive sample possible. The minimum photon $p_{\mathrm{T}}$ cut is limited by the available MC. Only the *Loose* identification criteria is applied at this stage such that events can be separated into the signal region and control regions for the estimation of the fake photon background. Photons are removed if they are within $\Delta R < 0.4$ of an electron or muon and electrons are removed if they are within $\Delta R < 0.2$ of a muon, to suppress contributions from bremsstrahlung photons. Events are considered further if they contain at least two reconstructed electrons or muons and at least one reconstructed photon passing the preselection requirements.

In either channel, the leading lepton is required to have $p_{\mathrm{T}} > 30$ GeV in order to be above the single lepton trigger thresholds. The highest $p_{\mathrm{T}}$ opposite-sign same-flavour lepton pair is then selected as the $Z$ candidate and is required to have an invariant mass of $m_{\ell\ell} > 40$ GeV to remove contributions from low mass Drell-Yan production and resonances. In the signal region, the photon must also pass the *FixedCutLoose* isolation cut and the *Tight* identification cut (defined in Section 4.2.4). The highest $p_{\mathrm{T}}$ photon is selected, and must have $p_{\mathrm{T}} > 30$ GeV to suppress the contribution and large uncertainty from the fake photon background, which are both larger at low $p_{\mathrm{T}}$. Finally, the contribution from FSR photons is removed by requiring that the sum of the dilepton and three-body invariant masses is more than twice the $Z$ mass: $m_{\ell\ell} + m_{\ell\ell\gamma} > 2m_Z$, as demonstrated in Figure 1.6.

### 5.1.2 Fiducial-level selection

The fiducial-level selection is designed to be as close as possible to the detector-level selection, and is based on truth-level objects (defined in Section 4.4) as opposed to detector-level objects. The truth-level lepton objects considered are 'dressed' which means that the four-momenta of any photons within $\Delta R < 0.1$ are added to the lepton, in order to catch any energy which would be reconstructed as part of the same cluster in the calorimeter system. From a theoretical perspective, the dressing procedure also mimics the resummation of higher-order QED effects, which avoids divergences in the calculation. A common lepton selection is applied to both channels, which allows for a much simpler combination of the channels.

The truth-level lepton selection requirements are:

- leading lepton $p_{\mathrm{T}} > 30$ GeV
- subleading lepton $p_{\mathrm{T}} > 25$ GeV
- $|\eta| < 2.47$
- $m_{\ell\ell} > 40$ GeV

The truth-level photon selection requirements are:

- $p_{\mathrm{T}} > 30$ GeV
- $|\eta| < 2.37$
- $\Delta R(\gamma, \ell) > 0.4$
- $E_T^{cone20}/E_T^{\gamma} < 0.07$

The truth-level photon isolation variable $E_T^{cone20}$ is defined in Section 5.3.2, along with the optimisation of the cut which is placed on it. Finally, the contribution from the FSR production of photons is removed by requiring the same selection as applied at the detector level: $m_{\ell\ell} + m_{\ell\ell\gamma} > 2m_Z$.

### 5.1.3 Data and signal samples

The data used correspond to an integrated luminosity of 139 fb$^{-1}$, recorded from $pp$ collisions at $\sqrt{s} = 13$ TeV between 2015-2018. Any data which are recorded when any component of the detector is not fully functional are not considered.

The baseline $pp \to \ell\ell\gamma$ signal samples are generated using the Sherpa MC event generator [16]. The matrix elements are calculated at leading-order (LO) with up to three additional partons. The matrix element partons are matched to the Sherpa parton shower [19] using the ME+PS@LO prescription [88, 89, 90, 91]. The NNPDF3.0 NNLO PDF set [30] is used to describe the parton content of the incoming protons.

The samples are generated in slices of $p_T^\gamma$ to ensure there are a sufficient number of MC events across the entire $p_{\mathrm{T}}$ range being probed. As the matrix element is only calculated at LO accuracy, it is expected that the signal samples do not provide an accurate description of the data, due to the missing higher-order corrections. The normalisation of the LO sample can be improved by multiplying the expected yields and distributions by a normalisation factor (k-factor). The k-factor is calculated as the ratio of data or a higher order MC to the LO sample.

Alternative samples are generated with MadGraph [17] and Sherpa [92] at NLO which are used to cross-check the modelling and unfolding. These samples are not considered as the baseline as they are much more CPU-intensive to generate, hence they suffer from a significantly smaller number of events compared to the Sherpa LO samples.

## 5.2 Backgrounds

### 5.2.1 Fake photon background

The main source of background to $\ell\ell\gamma$ is from events with a $Z$ and a jet faking a photon. This process is not well modelled by simulation, so a data-driven method is used to estimate the amount of background. The 2D-sideband method is used which makes use of the four jet-enriched control regions (CRs); A, B, C and D, defined in Section 4.3.1. The number of data events in the signal region ($N_A^{data}$) can be written as

$$N_A^{data} = N_A^{sig} + N_A^{fake} + N_A^{bkg}, \tag{5.1}$$

where $N_A^{sig}$ is the number of signal events in the signal region, $N_A^{fake}$ is the number of fake photon events in the signal region and $N_A^{bkg}$ is the contribution from other background processes in the signal region.

The method works on the assumption that the ratio of the number of fakes in regions A and B is the same as that in C and D. In practice, this is not exactly true as the isolation and identification variables are correlated, as discussed in Section 4.2.4.1. To account for this correlation, the factor $R$ is defined as

$$R = \frac{N_A^{fake} N_D^{fake}}{N_B^{fake} N_C^{fake}}, \tag{5.2}$$

which is calculated from $Z$+jets MC events and found to have a value of 1.33±0.09. The uncertainty on $R$ is taken as the difference between data and simulation in a control region where the photon candidate fails the track isolation cut. The value of $R$ is then substituted into the signal region equation:

$$N_A^{data} = N_A^{sig} + R\frac{N_B^{fake} N_C^{fake}}{N_D^{fake}} + N_A^{bkg}. \tag{5.3}$$

The control regions B, C and D are expected to be dominated by fakes, but there are also small contributions from the signal and other backgrounds containing prompt

photons. The prompt photon backgrounds are estimated directly from simulation, whereas for the signal, leakage factors $c_i = N_i^{sig}/N_A^{sig}$ are used such that the amount of signal leakage depends on the amount of signal present in the signal region. The signal leakage factors are calculated directly from the signal MC.

The numbers of fake events in the background control regions ($i$ = B, C, D) are written as

$$N_i^{fake} = N_i^{data} - c_i N_A^{sig} - N_i^{bkg}, \tag{5.4}$$

making the final signal region breakdown:

$$N_A^{data} = N_A^{sig} + R\frac{(N_B^{data} - c_B N_A^{sig} - N_B^{bkg})(N_C^{data} - c_C N_A^{sig} - N_C^{bkg})}{N_D^{data} - c_D N_A^{sig} - N_D^{bkg}} + N_A^{bkg}. \tag{5.5}$$

This equation can then be solved for $N_A^{sig}$. It is solved inclusively and in each bin of the differential measurements.

Three sources of systematic uncertainty are considered for the 2D-sideband method. The statistical uncertainties on the numbers of data events ($N_i^{data}$) and prompt photon backgrounds ($N_i^{bkg}$) are propagated through to the value of $N_A^{sig}$. A systematic uncertainty on the signal leakage factors is derived to account for imperfect modelling of the photon isolation and identification variables. This is done by varying the pile-up reweighting factors in the signal MC by an amount which covers the uncertainty on the ratio of the measured and predicted inelastic proton-proton cross-section [93]. The final source of systematic uncertainty considered is due to the correlation factor $R$, which is described above.

### 5.2.2 $t\bar{t}\gamma$ background

As mentioned in Section 4.3.3, an opposite-sign different-flavour control region ($e\mu\gamma$) is used to constrain the normalisation of the top background. Other processes are accounted for in this region, such as the fake photon background which is estimated using the same technique as described in the previous section. Contributions to this

CR from $\tau\tau\gamma$, $WZ\gamma$ and $WW\gamma$ are also considered. The detector-level yields as a function of $E_T^\gamma$ and $m_{\ell\ell\gamma}$ are shown in Figure 5.1.

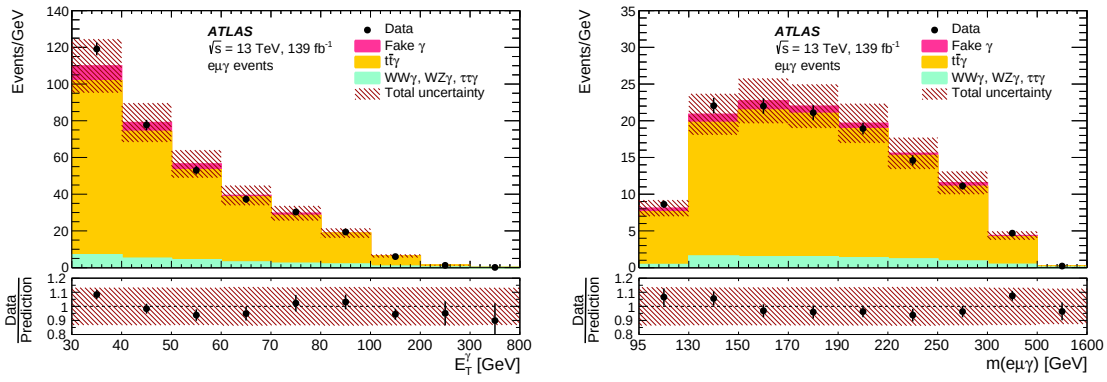


(a) (b)

Figure 5.1: The detector-level yields as a function of (a) $E_T^\gamma$ and (b) $m_{\ell\ell\gamma}$ in the $e\mu\gamma$ control region [26]. The $t\bar{t}\gamma$ contribution is multiplied by a k-factor of 1.44.

After subtracting the backgrounds from the data in this region, a normalisation factor for the $t\bar{t}\gamma$ MC is found to be 1.44. The normalisation factor is shown to provide good agreement between prediction and data in the $e\mu\gamma$ CR, across the whole range used for the differential measurements. An uncertainty of 15% is placed on the normalisation factor which is determined from an independent $t\bar{t}\gamma$ measurement [94]. This uncertainty comfortably covers the data-simulation disagreement in all bins, as demonstrated in Figure 5.1. The normalisation factor is subsequently applied to the $t\bar{t}\gamma$ MC in the signal region.

### 5.2.3 Pile-up background

The rate at which a $Z$+jets event overlaps with a $\gamma$+jets event from a different vertex in the same bunch crossing is estimated using a data-driven technique. The technique uses the variable $\Delta z = z_\gamma - z_{PV}$ which is the difference in the position along the beam line of the primary vertex and the extrapolated position of the photon. Typically, $z_\gamma$ is not reconstructed well enough to match it to a particular vertex, given a resolution of about 20 mm using directional information from the

calorimeter only. However, for photons which convert, additional information from the tracking systems is used to provide a much better resolution for the photon production vertex. Furthermore, converted photons which have a conversion vertex within the pixel detector ($R_{conv} < 125$ mm) have the best possible resolution of around 0.2 mm. These so-called pixel conversions are used to calculate the rate at which a photon is selected which originates from a different vertex to the $Z$. This rate is then extrapolated to the whole data sample including all photon types.

In Figure 5.2, the $\Delta z$ distribution in the ISR signal region in data is compared to the FSR control region, where the FSR cut is inverted, for photons which convert within the pixel volume. In the FSR case, the photons are naturally constrained to come from the same vertex as the leptons due to the invariant mass requirement of $m_{\ell\ell} + m_{\ell\ell\gamma} < 2m_Z$. Therefore, the events in the tails of the $\Delta z$ distribution for FSR events are primarily due to the resolution associated with the reconstruction of the converted photons. Contributions from pile-up background are assumed to be negligible in the FSR region due to the implicit vertex constraint. As well-reconstructed pixel conversions are used, the $\Delta z$ distribution should be similar regardless of whether the photon is ISR or FSR. However this is not what is seen in Figure 5.2 as there is an excess in the tails for the ISR (SR) events, which comes from events where the photon originates from a separate $pp$ interaction.

The $\Delta z$ distribution in ISR data is formed of two components. The first comes from single $pp$ interactions, which is narrowly peaked around $\Delta z = 0$. This includes both the signal and background processes in which the lepton and photon objects originate from the same vertex. The second, much wider, component comes from the pile-up background where the photon vertex is different to the PV. The width of this distribution can be calculated by considering the width of the PV $z$ position in data. This is found to be described by a Gaussian of width 35 mm. Therefore the shape of the pile-up component to the $\Delta z$ distribution is formed by the convolution of two such distributions, giving a total width of 50 mm. The ISR distribution shown in Figure 5.2 is formed from the sum of these two components.

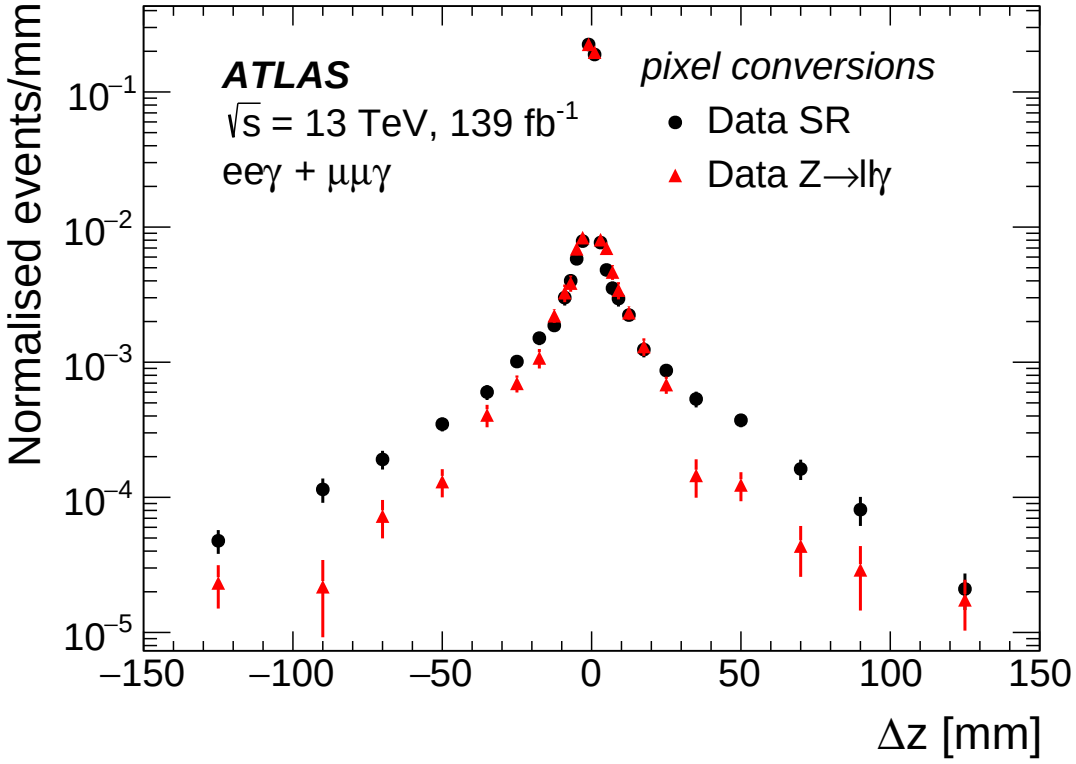


Figure 5.2: Comparison of the $\Delta z$ distributions of SR (ISR) and $Z \to \ell\ell\gamma$ (FSR) photons in data for photons which convert within the volume of the pixel detector [26].

The pile-up background fraction is measured in the tails ($|\Delta z| > 50$ mm) of the ISR $\Delta z$ distribution, where the dominant process is the pile-up background, and this is hence less reliant on the modelling of the single-$pp$ processes. The narrow component of the $\Delta z$ distribution is modelled by the Sherpa $\ell\ell\gamma$ MC signal sample. This distribution is normalised to the data around $\Delta z = 0$ which means it accounts for all single-$pp$ processes, not just the signal. This normalisation factor is found to be 1.4±0.1, where the uncertainty is driven by the number of data events.

An additional normalisation factor is derived which accounts for potential mismodelling in the tails of the $|\Delta z|$ distribution. This is done by investigating the fraction of events which are in the tails, in both data and the signal MC. FSR events are used so that the data is only sensitive to resolution effects and does not include the pile-up background. The fraction is found to be higher in data so a normalisation factor of 1.5±0.3 is derived as the ratio of the fraction in data to the fraction in the

signal MC. The uncertainty is statistical and is mainly driven by the limited data events in the tail region. The two normalisation factors are combined resulting in a total normalisation factor of $F = 2.1 \pm 0.4$, which is applied to the signal MC in the tail region.

The fraction of pile-up background is calculated by first subtracting the normalised signal MC from the data in the tails of the ISR $\Delta z$ distribution. As the tails correspond to $> 1\sigma$ of the two-sided Gaussian pile-up background distribution, a factor of $1/0.32$ can be used to extrapolate to the full range of $\Delta z$. This number is then divided by the total number of pixel conversion events, to get the fraction of events which have a pile-up photon ($f_{PU}$), which can be applied to the full signal region data. This is summarised by the following equation:

$$f_{PU} = \frac{N^{|\Delta z|>50mm}_{data,pixel-conv} - F \times N^{|\Delta z|>50mm}_{signalMC,pixel-conv}}{N_{data,pixel-conv} \times 0.32}, \tag{5.6}$$

from which $f_{PU}$ is determined to be $4.6 \pm 0.6\%$. Both the statistical uncertainties on the numbers of events in the above equation, and the uncertainty on $F$ are propagated to the uncertainty on $f_{PU}$.

The fraction of data which is determined to have a pile-up photon also contains events which have a pile-up jet faking a photon. However such events are already accounted for in the 2D-sideband method. So an additional purity factor is derived which separates the pile-up photon from the pile-up jet-faking-photon events. This is estimated using the same 2D-sideband method on single photon data. The purity is found to be $54 \pm 7\%$, resulting in a final pile-up photon fraction ($f^{\gamma}_{PU}$) of $2.5 \pm 0.5\%$.

The distributions of the number of events for this background, needed for the differential measurements, are determined from overlaid MC events at truth level. A dilepton pair is taken from a $Z$+jets sample, and overlaid with a random photon taken from a $\gamma$+jets event. The events are overlaid at truth level so the fiducial selection is applied to the combined objects. The distributions of the events which pass the fiducial selection are transformed to the detector level using bin-by-bin

factors similar to those defined in the unfolding (Section 4.4.1), in each channel. The distributions are then normalised to $f_{PU}^{\gamma}$ times the signal region yield in each channel.

### 5.2.4 Other backgrounds

Other smaller backgrounds are estimated directly from simulation. The processes considered include $Z(\rightarrow \tau\tau)\gamma$ and $WW\gamma$ which produce an irreducible contribution to the signal final states but have much lower cross-sections than the signal processes. The $WZ \rightarrow \ell\ell\ell\nu$ and $ZZ \rightarrow \ell\ell\ell\ell$ processes are also considered where an electron may fake a photon. The contribution from these processes are much smaller than that from jets faking photons, so any mismodelling effects have a much less significant effect on the results. Therefore the electron faking photon contributions are taken directly from simulation. In total, these four processes contribute less than 1% of the total data yield in the signal region.

### 5.2.5 Detector-level distributions

To examine the validity of the predictions, the sum of the background predictions and signal MC are compared to data at the detector level. The distributions in each channel are shown in Figure 5.3 as a function of $E_T^{\gamma}$ and $m_{\ell\ell\gamma}$. In these figures, the signal MC is scaled by a factor of 1.23, which is derived from the ratio between the background-subtracted data and raw signal MC yields. The need for this k-factor could arise from missing higher-order corrections, not included in the LO signal sample. A good agreement is seen between data and prediction, with all bins agreeing within uncertainty.

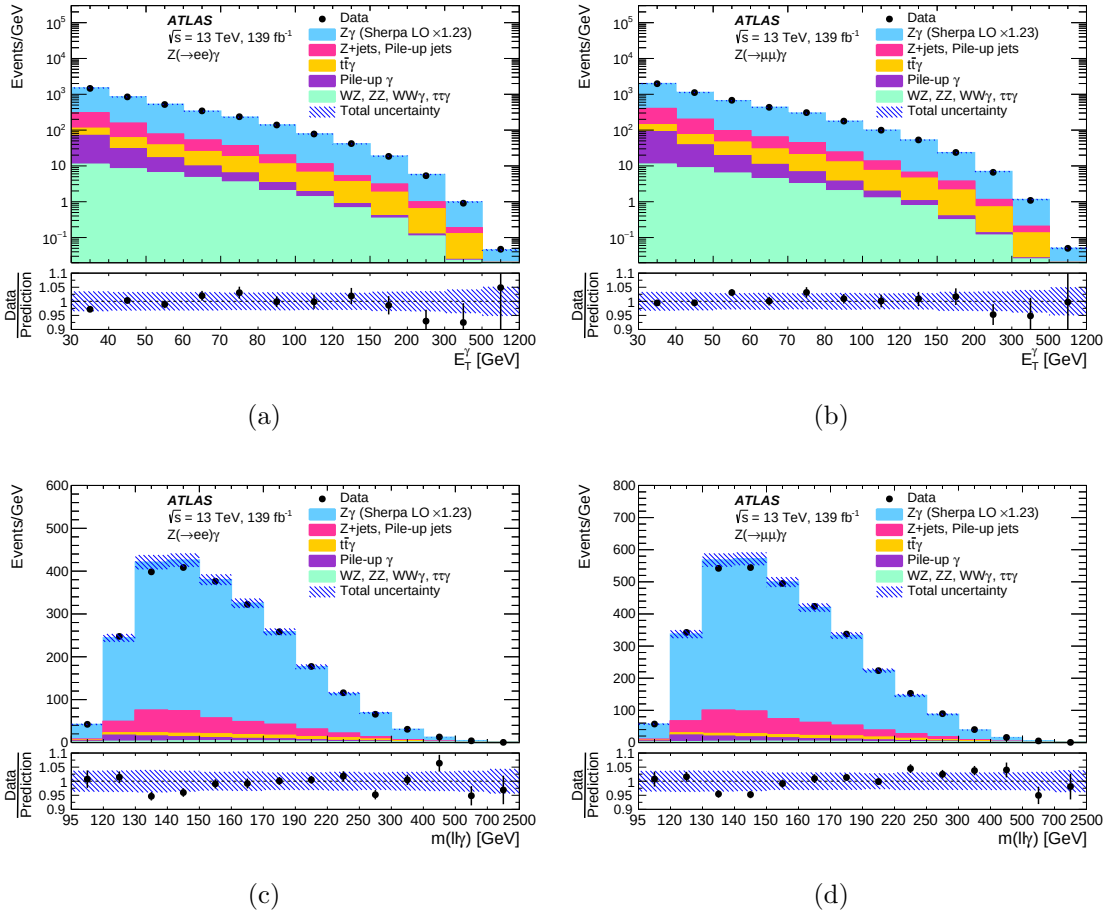


Figure 5.3: The detector-level data are compared to the sum of the background predictions and normalised signal MC, as a function of $E_T^\gamma$ and $m_{\ell\ell\gamma}$ in the $ee\gamma$ and $\mu\mu\gamma$ channels [26].

## 5.3 Photon isolation

Photon isolation plays an important role in many aspects of the analysis. At the detector level, the photon isolation cut is used to suppress fake photons. A photon isolation cut is also defined in the fiducial phase space in order to minimise the extrapolation from the detector-level phase space. Finally, in the generation of MC events and fixed-order calculations, an isolation cut is used to remove contributions from collinear fragmentation photons. The interplay of these three cuts must be carefully considered to avoid biases resulting from the different phase spaces used, or from the choice of model. The following sections describe the photon isolation at the detector, fiducial and generator level and their impact on the results.

### 5.3.1 Detector-level isolation

The detector-level photon isolation cut is chosen to reject contributions from the fake photon background, whilst retaining as much of the signal as possible. Two working points exist; the first *FixedCutLoose* is ultimately chosen and is defined in Section 4.2.4.2. The second, *FixedCutTight*, is calculated in a cone size of $\Delta R < 0.4$ around the photon, whereas *FixedCutLoose* is calculated in a cone size of $\Delta R < 0.2$. The signal efficiency of both cuts is shown in Figure 5.4(a), along with the separate track and calorimeter efficiencies for *FixedCutLoose*. *FixedCutTight* is not used as the signal efficiency is too poor, particularly at high pile-up and it has been shown that the fake photons are well estimated using the *FixedCutLoose* working point (Section 5.2.5).

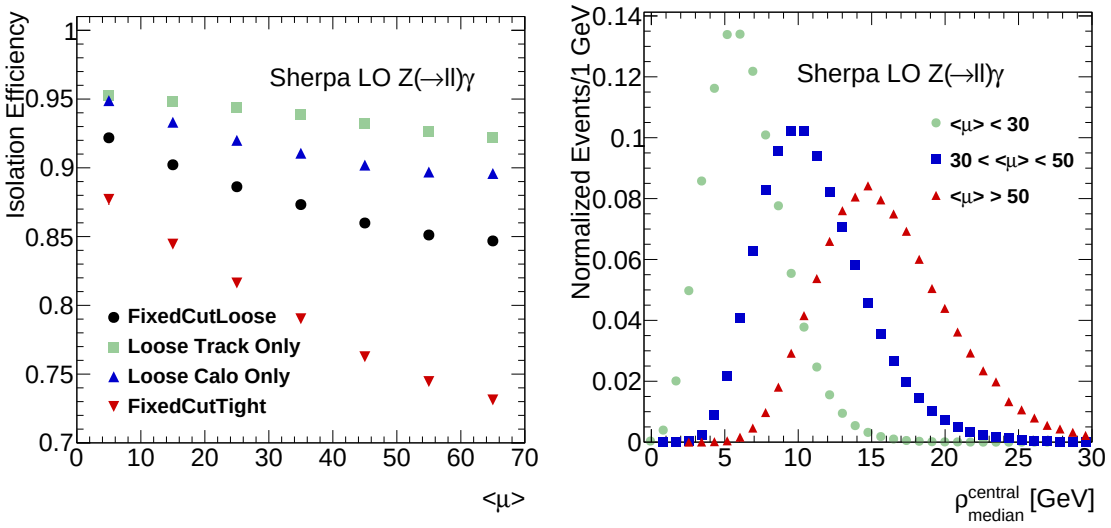


(a) (b)

Figure 5.4: (a) The photon isolation efficiency as a function of pile-up for various isolation working points. (b) The median energy density in the central region of the detector ($|\eta| < 1.5$) as a function of pile-up.

It is seen that in all cases there is a degradation of the efficiency with increasing pile-up. This is less pronounced in the track isolation efficiency due to the fact that the tracks must be associated to the primary vertex in order to be included in the calculation of $p_T^{cone20}$, and hence is less influenced by pile-up. The calorimeter isolation is more strongly influenced as no such association can be made for the

calorimeter clusters. Instead, an $\eta$-dependent correction is applied to $E_T^{cone20}$ in order to account for the contribution from pile-up clusters.

$E_T^{cone20}$ is calculated as

$$E_T^{cone20} = E_{T,raw}^{cone20} - E_T^{5\times 7 core} - E_T^{leakage}(p_T) - E_T^{pile\text{-}up}(\eta), \tag{5.7}$$

where $E_{T,raw}^{cone20}$ is the total $E_T$ measurement from clusters within $\Delta R < 0.2$ of the photon, $E_T^{5\times 7 core}$ is the estimation of the contribution from the photon itself calculated in a 5×7 ($\eta \times \phi$) window around the photon, and $E_T^{leakage}(p_T)$ is a MC-driven correction for the amount of photon energy which leaks outside the 5×7 window, determined as a function of photon $p_{\mathrm{T}}$. $E_T^{pile\text{-}up}(\eta)$ is the correction for pile-up which is calculated as

$$E_T^{pile\text{-}up} = \rho(\pi R^2 - A_{core}), \tag{5.8}$$

where $\rho$ is the median energy density for all reconstructed clusters with $E_T > 1$ GeV in an event, $R$ is the radius of the cone, and $A_{core}$ is the area of the 5×7 window. $\rho$ is calculated separately in the central ($|\eta| < 1.5$) and forward ($|\eta| > 1.5$) regions on a per-event basis. Figure 5.4(b) shows $\rho$ in the central region in three different ranges of pile-up. As expected, the mean value in each of the three regions increases with pile-up, however the width of the distributions also increases due to larger event-by-event fluctuations. This means there is a higher chance that the pile-up subtraction is underestimated and the photon fails the isolation cut at higher pile-up.

### 5.3.2 Truth-level isolation

A photon isolation cut is defined at the truth level in order to reduce the extrapolation between the detector-level and truth-level phase spaces during the unfolding, thus reducing the dependence on the choice of model for the signal MC. The truth-level photon isolation parameter, $E_T^{cone20}$, is defined as the sum of the $E_T$ of all truth-level particles which fall in a cone of $\Delta R < 0.2$ around the photon, excluding muons, neutrinos and the photon itself. This therefore includes all particles which

would be detected in the tracking and calorimeter systems. The truth isolation cut is also required to scale with the photon $p_{\mathrm{T}}$, as is done at the detector level, so the cut is defined as a value of $E_T^{cone20}/E_T^{\gamma}$.

The performance of the truth-level isolation cut should match that of the detector-level cut, meaning that an event has approximately the same chance of passing (or failing) both cuts. The truth-level cut value is determined by looking at the ratio of the number of events which pass the detector-level isolation cut to those which fail it, as a function of the truth-level isolation variable $E_T^{cone20}/E_T^{\gamma}$. This is shown in Figure 5.5, where it is seen that the point at which the ratio is equal to 1, corresponds to a cut of 7%. It is also crucial that the distribution is not steeply falling in this region so that the performance is not sensitive to small changes in the cut value, which is what is seen in the figure. The value of 7% is similar to the 6.5% which is used at detector level, but differences are caused by detector resolution and the fact that the truth-level cut is replicating both the track and calorimeter based isolation cuts at detector level.

### 5.3.3 Generator-level isolation

The modelling of prompt photon production from hadron collisions is complicated due to the existence of two production mechanisms. The first, known as direct production, is simply the radiation of a photon off an incoming quark (e.g. Figures 1.5(a) and 1.8(a)). These processes are characterised by a large energy scale and hence can be calculated using perturbative QCD. In the second production mechanism, a photon can be radiated during the fragmentation of an outgoing parton. The emission of such a photon may be collinear to the parton which can lead to infrared divergences in the cross-section as the photon can be emitted with arbitrarily small momentum. Such photons are referred to as fragmentation photons and an example is shown in Figure 5.6 for the quark-gluon production of $Z\gamma$. As this production method is non-perturbative, the contribution must be estimated by using fragmentation functions, which are derived from fits to data, in a similar way

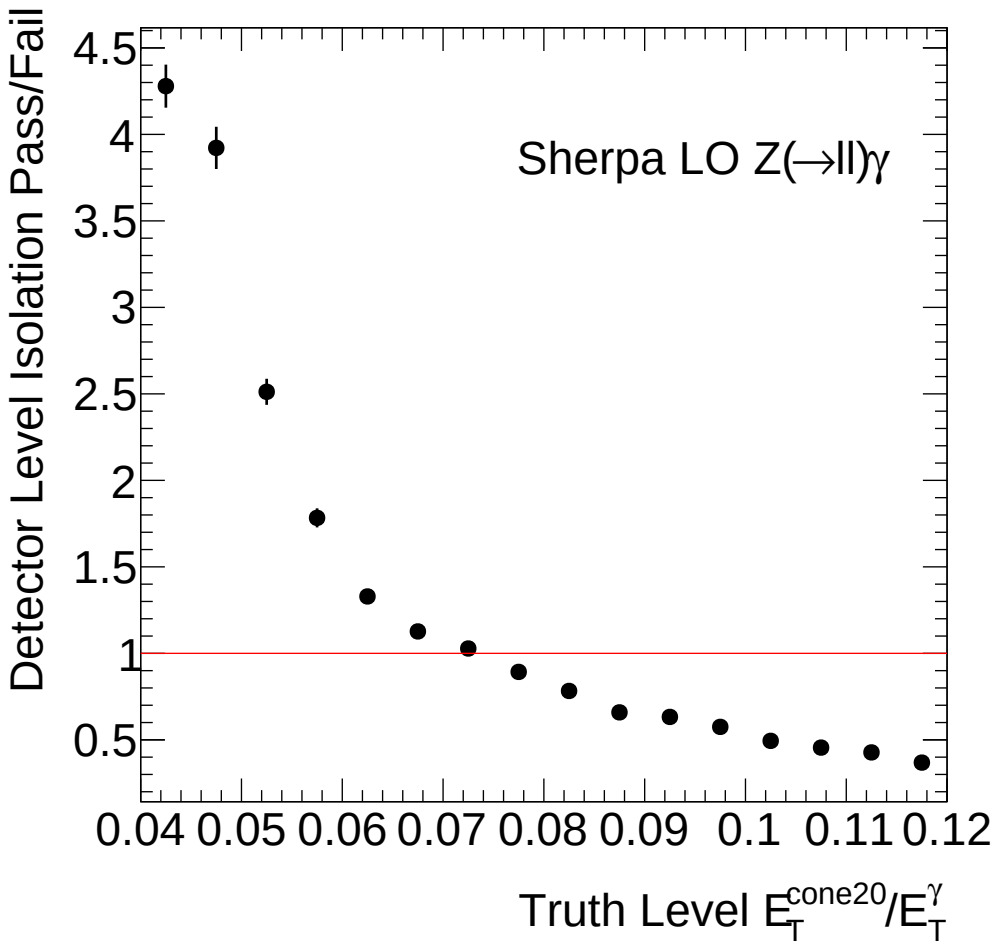


Figure 5.5: The ratio of the number of events which pass the detector level isolation cut to the number which fail it, as a function of the truth-level isolation variable. The red line corresponds to the point where the ratio is equal to one.

to parton density functions (Section 1.3). Fragmentation photons are typically not well isolated as partonic remnants remain close to the photon. This results in a large proportion of fragmentation photons being removed by isolation cuts in the detector-level selection. However the remaining contribution must still be estimated by the data-driven fragmentation functions.

An alternative approach is to remove the contribution of fragmentation photons altogether. This is done by implementing a smooth cone isolation [95] (Frixione isolation) during the calculation of predictions. The requirement considers the angular separations between partons and the photon, which is demonstrated in Figure 5.7.

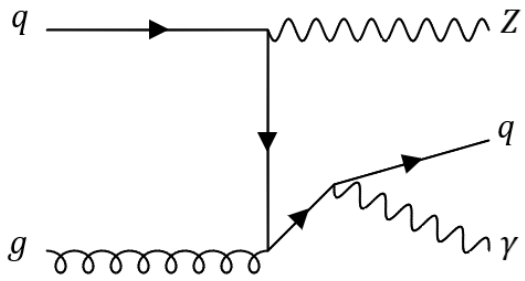


Figure 5.6: An example of $Z\gamma$ production where the photon is radiated via parton fragmentation. Collinear divergences arise when the angle between the photon and the fragmented parton is small.

For each outgoing parton ($p_i$) which falls within a predefined cone of size $\delta_0$ around the photon, a sub-cone is defined by the angular separation between that parton and the photon ($\delta_i$). The isolation requirement is imposed in each sub-cone by requiring that the sum of the transverse momentum of all partons within the sub-cone, including that which defines the sub-cone, is less than a predefined fraction of the transverse momentum of the photon ($\epsilon p_T^\gamma$), multiplied by the function

$$\left(\frac{1-cos(\delta_i)}{1-cos(\delta_0)}\right)^n. \tag{5.9}$$

This function ensures that the requirement gets tighter as the sub-cone gets smaller, and this scaling can be adjusted using the third predefined parameter, $n$. This therefore ensures the removal of events with photons produced by collinear radiation, as the partons considered are very close to the photon.

The three adjustable parameters $\delta_0$, $\epsilon$ and $n$ are chosen so as not to be tighter than the photon isolation cuts applied in the detector-level selection (Sections 5.1 and 6.1), otherwise areas of the detector-level phase-space would be excluded during the generation of MC events. The detector-level isolation requires that the measured energy or momentum within a cone around the photon must be less than some fraction of the photon transverse momentum. This means that in the definition of the Frixione isolation used to produce the predictions, $\delta_0$ must not be larger than the cone size used in the detector-level isolation and $\epsilon$ must be larger than the photon momentum fraction used in the detector-level isolation.

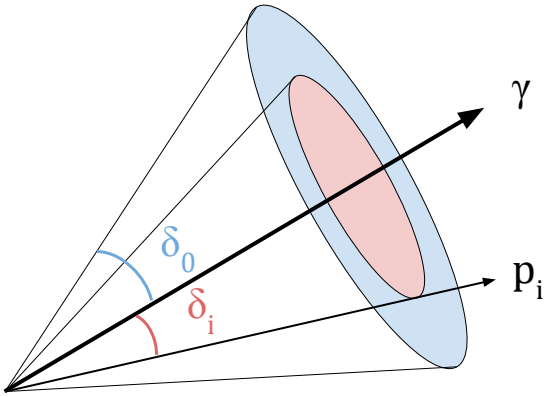


Figure 5.7: A diagram showing the angular separations considered in the Frixione isolation requirement. The angular separation between parton $p_i$ and the photon ($\gamma$) is given as $\delta_i$ and all partons with $\delta_i < \delta_0$ are considered.

An important caveat related to Frixione isolation comes when considering the interplay with the truth-level isolation. To explore the effect of Frixione isolation on the truth-level phase space, signal samples are generated with Sherpa 2.2.4 with various sets of Frixione parameters. The MC predictions are considered here because variables can be studied at both the parton and truth levels for the same sample. The predicted fiducial cross-section is shown for two $p_T^\gamma$ slices in the $ee\gamma$ channel in Figure 5.8, for five different sets of Frixione parameters. It is seen that the fiducial cross-section is sensitive to the choice of parameters, with the tighter values for the variables (larger $\delta_0$, smaller $\epsilon$) generally predicting a smaller cross-section, which is the expected behaviour. It is therefore necessary to quote predicted cross-sections corresponding to a particular set of Frixione parameters. It is also necessary to quote measured cross-sections corresponding to a particular set of parameters as the truth-level isolation also influences the unfolding.

Another complication arises when considering the fixed-order calculations, which are produced at the parton level. An extrapolation needs to be performed in order to compare these to unfolded data or other fiducial-level predictions. The extrapolation is linked to photon isolation due to the two different implementations at the parton and truth levels. A correction factor can be derived which is simply the truth-level photon isolation efficiency, which is then applied to the parton-level predictions.

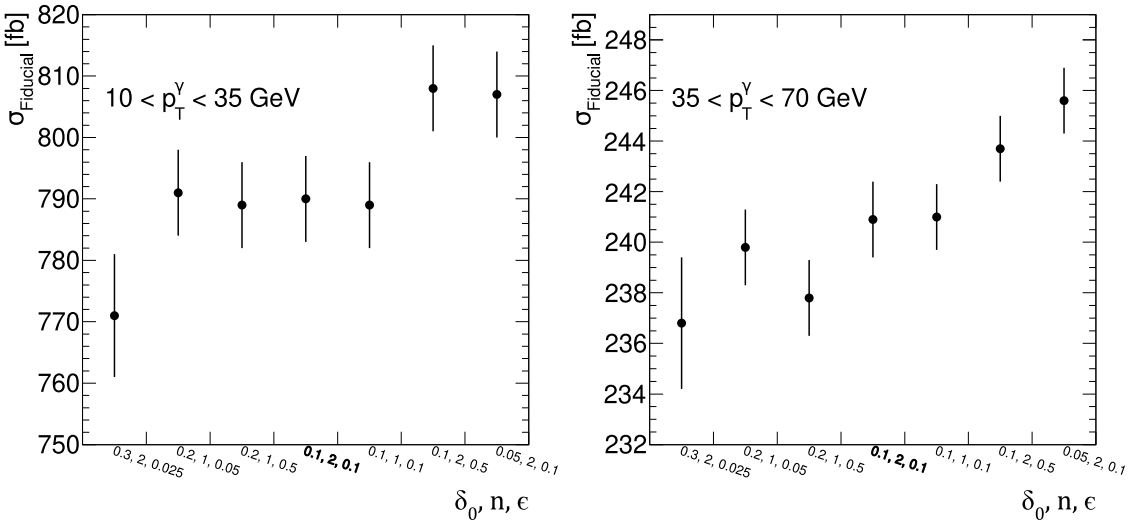


(a) (b)

Figure 5.8: The fiducial $Z\gamma$ cross-section for various sets of Frixione isolation parameters in two slices of photon $p_{\mathrm{T}}$ in the $ee\gamma$ channel: (a) $10 < p_T^{\gamma} < 35$ GeV and (b) $35 < p_T^{\gamma} < 70$ GeV. The bin labelled with the bold font corresponds to the parameters used in the final analysis.

This correction factor is shown for the MC samples generated with different Frixione parameters in Figure 5.9. Again, there is a clear dependence on the Frixione parameters for the isolation efficiency, particularly on $\delta_0$. For a fair extrapolation, it is therefore crucial that a common set of Frixione parameters is used between the fixed-order calculations and MC samples, from which the corrections are derived.

To conclude, the implementation of a Frixione photon isolation requirement in the generation of MC events and fixed-order calculations avoids the estimation of the non-perturbative fragmentation component. However, the parameters must be chosen carefully in order to make a coherent comparison between measurement and prediction. Firstly, the parameters must not be tighter than those applied in the detector and truth level isolation selections, so that regions of phase space are not removed at the generator level. Secondly, a common set of parameters must be used across all predictions to provide a fair comparison among them. Finally, it is seen that the fiducial cross-section is dependent on the choice of Frixione parameters, so measured and predicted cross-sections must be quoted corresponding to a particular set of parameters. For the $Z\gamma$ analysis, all MC samples and fixed-order calculations

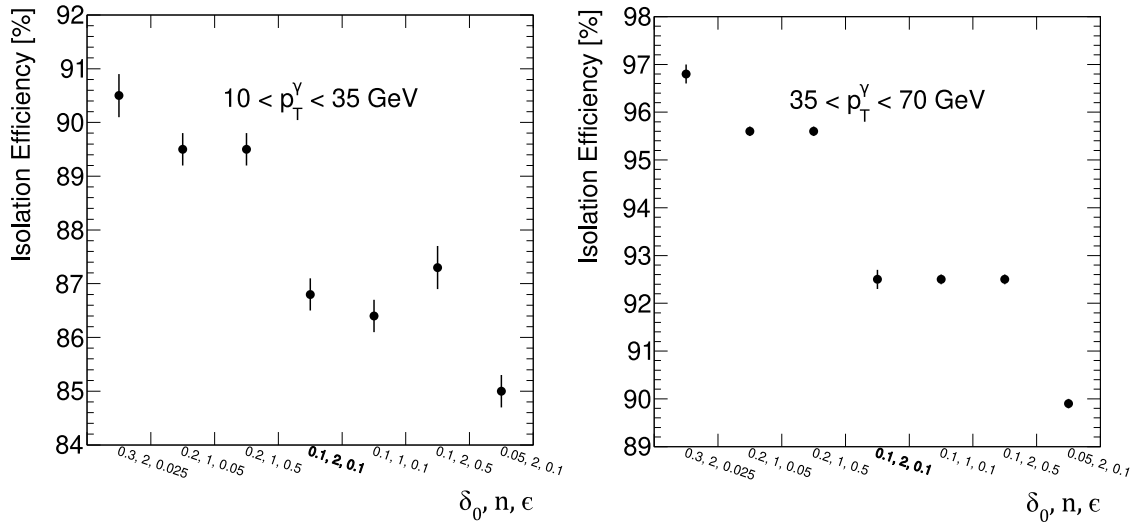


(a) (b)

Figure 5.9: The photon fiducial isolation efficiency for various sets of Frixione isolation parameters in two slices of photon $p_{\mathrm{T}}$ in the $ee\gamma$ channel, (a) $10 < p_T^\gamma < 35$ GeV and (b) $35 < p_T^\gamma < 70$ GeV. The bin labelled with the bold font corresponds to the parameters used in the final analysis.

are generated with the Frixione parameters $\delta_0$=0.1, $\epsilon$=0.1 and $n$=2.

## 5.4 Results

The background prediction is subtracted from the total data yield in each channel, then divided by the corresponding $C$-factor as shown in Equation 4.1. The fiducial signal yield is then divided by the integrated luminosity in order to calculate the integrated fiducial cross-section. The systematic uncertainties, listed in Section 4.4.2, are propagated through to this cross-section value. The relative sizes of the uncertainties in each channel are listed in Table 5.1. The dominant sources of uncertainty come from the electron identification efficiency correction, the fake photon background estimate and the uncertainty on the integrated luminosity.

The fiducial cross-section values in each channel are combined following the procedure described in Section 4.4.2.1. The integrated fiducial $Z(\to \ell\ell)\gamma$ cross-section is

| Source | Relative uncertainty [%] | |
|---|---|---|
| | $e^+e^-\gamma$ | $\mu^+\mu^-\gamma$ |
| Trigger efficiency | - | 0.2 |
| Photon identification efficiency* | 1.0 | |
| Photon isolation efficiency* | 0.9 | |
| Electron identification efficiency | 1.4 | - |
| Electron reconstruction efficiency | 0.3 | - |
| Electron-photon energy scale* | 0.9 | 0.6 |
| Muon isolation efficiency | - | 0.4 |
| Muon identification efficiency | - | 0.7 |
| $Z$+jets background* | 1.3 | |
| Pile-up background* | 0.6 | |
| Other backgrounds* | 0.8 | 0.7 |
| Monte Carlo event statistics | 0.4 | 0.4 |
| Integrated luminosity* | 1.7 | |
| Systematic uncertainty | 3.2 | 2.9 |
| Statistical uncertainty | 0.6 | 0.5 |
| Total uncertainty | 3.2 | 3.0 |

Table 5.1: Relative systematic uncertainties on the integrated $Z(\to \ell\ell)\gamma$ fiducial cross-section in each channel [26]. Uncertainties marked with a * are fully or partially correlated between the two channels.

measured to be

$$\sigma_{fid}^{Z(\to\ell\ell)\gamma} = 533.7 \pm 2.1(\text{stat}) \pm 12.4(\text{syst}) \pm 9.1(\text{lumi}) \text{ fb}\,.$$

The measured cross-section is compared to the theory predictions from MATRIX at NLO and NNLO in QCD (first introduced in Section 1.6.2). As mentioned in the previous section, these predictions are provided at parton level so the correction factor to account for the difference between parton and truth-level isolation is applied. Inclusively this factor is 0.9338±0.0004. An additional correction factor is derived which accounts for the dressing procedure. This correction factor is calculated as the ratio of the fiducial cross-section using dressed leptons to that when using raw leptons, where the energy of nearby photons is not added to the leptons. Inclusively this factor is 0.9800±0.0003. The overall correction is a product of both factors and is also calculated in each bin of the differential measurements.

The integrated fiducial cross-section measurement is displayed in Figure 5.10 where it is compared to the corrected predictions from MATRIX. The NNLO QCD prediction is also shown when including the NLO EW corrections applied additively and multiplicatively. The total uncertainty on the measured cross-section is 3%. At this level of precision, the importance of the NNLO terms in the cross-section calculation is highlighted as the agreement between the measurement and the NLO cross-section is poor. The agreement with the NNLO cross-section is good, and the NLO EW corrections only have a small effect on the integrated cross-section. The prediction from MATRIX at NNLO agrees with the measured integrated cross-section within $0.7\sigma$.

The data are unfolded and differential fiducial cross-sections are measured as functions of the transverse momentum of the photon ($E_T^\gamma$), the pseudorapidity of the photon ($|\eta^\gamma|$), the invariant mass of the 3-body system ($m_{\ell\ell\gamma}$), the transverse momentum of the 3-body system ($p_T^{\ell\ell\gamma}$), the ratio of these two variables ($p_T^{\ell\ell\gamma}/m_{\ell\ell\gamma}$) and the azimuthal separation between the dilepton system and the photon ($\Delta\phi(\ell\ell,\gamma)$). In Figures 5.11 and 5.12, a number of these distributions are compared to the predictions from MATRIX. The NLO EW corrections to the NNLO prediction from MATRIX are only available for the $E_T^\gamma$, $|\eta^\gamma|$ and $m_{\ell\ell\gamma}$ distributions. In Figure 5.13, the measured distributions are compared to predictions from the Sherpa and MadGraph MC generators. The full set of results, where the data are compared to MATRIX and the MC generators for all six observables, can be found in Reference [26].

The $E_T^\gamma$ distribution represents a basic experimental property of the photon. The $E_T^\gamma$ distribution is compared to MATRIX in Figure 5.11(a) where it is seen that the prediction at NLO is once again poor, but the inclusion of the NNLO QCD corrections result in a much better agreement with data. The effects of the NLO EW corrections are also most pronounced in the highest bins of this distribution, where the corrections are of similar size to the difference between the NLO and NNLO QCD corrections. The $E_T^\gamma$ distribution is also compared to the predictions from MC generators in Figure 5.13(a). The Sherpa LO prediction provides a reasonable description of the shape, but the normalisation is underestimated by about 20%.

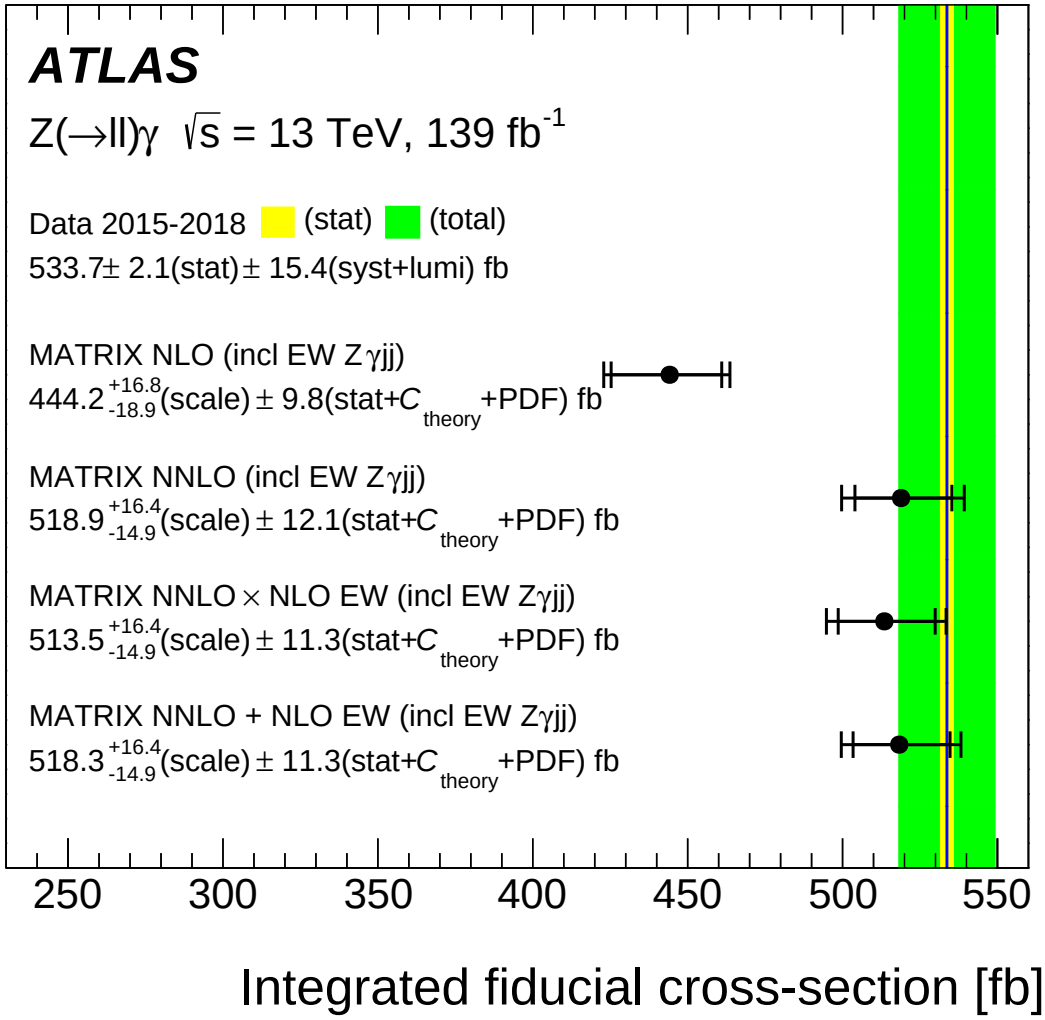


Figure 5.10: The measured integrated fiducial $Z(\to \ell\ell)\gamma$ cross-section compared to predictions from MATRIX [26].

The NLO predictions from Sherpa and MadGraph provide a better description of the normalisation but still have shape differences of up to 15%.

The $m_{\ell\ell\gamma}$ distribution provides a measure of the hard scale of the process, which is measured up to 3 TeV. As is seen in Figure 5.11(b), the NNLO prediction provides a poor description of this distribution in the low and high mass regions. However, it is seen that the inclusion of the NLO EW corrections improves the agreement greatly in these regions.

The $p_T^{\ell\ell\gamma}$, $p_T^{\ell\ell\gamma}/m_{\ell\ell\gamma}$ and $\Delta\phi(\ell\ell,\gamma)$ distributions all provide probes of the QCD mod-

elling of the predictions. It is therefore expected that lower-order predictions will provide significantly worse modelling of these variables. The $p_T^{\ell\ell\gamma}$ distribution is compared to predictions from MC generators in Figure 5.13(b). The Sherpa LO prediction provides a poor description of the shape and normalisation, but the description is better for the NLO predictions. The $p_T^{\ell\ell\gamma}/m_{\ell\ell\gamma}$ distribution is compared to the predictions from MATRIX in Figure 5.12(a). The NLO prediction is very poor with differences up to 50% in some bins, but the inclusion of the NNLO corrections results in a much better description. The $\Delta\phi(\ell\ell,\gamma)$ distribution is shown in Figure 5.12(b). It is seen that the majority of events are produced with the $Z$ and photon pointing in roughly opposite directions, as would be expected in the LO case. The region below the peak is hence sensitive to higher-order QCD corrections. This region is much better described by the NNLO prediction, as expected.

### 5.4.1 Summary and outlook

The $Z(\to \ell\ell)\gamma + X$ process is measured in isolation for the first time, at a centre-of-mass energy of 13 TeV. The integrated fiducial cross-section is measured to a precision of 3%, which is an improvement of almost a factor two compared to the 8 TeV $\ell\ell\gamma$ measurement [41]. This is primarily due to the approximately four times larger dataset, but also improvements in the systematic uncertainties. The fiducial cross-section is also measured differentially as functions of six variables which are used to test QCD modelling up to NNLO and also the inclusion of EW corrections at NLO.

Further analysis of the $Z\gamma$ process at 13 TeV could be used to probe anomalous couplings. The limits set would be expected to be more stringent than previous studies of this process due to the higher precision, higher centre-of-mass energy and the ISR phase space selection. Additionally, this process could be used to further test QCD modelling by measuring the cross-section as a function of the number of jets in the event, and also the exclusive cross-section by requiring a jet veto.

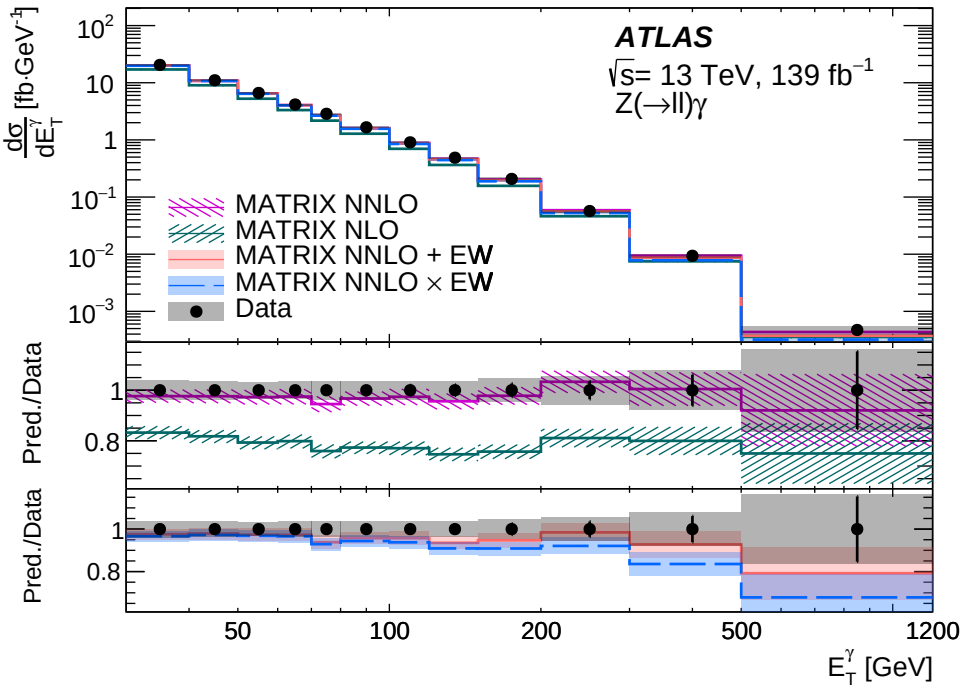


(a)

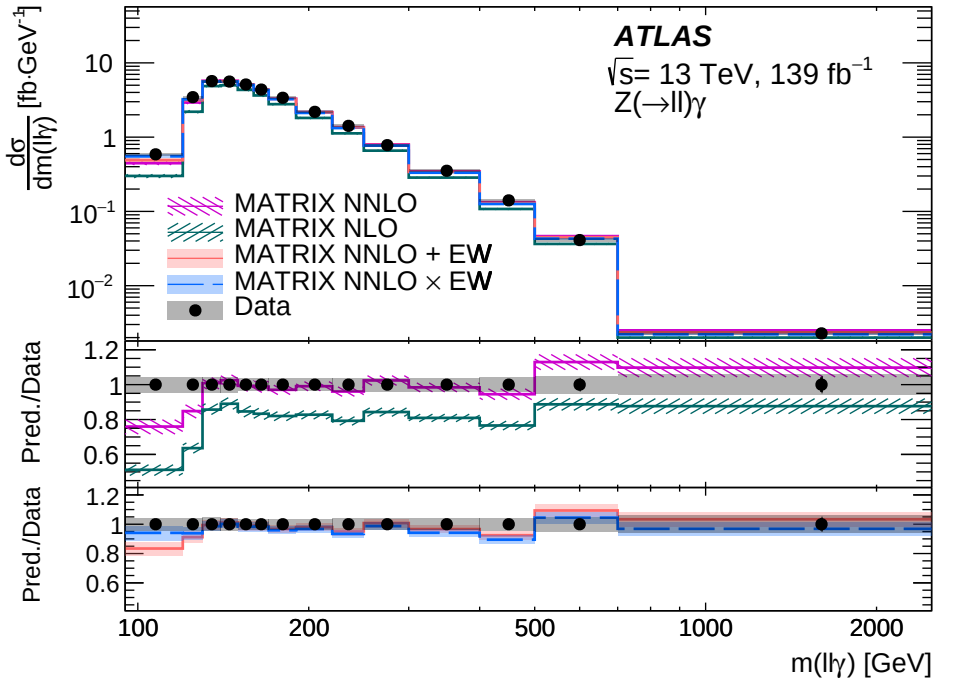


(b)

Figure 5.11: The differential fiducial cross-section measurements as a function of (a) the photon transverse energy and (b) the three-body invariant mass, compared to predictions from MATRIX [26].

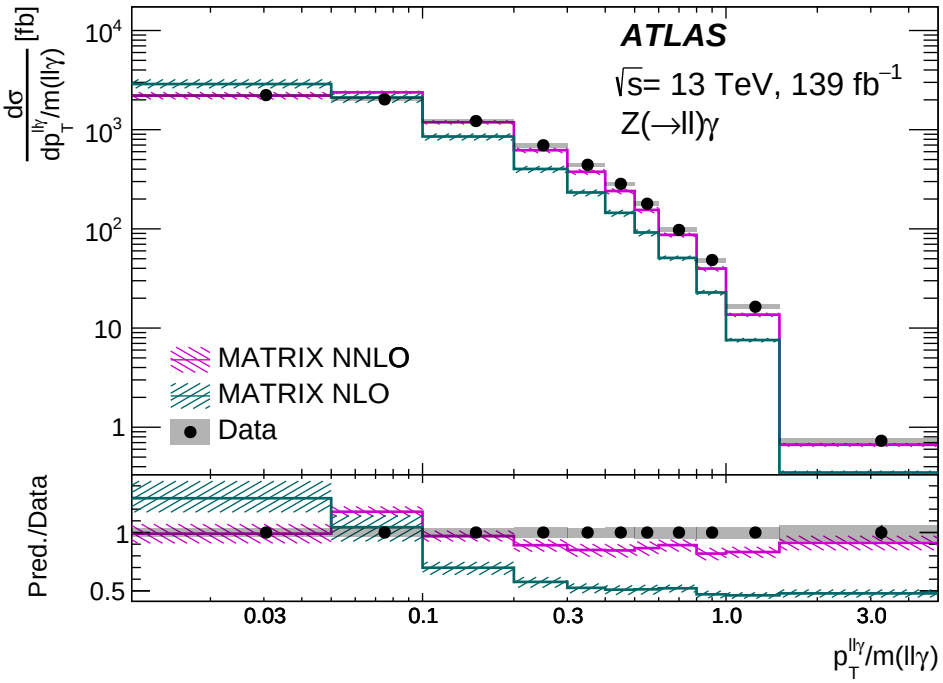


(a)

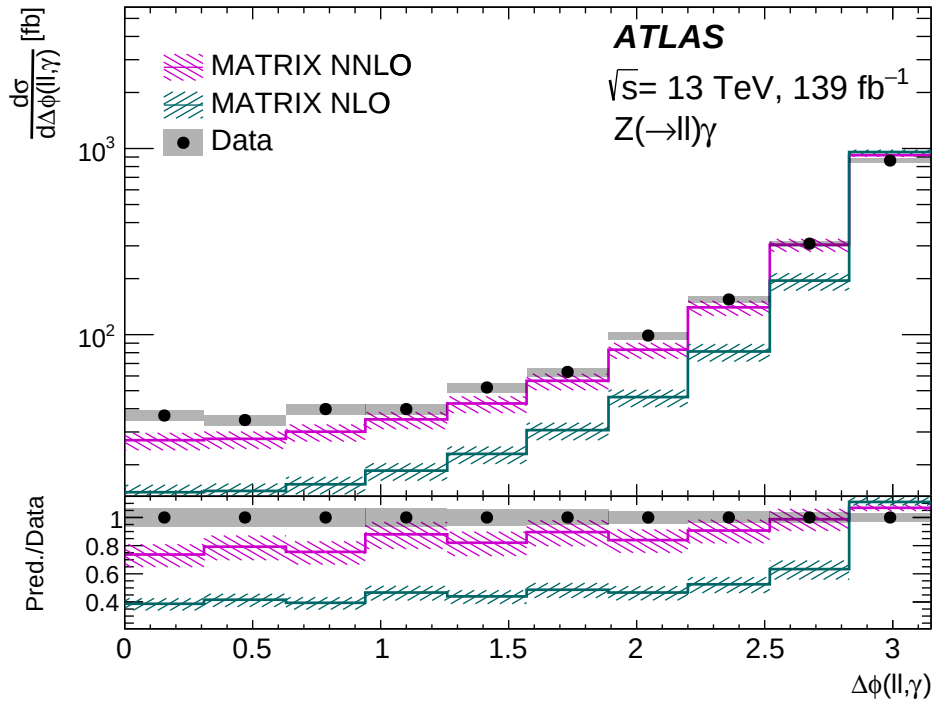


(b)

Figure 5.12: The differential fiducial cross-section measurements as a function of (a) the ratio of the transverse momentum to the invariant mass of the three-body system and (b) the azimuthal separation of the photon and dilepton system, compared to predictions from MATRIX [26].

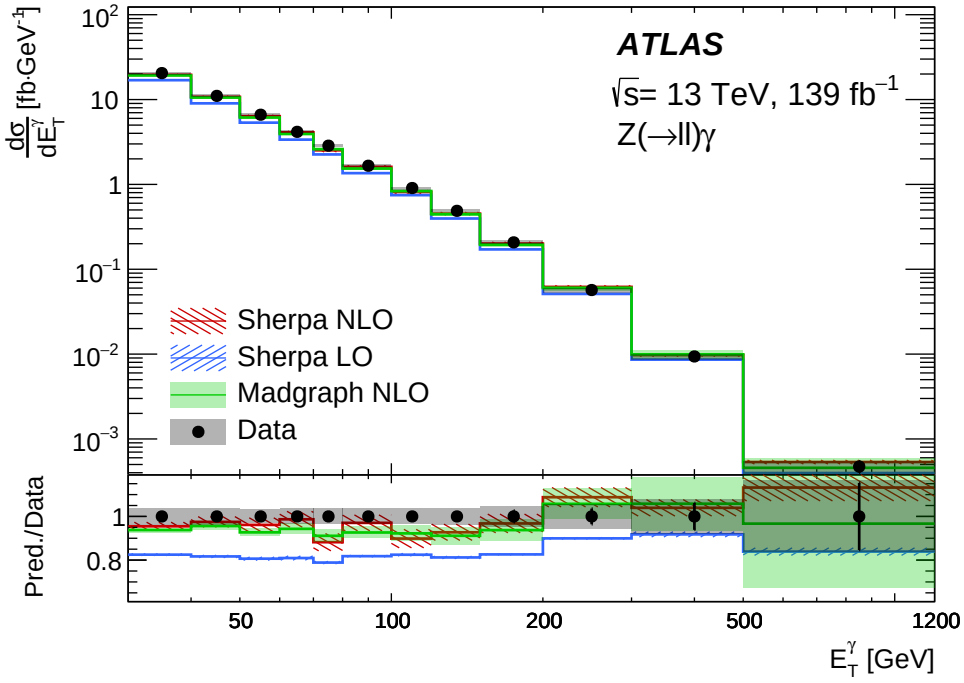


(a)

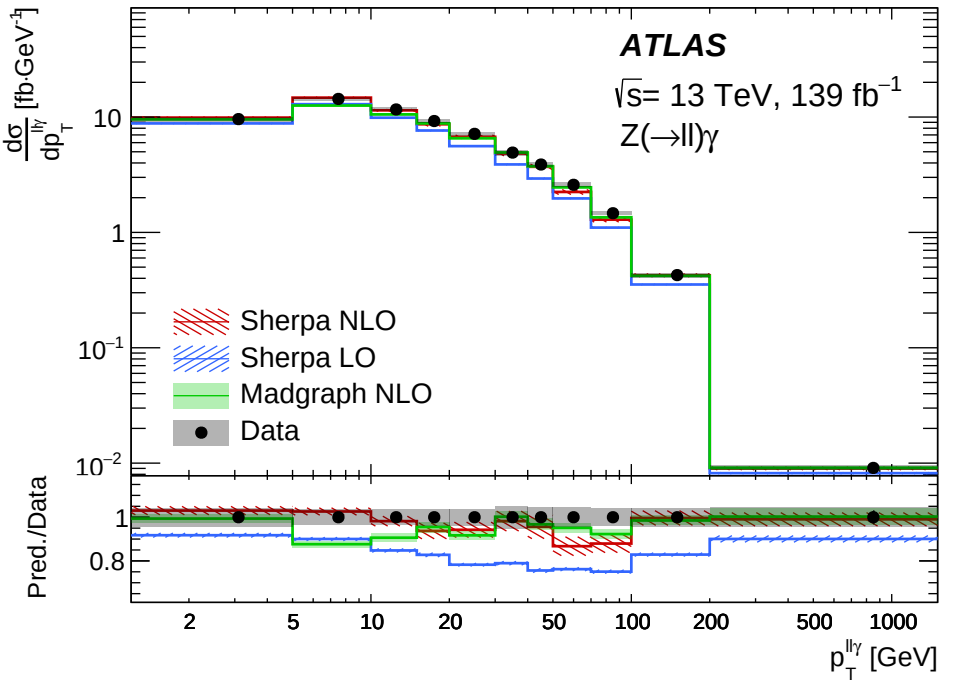


(b)

Figure 5.13: The differential fiducial cross-section measurements as a function of (a) the photon transverse energy and (b) the transverse momentum of the three-body system, compared to predictions from the Sherpa and MadGraph MC generators [26].

# CHAPTER 6

# Measurements of $Z(\rightarrow \ell\ell)\gamma\gamma$ Production

This chapter details the selection of $Z(\rightarrow ee)\gamma\gamma$ and $Z(\rightarrow \mu\mu)\gamma\gamma$ events from $pp$ collision data, the estimation of the backgrounds contributing to these processes and the fiducial cross-section results. The integrated fiducial cross-sections are measured in both channels, and differential fiducial cross-sections are measured as functions of: the leading photon transverse energy ($E_T^{\gamma 1}$), the subleading photon transverse energy ($E_T^{\gamma 2}$), the dilepton transverse momentum ($p_T^{\ell\ell}$), the transverse momentum of the 4-body system ($p_T^{\ell\ell\gamma\gamma}$), the diphoton invariant mass ($m_{\gamma\gamma}$) and the 4-body invariant mass ($m_{\ell\ell\gamma\gamma}$).

The detector and fiducial selections are presented in Section 6.1 along with a description of the data and signal samples used. The method and results of estimating the fake photon background are described in Section 6.2. The remaining backgrounds are explained in Section 6.3. The detector-level data are compared to full predictions in Section 6.4. The procedure used to perform the cross-section extraction is detailed in Section 6.5. The uncertainties related to the SM predictions (first intro-

duced in Section 1.7.2) are described in Section 6.6. Finally, the results are given in Section 6.7.

## 6.1 Selections and samples

### 6.1.1 Detector-level selection

The following describes the signal region (SR) selection. As explained in Section 4.1, events are selected which fire one of the single lepton triggers. These events are required to have at least one vertex reconstructed (as detailed in Section 4.2.2), and the one with the highest $\Sigma p_T^2$ is chosen as the primary vertex (PV).

The preselection requirements placed on all electron objects are:

- $p_{\mathrm{T}} > 20$ GeV
- $|\eta| < 2.47$ and not $1.37 < |\eta| < 1.52$
- consistency with track originating from the PV
- *Medium* electron identification criteria
- *Loose* electron isolation criteria

The preselection requirements placed on all muon objects are:

- $p_{\mathrm{T}} > 20$ GeV
- $|\eta| < 2.5$
- consistency with track originating from the PV
- *Medium* muon identification criteria
- *Loose* muon isolation criteria

The preselection requirements placed on all photon objects are:

- $p_{\mathrm{T}} > 20$ GeV
- $|\eta| < 2.37$ and not $1.37 < |\eta| < 1.52$
- *Loose* photon identification criteria

Similarly to the $Z\gamma$ analysis, the preselection requirements are used to define an inclusive sample which is not tighter than the requirements placed at the trigger level. The minimum photon $p_{\mathrm{T}}$ requirement is raised to 20 GeV due to the limits of some MC samples used. Photons are removed if they are within $\Delta R < 0.4$ of an electron or muon and electrons are removed if they are within $\Delta R < 0.2$ of a muon, to suppress contributions from bremsstrahlung photons. Events are considered further if they contain at least two reconstructed electrons or muons and at least two reconstructed photons passing the preselection requirements.

In both channels, the leading lepton is required to have $p_{\mathrm{T}} > 30$ GeV in order to be above the single lepton trigger thresholds. The highest $p_{\mathrm{T}}$ opposite-sign same-flavour lepton pair is then selected as the $Z$ candidate and is required to have an invariant mass of $m_{\ell\ell} > 40$ GeV to remove contributions from low mass Drell-Yan production and resonances. If an electron pair is selected, the leading electron is required to pass the *Tight* identification cut, which corresponds with the identification cut applied in the lowest $p_{\mathrm{T}}$ single electron trigger used. If a muon pair is selected, then the leading muon must pass the *Tight* isolation criteria, which corresponds with the isolation cut applied in the lowest $p_{\mathrm{T}}$ single muon trigger used.

The two highest $p_{\mathrm{T}}$ photons in the event are selected. Both of the photons must pass the *FixedCutLoose* isolation and *Tight* identification cuts, and be separated by $\Delta R > 0.4$.

Finally, the contribution from FSR photons is removed by placing a cut on the invariant masses of objects in the event: $m_{\ell\ell} + \min(m_{\ell\ell\gamma_1}, m_{\ell\ell\gamma_2}) > 2m_Z$, where $\gamma_1$ refers to the leading photon and $\gamma_2$ refers to the subleading photon. For the case

where both photons are produced via ISR (the desired signal process), the dilepton mass will be approximately equal to the $Z$ mass and both three-body invariant masses will be larger than the $Z$ mass. For the cases where an FSR photon is present, the dilepton invariant mass will be less than the $Z$ mass and the largest value that the minimum of the two three-body masses can take is approximately the $Z$ mass. This cut is visualised in Figure 6.1, where the ISR and FSR populations can be clearly distinguished.

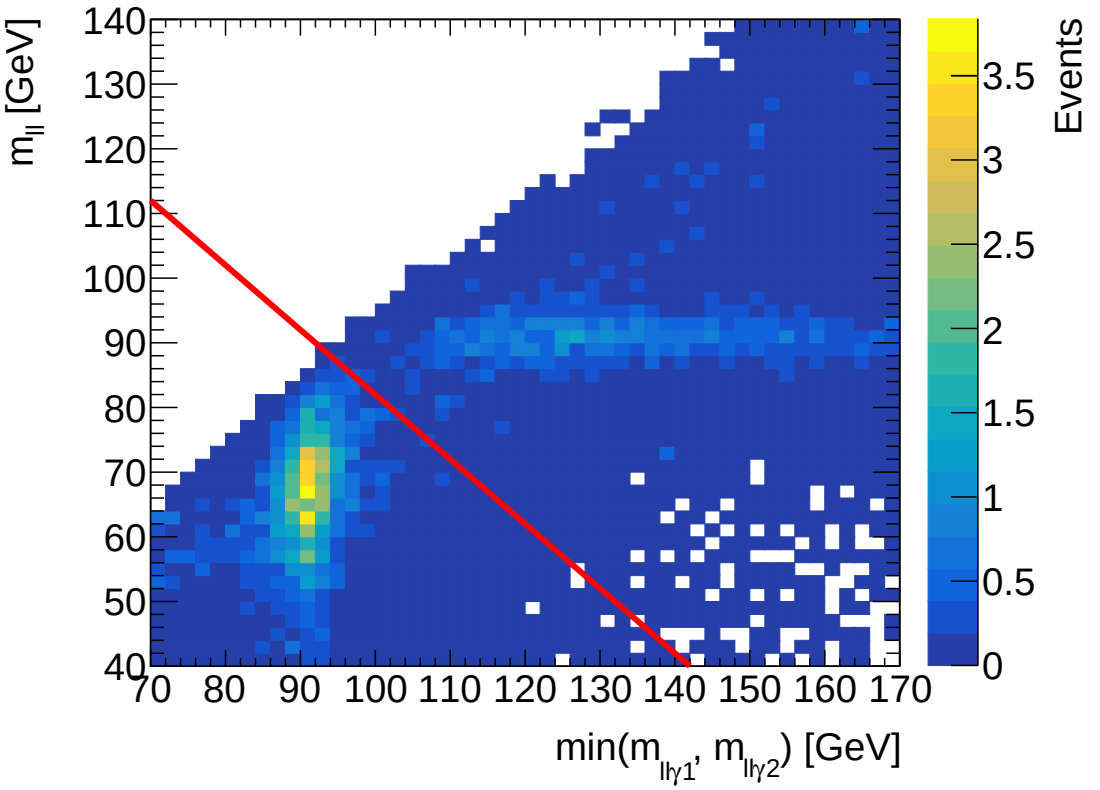


Figure 6.1: The dilepton invariant mass versus the minimum of the two three-body masses formed from the dilepton system and each of the photons, in the signal MC. The ISR population is centred around $m_Z$ in the dilepton invariant mass distribution.

### 6.1.2 Fiducial-level selection

The fiducial-level selection is designed to be as close as possible to the detector-level selection, and is based on truth-level objects (defined in Section 4.4) as opposed to detector-level objects. The truth-level lepton objects considered are 'dressed' which

means that the four-momenta of any photons within $\Delta R < 0.1$ are added to the lepton, in order to catch any nearby photon energy which is radiated. A common lepton kinematic selection is applied to both channels, which allows for a simple combination of the channels.

The truth-level lepton selection requirements are:

- leading lepton $p_{\mathrm{T}} > 30$ GeV
- subleading lepton $p_{\mathrm{T}} > 20$ GeV
- $|\eta| < 2.47$
- $m_{\ell\ell} > 40$ GeV

The truth-level photon selection requirements are:

- $p_{\mathrm{T}} > 20$ GeV
- $|\eta| < 2.37$
- $\Delta R(\gamma, \ell) > 0.4$
- $E_T^{cone20}/E_T^{\gamma} < 0.07$

The event is required to have at least two fiducially selected electrons or muons and at least two fiducially selected photons. The two highest $p_{\mathrm{T}}$ fiducial photons are selected and required to be separated by $\Delta R > 0.4$. Finally, the FSR removal cut is also applied using truth-level objects: $m_{\ell\ell} + \min(m_{\ell\ell\gamma_1}, m_{\ell\ell\gamma_2}) > 2m_Z$.

The truth-level photon isolation cuts are chosen following the same procedure as detailed in Section 5.3.2. The ratio of the number of events passing the detector-level isolation cut to the number which fail, as a function of the truth-level isolation variable is shown in Figure 6.2. The cut value is found to be consistent for the leading and subleading photons, and is also the same as the cut value determined in the $Z\gamma$ analysis.

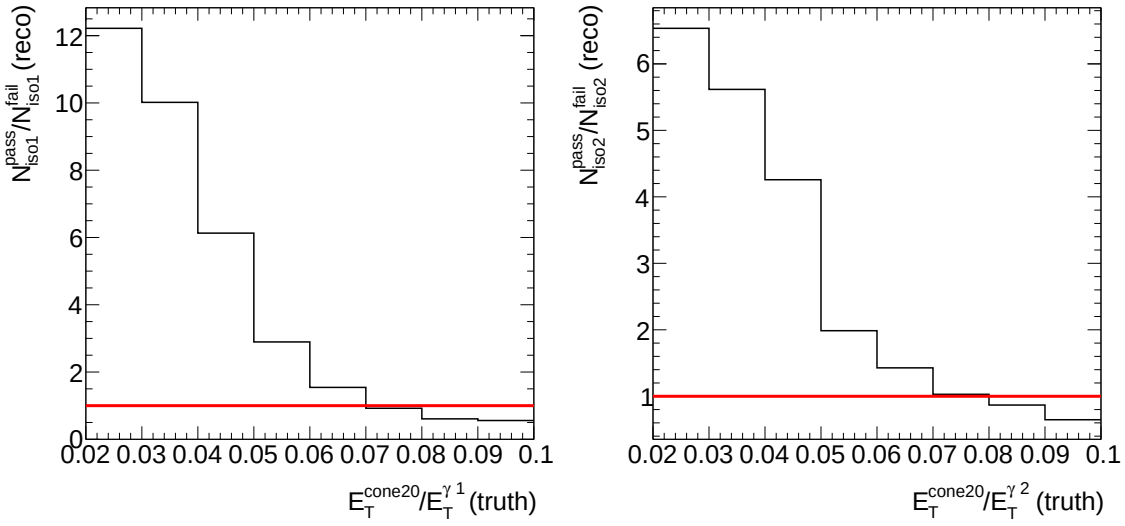


(a) (b)

Figure 6.2: Ratio of number of detector-level events passing the detector-level isolation cut to the number which fail, in bins of the truth-level isolation variable for (a) the leading photon and (b) the subleading photon.

### 6.1.3 Data and signal samples

The data used correspond to an integrated luminosity of 139 fb$^{-1}$, recorded from $pp$ collisions at $\sqrt{s} = 13$ TeV between 2015-2018. Any data which are recorded when any component of the detector is not fully functional are not considered.

The baseline simulated signal sample is generated with Sherpa 2.2.10 at NLO, with up to two additional partons at LO accuracy. The sample is generated to be uniform in the variable $\max(p_T^\gamma, m_{\gamma\gamma})$ which leads to a more even population of MC events across the full phase space being probed. The events are then reweighted to recover the expected distribution in this variable.

An alternative signal sample is provided by Sherpa 2.2.4 at LO accuracy, with up to two additional partons. The sample is generated in three separate bins of photon $p_{\mathrm{T}}$ and $m_{\gamma\gamma}$ to provide a more even distribution of events in the regions being probed.

Both signal samples are generated with the same Frixione photon isolation parameters as are used in the $Z\gamma$ analysis; $\delta_0 = 0.1$, $\epsilon = 0.1$ and $n = 2$ (defined in

Section 5.3.3).

## 6.2 Fake photon backgrounds

The largest background to the $Z\gamma\gamma$ final state is from events with a $Z$ and at least one jet faking a photon. Three processes make up the background: $Z\gamma j$ where the subleading photon is faked by a jet, $Zj\gamma$ where the leading photon is faked by a jet and $Zjj$ where both photons are faked by jets. Using the control region definitions in Section 4.3.1, generalised to the case of two photons, the number of events in the signal region (AA), can be written as

$$N^{AA} = N^{AA}_{Z\gamma\gamma} + N^{AA}_{Z\gamma j} + N^{AA}_{Zj\gamma} + N^{AA}_{Zjj} + N^{AA}_{bkg}, \tag{6.1}$$

where $N^{AA}_{Z\gamma\gamma}$ is the contribution from the signal process and $N^{AA}_{bkg}$ is the contribution from other background processes (i.e. not fake photon backgrounds). The contributions from these other background processes are ignored in the following discussion of fake photon backgrounds, but are described in full in Section 6.3. The rate at which jets fake photons is poorly modelled in simulation, so data-driven techniques are used to estimate the sizes of these backgrounds. The primary method used in the $Z\gamma\gamma$ analysis is known as the matrix method.

### 6.2.1 Matrix method

The matrix method is performed on a data sample where the full event selection is applied apart from the photon identification and photon isolation requirements. As described in Section 4.3.1, where the regions A, B, C and D are defined, the photon candidates are also required to satisfy the *LoosePrime4* working point to reduce the correlation between identification and isolation of the jets.

The inclusive yields for each of the four processes in this loose sample are denoted

as $W_{Zxy}$, where $xy = \gamma\gamma$, $\gamma j$, $j\gamma$ or $jj$. Efficiency factors are used to calculate the contribution of each process to the signal region. These efficiencies are expected to be different for true photons and for fake photons, so the efficiencies $\epsilon_{1,2}$ are defined for true photons and the fake rates $f_{1,2}$ are defined for fake photons. The indices 1 and 2 correspond to the leading and subleading photon candidates respectively. The number of events in the signal region ($N^{AA}$) can then be written as the sum of four components

$$N^{AA} = N^{AA}_{Z\gamma\gamma} + N^{AA}_{Z\gamma j} + N^{AA}_{Zj\gamma} + N^{AA}_{Zjj} = W_{Z\gamma\gamma}\epsilon_1\epsilon_2 + W_{Z\gamma j}\epsilon_1 f_2 + W_{Zj\gamma} f_1\epsilon_2 + W_{Zjj} f_1 f_2. \tag{6.2}$$

By considering three additional control regions, AB, BA and BB, where respectively, each and both of the photon candidates are required to fail the isolation requirement, and inverting the corresponding efficiencies and fake rates, one can write down three more equations. These can be written as a 4×4 matrix equation:

$$\begin{pmatrix} N^{AA} \\ N^{AB} \\ N^{BA} \\ N^{BB} \end{pmatrix} = \begin{pmatrix} \epsilon_1\epsilon_2 & \epsilon_1 f_2 & f_1\epsilon_2 & f_1 f_2 \\ \epsilon_1(1-\epsilon_2) & \epsilon_1(1-f_2) & f_1(1-\epsilon_2) & f_1(1-f_2) \\ (1-\epsilon_1)\epsilon_2 & (1-\epsilon_1)f_2 & (1-f_1)\epsilon_2 & (1-f_1)f_2 \\ (1-\epsilon_1)(1-\epsilon_2) & (1-\epsilon_1)(1-f_2) & (1-f_1)(1-\epsilon_2) & (1-f_1)(1-f_2) \end{pmatrix} \begin{pmatrix} W_{Z\gamma\gamma} \\ W_{Z\gamma j} \\ W_{Zj\gamma} \\ W_{Zjj} \end{pmatrix}, \tag{6.3}$$

This also means that the $\epsilon_{1,2}$ and $f_{1,2}$ are explicitly *isolation* efficiencies and fake rates. Once the values for the efficiencies and fake rates have been determined, the matrix is inverted and applied to the left-hand side of this equation to determine the unknown yields for each process, $W_{Zxy}$.

The efficiencies correspond to the rate at which a photon that is identified as *Tight*, passes the isolation requirement. These are calculated from the signal MC, denoted by the subscript 'sig', as

$$\epsilon_1 = \frac{N^{AA}_{sig}}{N^{AA}_{sig} + N^{BA}_{sig}},\ \epsilon_2 = \frac{N^{AA}_{sig}}{N^{AA}_{sig} + N^{AB}_{sig}}. \tag{6.4}$$

The isolation fake rates are calculated in data using *LoosePrime4* photon candidates

which fail the *Tight* identification cut as

$$f_1 = \frac{N^{CA}}{N^{CA} + N^{DA}},\ f_2 = \frac{N^{AC}}{N^{AC} + N^{AD}}. \tag{6.5}$$

In these control regions, the other photon candidate is required to pass both the isolation and identification cuts (A), as these regions are well populated and are expected to best describe the two largest fake background components ($Z\gamma j$ and $Zj\gamma$). As these control regions are not completely pure in background events, signal leakage into these regions must also be accounted for. The signal leakage ($N_{sig}^{XY}$) is estimated directly from the simulated signal samples.

The isolation fake rates are calculated in a control region where the photon candidate is required to fail *Tight* identification. This introduces a bias as a jet candidate is more likely to fail the isolation cut if it has already failed the identification cut. This bias is corrected for by the correlation parameters $R_1$ and $R_2$ which are defined as

$$R_1 = \frac{N^{AX}N^{DX}}{N^{BX}N^{CX}},\ R_2 = \frac{N^{XA}N^{XD}}{N^{XB}N^{XC}}, \tag{6.6}$$

and are applied to the C control region yields in the definition of the fake rates. The superscript $X$ means there is no isolation or identification requirement placed on the other photon candidate. The values of $R_1$ and $R_2$ are estimated from simulation, described later in Section 6.2.3.2.

The above equations (6.5) for the fake rates are thus modified to give

$$f_1 = \frac{(N^{CA} - N_{sig}^{CA})R_1}{(N^{CA} - N_{sig}^{CA})R_1 + N^{DA} - N_{sig}^{DA}},\ f_2 = \frac{(N^{AC} - N_{sig}^{AC})R_2}{(N^{AC} - N_{sig}^{AC})R_2 + N^{AD} - N_{sig}^{AD}}. \tag{6.7}$$

With the efficiencies and fake rates determined, the yields for each process $W_{Zxy}$ can be deduced. The contribution from each process in the signal region can then be calculated from each term in Equation 6.2.

### 6.2.2 Closure test

The matrix method is tested using a pseudo-dataset formed from the signal MC and multiple simulation samples representing the fake background components. For the $Z\gamma j$ and $Zj\gamma$ components, a $Z\gamma$+jets sample is used, generated with Sherpa 2.2.4 [16] at LO. The $Zj\gamma$ ($Z\gamma j$) component is selected by requiring that the (sub)leading photon candidate is truth-matched to a photon originating from a hadron decay (i.e. corresponding to a fake photon). An alternative sample for the $Z\gamma j$ and $Zj\gamma$ components is provided by MadGraph [17] at NLO. The $Zjj$ component is provided by a $Z$+jets simulation sample generated with Powheg [18] which includes the matrix element calculation at NLO and is interfaced to PYTHIA [20] to provide the parton shower and hadronisation.

The $Z\gamma$+jets and $Z$+jets simulations are known to model the normalisation of the fake backgrounds poorly, hence the need for a data-driven method. Normalisation factors are derived to make the pseudo-dataset more representative of the data. Three control regions: AD, DA and DD, are chosen to derive normalisation factors, each of which is expected to be dominated by one component of the fake background. The normalisation factors for each component ($F_{Z\gamma j}$, $F_{Zj\gamma}$ and $F_{Zjj}$) are determined by solving the following set of equations:

$$N_{data}^{AD} - N_{sig}^{AD} = F_{Z\gamma j} N_{Z\gamma+jet}^{AD} + F_{Zjj} N_{Z+jets}^{AD} \tag{6.8}$$

$$N_{data}^{DA} - N_{sig}^{DA} = F_{Zj\gamma} N_{Zjet+\gamma}^{DA} + F_{Zjj} N_{Z+jets}^{DA} \tag{6.9}$$

$$N_{data}^{DD} - N_{sig}^{DD} = F_{Z\gamma j} N_{Z\gamma+jet}^{DD} + F_{Zj\gamma} N_{Zjet+\gamma}^{DD} + F_{Zjj} N_{Z+jets}^{DD}. \tag{6.10}$$

The signal leakage into each region is taken from the baseline signal MC and the remaining events are assumed to be made up from the background components. It is assumed that there is no leakage of $Z\gamma j$ events into DA and no leakage of $Zj\gamma$ events into AD. The normalisation factors are found to be $F_{Z\gamma j} = 2.0$, $F_{Zj\gamma} = 1.4$ and $F_{Zjj} = 9.4$. The final pseudo-dataset is formed of the baseline signal MC and the three background MCs, normalised by their respective normalisation factors.

The matrix method is performed on this pseudo-dataset, and the results for the different component breakdowns in each of the regions are shown in Figure 6.3. The extracted signal region yields are compared to the expectation from MC in Table 6.1, which demonstrates that the method is able to accurately reproduce the fake background yields. The statistical uncertainty is estimated by performing the method on 1000 sets of toy data which are randomly drawn using a probability density function formed from the original pseudo-dataset distribution.

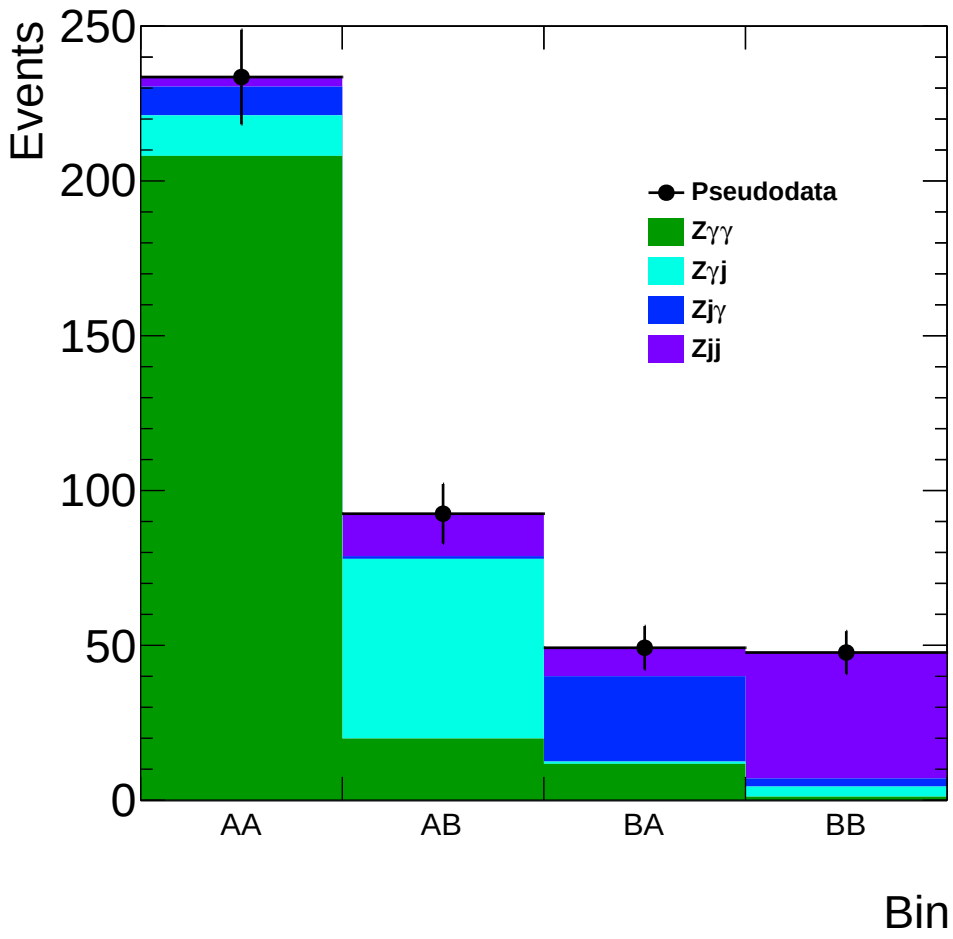


Figure 6.3: The pseudo-dataset yield breakdowns in the signal region and each of the control regions, as estimated using the matrix method.

| | $N^{AA}_{Z\gamma\gamma}$ | $N^{AA}_{Z\gamma j}$ | $N^{AA}_{Zj\gamma}$ | $N^{AA}_{Zjj}$ |
|---|---|---|---|---|
| Expected | 210.9±1.3 | 10.6±2.3 | 6.1±1.5 | 6.0±4.3 |
| Matrix method result | 208±17 | 13.1±5.1 | 9.3±4.2 | 3.1±1.5 |

Table 6.1: The yields for each process, extracted from a pseudo-dataset using the matrix method, compared to the normalised expected values from simulation. The uncertainties quoted are statistical.

### 6.2.3 Systematic uncertainties

Five sources of systematic uncertainty are considered for the matrix method. Two are related to the fixed input parameters: the photon isolation efficiencies and the correlation parameters; two are related to the definition of the fake-enriched background control regions: the *LoosePrime* working point and isolation energy gap definition; and the final one comes from the number of signal MC events.

#### 6.2.3.1 Isolation efficiency

The method is performed inclusively, i.e. it is not binned, due to the relatively small number of events in the signal region. This means that the central value of the photon isolation efficiency may not accurately describe all the events being used. This statement can be tested by looking at variables which describe the amount of hadronic activity within the event, which will then influence the isolation efficiency. The isolation efficiencies are studied as a function of $p_T^{\ell\ell\gamma\gamma}$ and $\langle\mu\rangle$, and the values are given in Table 6.2.

| | Inclusive [%] | $p_T^{\ell\ell\gamma\gamma} < 25$ [%] | $25 < p_T^{\ell\ell\gamma\gamma} < 75$ [%] | $75 < p_T^{\ell\ell\gamma\gamma}$ [%] |
|---|---|---|---|---|
| $\epsilon_1$ | 94.3±0.2 | 95.4±0.2 | 93.8±0.3 | 92.9±0.3 |
| $\epsilon_2$ | 90.9±0.2 | 92.3±0.2 | 89.9±0.4 | 89.3±0.3 |
| | Inclusive [%] | $\langle\mu\rangle < 20$ [%] | $20 < \langle\mu\rangle < 40$ [%] | $40 < \langle\mu\rangle$ [%] |
| $\epsilon_1$ | 94.3±0.2 | 95.1±0.4 | 94.6±0.2 | 93.1±0.3 |
| $\epsilon_2$ | 90.9±0.2 | 93.2±0.5 | 91.4±0.2 | 88.2±0.4 |

Table 6.2: Comparison of the photon isolation efficiencies across different bins describing the hadronic activity within the event. The units of $p_T^{\ell\ell\gamma\gamma}$ are GeV.

Based on these values, a systematic uncertainty of $\pm 2\%$ is assigned to $\epsilon_1$ and $\pm 3\%$ to $\epsilon_2$ which covers all the variations with hadronic activity. For each efficiency, the average of the up and down variations is taken as the systematic uncertainty on the extracted yields due to that efficiency. The uncertainties due to both isolation efficiencies are added in quadrature which amounts to an uncertainty of 8% on the total fake photon background yield.

#### 6.2.3.2 Correlation parameters

The correlation parameters $R_1$ and $R_2$ (defined in Equations 6.6) are calculated from the Sherpa and MadGraph $Z\gamma$+jets MC, as well as the Powheg $Z$+jets MC. In the $Z\gamma$+jets MCs, $R_1$ ($R_2$) is calculated from $Zj\gamma$ ($Z\gamma j$) events by truth-matching the (sub)leading photon candidate to a photon originating from a hadron decay. In the $Z$+jets MC, both photons are required to be truth-matched to a photon originating from a hadron decay to ensure $Zjj$ events are being considered. The values of $R_1$ and $R_2$ calculated from each simulation are given in Table 6.3. A single value of $R$ is produced from each of the MCs by combining the values for the leading and subleading jet candidates which improves the statistical precision. The final value taken for the correlation is the average of $R$ from each of the three MCs, which is $1.18 \pm 0.11$ and is used in the method for both $R_1$ and $R_2$. The uncertainty on the correlations is increased to 0.18, which covers the case where there is no correlation ($R = 1.0$) and is more conservative. The averages of the up and down variations of each correlation are summed in quadrature to determine the systematic uncertainty on the extracted yields. This results in a systematic uncertainty of 10% on the total fake photon background yield.

#### 6.2.3.3 LoosePrime definition

The effect of the choice of the *LoosePrime* working point (see Table 4.1) in the definition of the CRs in which the fake rates are calculated is investigated by comparison

| | $Z\gamma$+jets MC (Sherpa) | $Z\gamma$+jets MC (MadGraph) | $Z$+jets MC |
|---|---|---|---|
| $R_1$ | 0.74±0.23 | 1.23±0.21 | 1.62±0.40 |
| $R_2$ | 1.22±0.33 | 1.15±0.16 | 1.30±0.13 |
| $R$ | 0.92±0.19 | 1.18±0.13 | 1.44±0.25 |

Table 6.3: Comparison of identification-isolation correlation parameters calculated from the fake background simulations. All uncertainties are statistical.

with an alternative working point. The difference between the extracted yields when using the *LoosePrime5* working point to define the control regions, relative to the nominal *LoosePrime4* results, is assigned as the systematic uncertainty. This results in a 3% systematic uncertainty on the total fake photon background yield.

#### 6.2.3.4 Isolation energy gap

The effect of the choice of isolation energy gap, used to define the failed isolation control regions (see Section 4.3.1), is investigated by varying the nominal value of $E_{gap} = 2$ GeV to 1 and 0 GeV. The effect of increasing $E_{gap}$ further is not considered as this results in a too severe reduction of events in the non-isolated control regions. The largest difference from the nominal value when considering each of these two variations is found to be 11%, and is hence taken as the systematic uncertainty on the total fake photon background yield.

#### 6.2.3.5 MC statistical uncertainty

The systematic uncertainties on the extracted yields due to the limited MC statistics are propagated through the signal leakage numbers and photon efficiencies. This amounts to only a small effect of 1% on the total fake photon background yield.

### 6.2.4 Matrix method results

The predicted prompt photon backgrounds, to be described in the following Section 6.3, are subtracted from the data yields in the signal region. The resulting yields therefore consist of only the fake photon background and signal processes. The yields are combined from both the electron and muon channels, resulting in a total of approximately 300 signal region events. The prompt photon backgrounds are also subtracted in each of the three control regions. The matrix method is then performed to determine the breakdown in the signal region, the results of which are given in Table 6.4.

The sum of the three background components ($N_{fakes} = 64.2$) is used to assess the uncertainties, as this encapsulates any correlations between the components and is ultimately the value which enters the cross-section calculation. The dominant uncertainty is due to the data statistics, which has a value of $\pm 11.8$ for $N_{fakes}$. The largest sources of systematic uncertainty are due to the correlations and isolation energy gap, which lead to uncertainties of $\pm 6.2$ and $\pm 7.0$ respectively on the value of $N_{fakes}$.

| | $Z\gamma\gamma$ | $Z\gamma j$ | $Zj\gamma$ | $Zjj$ | Total fake $\gamma$ background |
|---|---|---|---|---|---|
| Yield | 234.1 | 26.2 | 29.0 | 9.0 | 64.2 |
| Total uncertainty | 25.0 | 11.2 | 11.2 | 4.5 | 16.0 |
| Statistical uncertainty | 22.5 | 8.3 | 9.0 | 3.4 | 11.8 |
| Systematic uncertainty | 10.7 | 7.6 | 6.5 | 2.9 | 10.7 |
| Isolation efficiency | 4.8 | 3.7 | 3.2 | 0.6 | 4.8 |
| Correlations | 6.2 | 4.4 | 4.8 | 2.0 | 6.2 |
| LoosePrime definition | 1.9 | 3.7 | 2.5 | 0.8 | 4.8 |
| Isolation energy gap | 7.0 | 3.4 | 1.9 | 1.8 | 7.0 |
| MC statistical uncertainty | 0.5 | 0.4 | 0.4 | 0.1 | 0.5 |

Table 6.4: Matrix method uncertainty breakdown for each of the fake photon background components.

### 6.2.5 Fake photon templates

The matrix method is able to provide only the normalisation of the fake photon backgrounds due to the limited number of events in the signal region. For the differential cross-section measurements, the shapes of these backgrounds as functions of the measured variables are also needed. The $Z\gamma j$ and $Zj\gamma$ shape templates are taken from the Sherpa $Z\gamma$+jets MC, and the $Zjj$ shapes are taken from the Powheg $Z$+jets MC, as described in Section 6.2.2. The templates are taken from a slightly loosened signal region, in which at most one of the four photon identification and isolation cuts is allowed to fail. This increases the number of available events whilst remaining as close to the signal region as possible. The templates are then normalised to the yields extracted by the matrix method.

An uncertainty on the shape of the templates is derived by comparing the shape of the overall fake background estimate (sum of all three components), using the templates from simulation, to the data in a fake-background enriched control region. This control region is defined by requiring at least two of the four photon identification and isolation cuts to fail, and hence it is dominated by the fake photon backgrounds. The templates from simulation are normalised using the factors derived in Section 6.2.2. The fractional difference between the shape of the data and the shape of the normalised templates is taken as the shape uncertainty on the fake photon background in each bin of the differential measurements.

## 6.3 Other backgrounds

### 6.3.1 $t\bar{t}\gamma\gamma$ background

The background to $\ell\ell\gamma\gamma$ from top processes is assessed in an opposite-sign different-flavour lepton control region. Applying the full event selection, 20 $e\mu\gamma\gamma$ events are selected in data. The $t\bar{t}\gamma\gamma$ background process is modelled by a $t\bar{t}\gamma$ simulation,

generated with MadGraph, where the second photon comes from showering. The contribution from fake photons is also considered, while other processes are assumed to be negligible and well covered within the uncertainty on the $t\bar{t}\gamma\gamma$ normalisation.

The contribution from fake photons is estimated using the matrix method described in the previous section. The photon isolation efficiencies are estimated from the $t\bar{t}\gamma$ MC. The fake rates are calculated in control regions where the photon candidates are required to fail Tight identification, but satisfy *LoosePrime5*. This working point is preferred over the nominal *LoosePrime4* as it increases the number of events available. Using the matrix method, the 20 events in data are divided into 17.4 $e\mu\gamma\gamma$, 2.0 $e\mu\gamma j$, 0.6 $e\mu j\gamma$ and 0.1 $e\mu jj$ events. The normalisation factor for the $t\bar{t}\gamma$ MC is then derived by dividing the signal yield extracted from the data by the $t\bar{t}\gamma$ MC yield in the $e\mu\gamma\gamma$ control region. This factor is found to be 0.70±0.15, where the uncertainty given is statistical. The normalised MC is compared to the data and fake photon background expectation in Figure 6.4, where a good agreement can be seen.

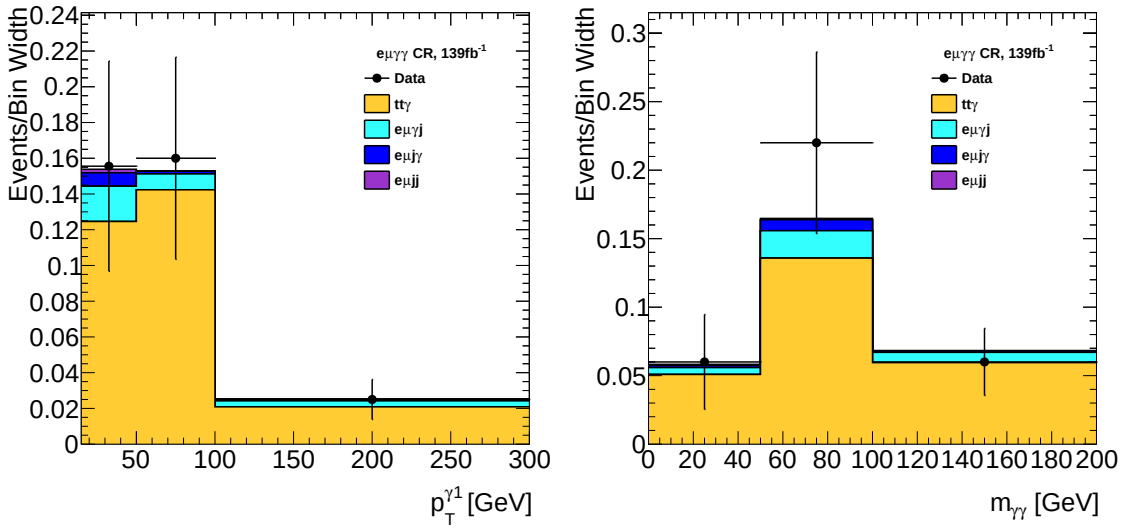


(a) (b)

Figure 6.4: The comparison of prediction to data in the $e\mu\gamma\gamma$ control region as a function of (a) leading photon $p_{\mathrm{T}}$ and (b) diphoton invariant mass.

For the implementation of the matrix method in the $e\mu\gamma\gamma$ control region, the same systematic effects are considered as for the signal region (described in Section 6.2.3).

The total systematic uncertainty on the $t\bar{t}\gamma$ normalisation factor due to the isolation efficiency, correlations, *LoosePrime* definition and isolation energy gap, is 0.02. The final normalisation factor of 0.70 $\pm$0.15 (stat) $\pm$0.02 (syst) is applied to the $t\bar{t}\gamma$ MC in the signal region. This predicts $\sim$ 15 $t\bar{t}\gamma\gamma$ events, which is approximately 5% of the data yield in the signal region.

### 6.3.2 Pile-up background

There are two pile-up background sources with prompt photons (i.e. not jets faking photons) which contribute to the $\ell\ell\gamma\gamma$ signal region at first order. The nature of these backgrounds was first introduced in Section 4.3.2. The first source is a single photon from a *pp* interaction overlapping with a $Z\gamma$ event from another, referred to as $Z\gamma + \gamma$. The second is a diphoton system overlapping with a $Z$ event, referred to as $Z + \gamma\gamma$. Due to the relatively small number of data events in the signal region, a data-driven method cannot be used to estimate the sizes of these backgrounds, as was done in the $Z\gamma$ analysis (Section 5.2.3). Instead, the contributions are estimated entirely from simulation, using a separate simulation for each of the four processes: $Z\gamma$, single-$\gamma$, $Z$ and $\gamma\gamma$.

For $Z\gamma + \gamma$, a random $Z\gamma$ event is subjected to the lepton and photon fiducial cuts detailed in Section 6.1. If at least two fiducial leptons and at least one fiducial photon is selected, then the fiducial photon selection is also applied to a random single-$\gamma$ event. All of the selected photons from both events are ordered by $p_{\mathrm{T}}$, and if the two highest $p_{\mathrm{T}}$ photons come from separate processes, the overlaid event is considered further. The remaining fiducial cuts which require all four objects are then applied. The selected events are used to calculate the fiducial level yields and distributions for the $Z\gamma + \gamma$ process. The number of events ($N_{Z\gamma+\gamma}$) is calculated as

$$N_{Z\gamma+\gamma} = \epsilon_{Z\gamma+\gamma}(\frac{\langle\mu\rangle\sigma_{\gamma}}{\sigma_{pp}})\sigma_{Z\gamma}L, \tag{6.11}$$

where $\epsilon_{Z\gamma+\gamma}$ is the selection efficiency of the overlaid events, $\langle\mu\rangle$ is the mean number

of interactions per bunch crossing, $\sigma_{pp} \sim 80$ mb is the total inelastic proton-proton cross-section [96] and $L$ is the integrated luminosity. The cross-sections, $\sigma_\gamma$ and $\sigma_{Z\gamma}$ are the predicted total cross-sections, i.e. without any fiducial cuts, from the single-$\gamma$ and $Z\gamma$ samples. Such cross-sections are referred to as generator-level cross-sections.

The estimation of the $Z + \gamma\gamma$ process is similar but simpler as the lepton fiducial selection is only applied to the $Z$ event and the photon fiducial selection is only applied to the diphoton event. The number of events ($N_{Z+\gamma\gamma}$) is calculated as

$$N_{Z+\gamma\gamma} = \epsilon_{Z+\gamma\gamma}(\frac{\langle\mu\rangle\sigma_{\gamma\gamma}}{\sigma_{pp}})\sigma_Z L, \tag{6.12}$$

where $\epsilon_{Z+\gamma\gamma}$ is the selection efficiency of the overlaid events and $\sigma_{\gamma\gamma}$ and $\sigma_Z$ are the respective generator-level cross-sections for the diphoton and $Z$ processes.

For both backgrounds, the fiducial-level yields and distributions are corrected to the detector level using 'folding' factors derived from the $Z\gamma\gamma$ signal MC. This is effectively the reverse of the bin-by-bin unfolding procedure outlined in Section 4.4.1. The correction factors are calculated inclusively and in each of the bins of the differential measurements. This calculation is discussed in more detail in Section 6.5.2. The total yields for the pile-up background processes, corresponding to an integrated luminosity of 139 fb$^{-1}$ are given in Table 6.5. These backgrounds contribute 2.6% of the data events in the signal region.

| | $ee\gamma\gamma$ | $\mu\mu\gamma\gamma$ |
|---|---|---|
| $Z\gamma + \gamma$ | 2.1±0.2 | 2.7±0.2 |
| $Z + \gamma\gamma$ | 1.44±0.04 | 1.90±0.05 |

Table 6.5: Pile-up background yields in the signal region for each channel.

### 6.3.3 Remaining backgrounds

The treatment of jets misidentified as photons is discussed in Section 6.2. Photons may also be faked by electrons, where either the track is missed, or falsely combined

with another track-cluster pair to form a photon conversion candidate. The two processes which contribute to these backgrounds at first order are $ZZ \to \ell\ell\ell\ell$ and $WZ\gamma \to \ell\ell\ell\gamma$. Both these processes are modelled by simulation. A 50% uncertainty is assigned to these backgrounds, based on measurements of $e \to \gamma$ fake rates using Run-2 data [59], which are shown to be poorly modelled in some regions of phase space. The total signal region prediction for these two processes is 3.5±1.7 events.

A final source of background from Higgs production in association with a $Z$, $Z(\to \ell\ell)H(\to \gamma\gamma)$, is estimated directly from simulation. Approximately two $ZH$ events are expected in the signal region.

## 6.4 Detector-level comparison

The data are compared to the full prediction inclusively and as functions of the variables which are unfolded. The fake photon backgrounds (shown in Table 6.4) are calculated using both channels combined as the contributions are assumed to be independent of how the $Z$ boson decays and the small differences in the kinematic selection. In order to get the fake photon background expectation in each channel, the fractional fake background is used. For example, the number of fakes in the electron channel ($N^{ee\gamma\gamma}_{fakes}$) is calculated as

$$N^{ee\gamma\gamma}_{fakes} = (N^{ee\gamma\gamma}_{data} - N^{ee\gamma\gamma}_{prompt\ bkg})\frac{N^{\ell\ell\gamma\gamma}_{fakes}}{N^{\ell\ell\gamma\gamma}_{data} - N^{\ell\ell\gamma\gamma}_{prompt\ bkg}}. \tag{6.13}$$

### 6.4.1 Results

The data yield, individual background predictions and total background prediction are shown in Table 6.6 for each channel. The signal yield is determined by subtracting the total background prediction from the data in each channel. The signal yields are compared to the detector-level predictions from Sherpa LO and NLO in Table 6.7. Both predictions agree with the data, within $1.6\sigma$ in the electron channel,

and within $0.5\sigma$ in the muon channel. In both channels, the data are slightly better described by the NLO prediction.

| | $e^+e^-\gamma\gamma$ | $\mu^+\mu^-\gamma\gamma$ |
|---|---|---|
| $N_{data}$ | 148 | 171 |
| $N_{fakes}$ | $29.8 \pm 5.5$ (stat) $\pm 5.0$ (syst) | $34.4 \pm 6.3$ (stat) $\pm 5.7$ (syst) |
| $N_{t\bar{t}\gamma\gamma}$ | $6.4 \pm 0.4$ (stat) $\pm 1.3$ (syst) | $8.4 \pm 0.5$ (stat) $\pm 1.8$ (syst) |
| $N_{Z\gamma+\gamma}$ | $2.07 \pm 0.16$ (stat) | $2.74 \pm 0.21$ (stat) |
| $N_{Z+\gamma\gamma}$ | $1.44 \pm 0.04$ (stat) | $1.90 \pm 0.05$ (stat) |
| $N_{ZH}$ | $1.08 \pm 0.01$ (stat) | $1.38 \pm 0.01$ (stat) |
| $N_{\ell\ell\ell\ell}$ | $1.03 \pm 0.10$ (stat) $\pm 0.51$ (syst) | $1.24 \pm 0.11$ (stat) $\pm 0.62$ (syst) |
| $N_{WZ\gamma}$ | $0.69 \pm 0.06$ (stat) $\pm 0.35$ (syst) | $0.52 \pm 0.05$ (stat) $\pm 0.26$ (syst) |
| $N_{bkg}$ | $42.5 \pm 7.6$ | $50.6 \pm 8.7$ |

Table 6.6: The total number of events in data passing the $Z\gamma\gamma$ signal region selection using the full Run-2 dataset, $N^{data}$, is compared to the expected number of background events in each channel. The fake background yield, $N_{fakes}$, is the sum of the $Z\gamma j$, $Zj\gamma$ and $Zjj$ yields. $N_{bkg}$ is the total background prediction in each channel.

| | $e^+e^-\gamma\gamma$ | $\mu^+\mu^-\gamma\gamma$ |
|---|---|---|
| $N_{sig}^{data}$ | $105.5 \pm 12.2$ (stat) $\pm 7.6$ (syst) | $120.4 \pm 13.1$ (stat) $\pm 8.7$ (syst) |
| $N_{sig}^{Sherpa\ LO}$ | $83.0 \pm 1.9$ (stat) | $112.2 \pm 2.3$ (stat) |
| $N_{sig}^{Sherpa\ NLO}$ | $91.5 \pm 0.9$ (stat) | $119.5 \pm 1.0$ (stat) |

Table 6.7: The measured number of signal events in data compared to the predicted number of signal events in each channel.

The signal expectation generated with Sherpa at NLO plus the full background prediction is compared to the data, as a function of the six measured variables in Figure 6.5 for the electron channel and Figure 6.6 for the muon channel. The binning used in these figures is not the same as the binning which will be used for the differential cross-section measurements; it is chosen to provide even bin widths across the range where most of the data are distributed. Reasonable agreement is seen in all bins, with the prediction typically within the statistical uncertainty of the data.

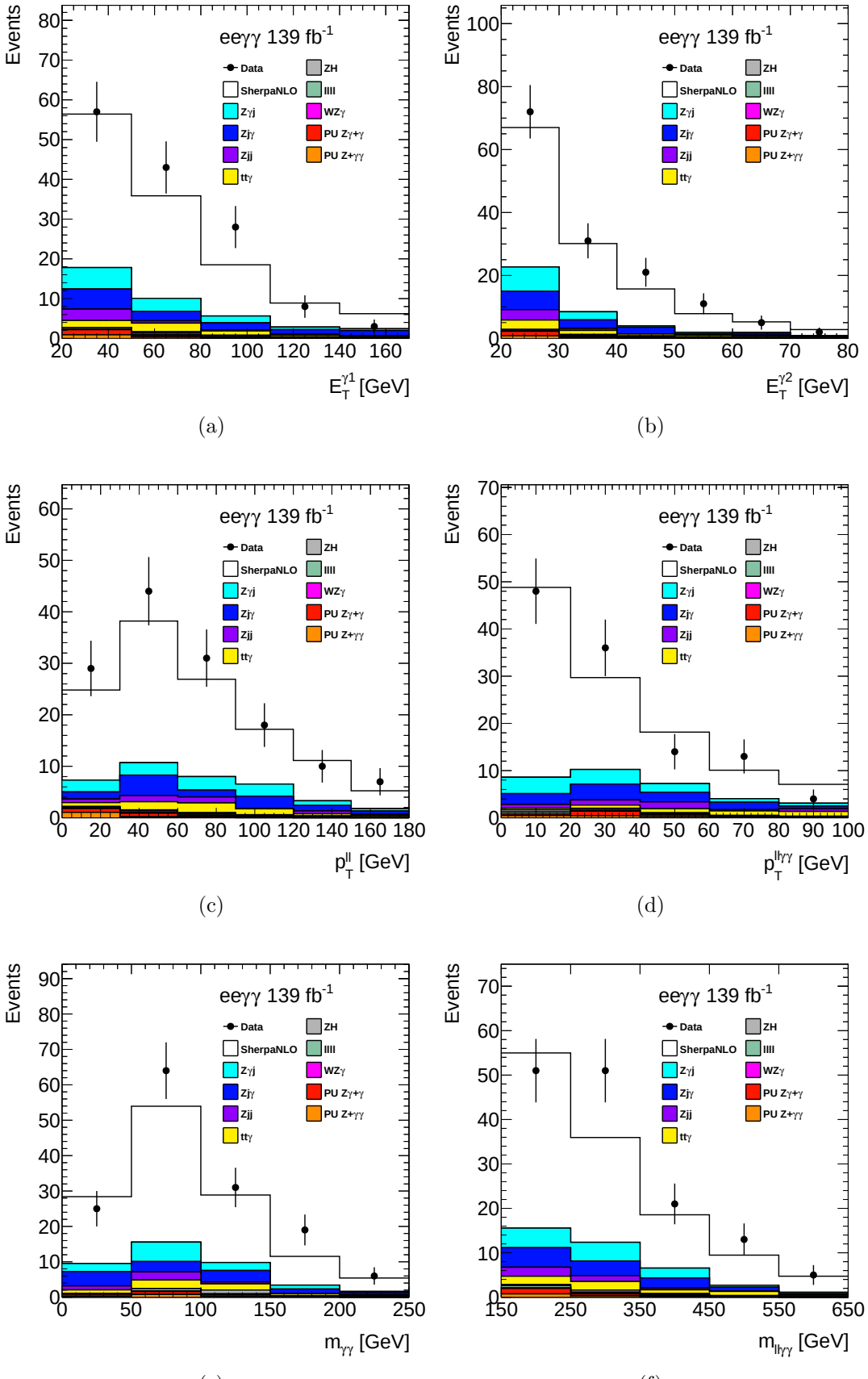


Figure 6.5: Detector-level distributions for the six measured variables in the $ee\gamma\gamma$ channel.

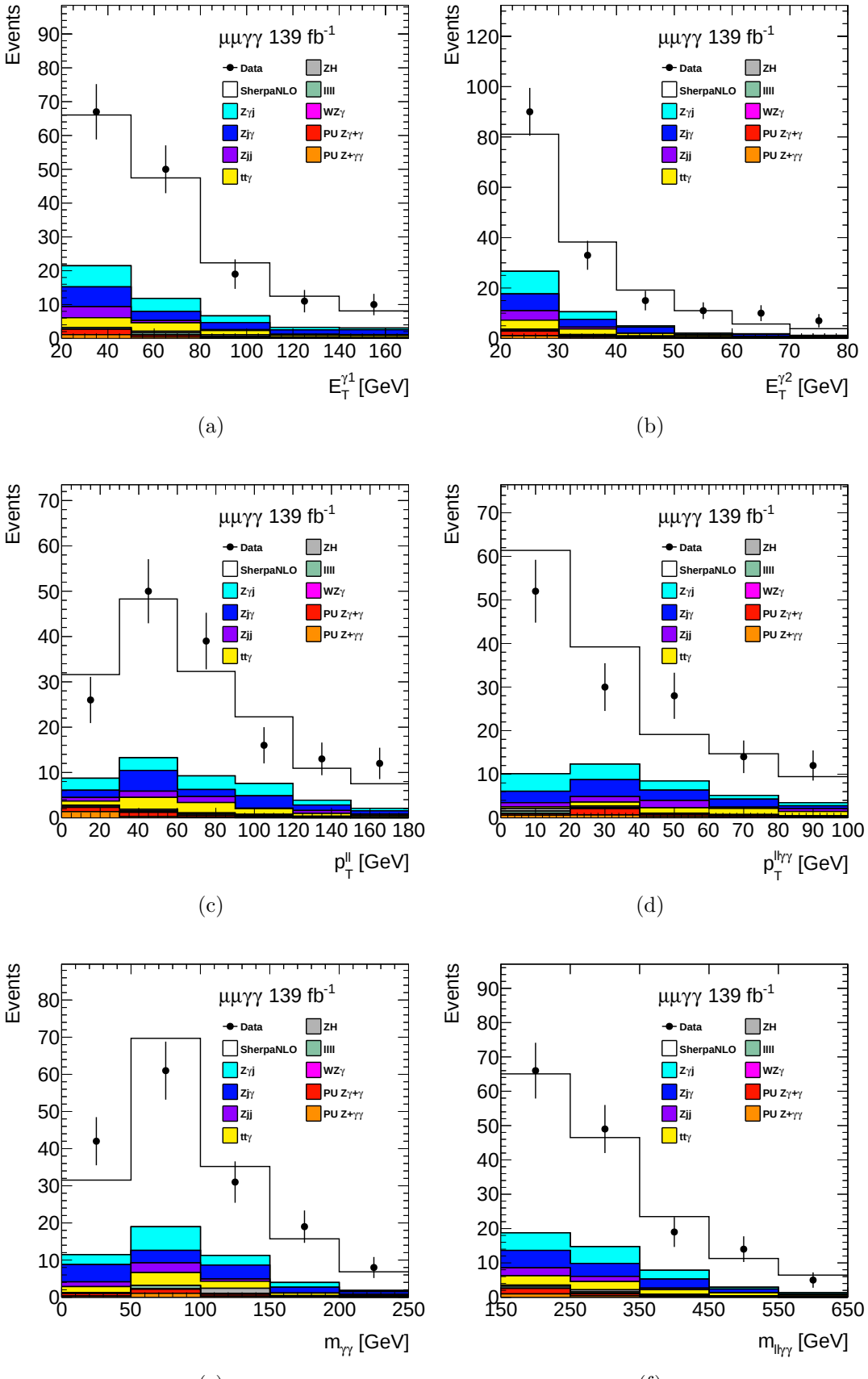


(a) (b) (c) (d) (e) (f)

Figure 6.6: Detector-level distributions for the six measured variables in the $\mu\mu\gamma\gamma$ channel.

## 6.5 Cross-section extraction

### 6.5.1 Variables and binnings

The binning for the differential cross-section measurements is chosen such that there are at least 15 events expected, based on the predictions of the signal MC, in each bin for the electron channel. This is done so that there are a sufficient number of events in each bin to perform the unfolding, and results in four or five bins per variable. The electron channel is considered as it has the lower reconstruction efficiency of the two channels, so it has fewer events to work with. The bin boundaries for each variable are as follows:

- $E_T^{\gamma 1}$: 20, 40, 60, 100, 2000 [GeV]
- $E_T^{\gamma 2}$: 20, 25, 30, 35, 50, 1200 [GeV]
- $p_T^{\ell\ell}$: 0, 30, 60, 120, 1200 [GeV]
- $p_T^{\ell\ell\gamma\gamma}$: 0, 10, 30, 50, 100, 1200 [GeV]
- $m_{\gamma\gamma}$: 0, 50, 75, 100, 150, 3000 [GeV]
- $m_{\ell\ell\gamma\gamma}$: 150, 200, 250, 350, 500, 3000 [GeV]

The uppermost bin edge is set by the range of events in the signal MC. This choice is somewhat arbitrary as most of the events in the highest bins fall towards the lower edge of that bin.

### 6.5.2 Correction factors

The factors used to correct the total detector-level yields to the fiducial level are given in Table 6.8 for both the Sherpa LO and NLO signal samples. $C_{eff}$ is the efficiency correction, which is the ratio of the number of events which pass both

the detector and fiducial selections, to the number of events which pass the fiducial selection. This correction factor corresponds to the reconstruction efficiency of signal events, and is higher in the muon channel due to the higher reconstruction efficiency of muons versus electrons. $C_{fid}$ is the fiducial correction factor, which is the ratio of the number of events which pass both the detector and fiducial selections, to the number of events which pass the detector-level selection. This factor accounts for events which pass the detector-level selection but fail the fiducial-level selection, mainly due to resolution effects. The overall correction factor $C$ is used to correct the detector-level yields to the fiducial-level phase space, and is calculated as $C = C_{eff}/C_{fid}$.

| | Sherpa LO $ee\gamma\gamma$ | Sherpa NLO $ee\gamma\gamma$ | Sherpa LO $\mu\mu\gamma\gamma$ | Sherpa NLO $\mu\mu\gamma\gamma$ |
|---|---|---|---|---|
| $C_{eff}$ | 0.268±0.007 | 0.268±0.003 | 0.375±0.009 | 0.354±0.004 |
| $C_{fid}$ | 0.940±0.030 | 0.939±0.013 | 0.940±0.027 | 0.935±0.011 |
| $C$ | 0.286±0.007 | 0.286±0.003 | 0.399±0.009 | 0.379±0.004 |

Table 6.8: The correction factors calculated from the two signal MCs. The uncertainties of $C_{eff}$ and $C$ are highly correlated due to them having the same denominator.

$C_{eff}$ and $C_{fid}$ are calculated in the differential-measurement bins, which are shown in Appendix B. Also shown in Appendix B are the migration matrices which describe the bin-to-bin migrations when moving from the fiducial-level phase space to the detector-level phase space. Both the correction factors and migration matrices are used as inputs to the unfolding. The migration matrices are very close to being diagonal, which means the effects of migrations between bins is expected to be small.

## 6.6 Theoretical uncertainties

This section details the uncertainties which are considered for the $Z\gamma\gamma$ predictions from Sherpa and their effect on the fiducial cross-section predictions. Specifically, the uncertainties considered are related to the choice of scales, choice of PDF set and the value used for the strong coupling constant, $\alpha_s$.

The uncertainty associated with using a fixed order in the matrix element calculation is estimated by varying the renormalisation ($\mu_R$) and factorisation ($\mu_F$) scales. The scales are varied up and down by factors of 2; all combinations are used except the case where the two scales move in opposite directions (i.e. $0.5 \leq \mu_F/\mu_R \leq 2.0$). The overall uncertainty is taken as the envelope of all the variations, i.e. the largest upwards and largest downwards fluctuation compared to the nominal value. For the integrated fiducial cross-section, this results in an uncertainty of $^{+14\%}_{-10\%}$ for the Sherpa LO prediction and $^{+16\%}_{-9\%}$ for the Sherpa NLO prediction. Typically, the scale uncertainties are expected to decrease as the order of the prediction increases, but this is not the behaviour observed here. However, the discrepancy could be due to the different scale choices between the two different versions of the software used, which suggests that maybe the scale uncertainty for the LO prediction is underestimated. The scale uncertainty for the Sherpa NLO sample is shown as a function of two measured observables in Figure 6.7 for the $ee\gamma\gamma$ channel and is relatively largest in the high-$p_{\mathrm{T}}$ regime.

The nominal PDF set used for the Sherpa NLO signal MC is NNPDF30_nnlo_as_0118, described in Reference [30]. The PDF uncertainty is estimated by looking at the 100 variations which follow the PDF4LHC recommendations [97]. The standard deviation of the mean value from these 100 variations is taken as the PDF uncertainty. The nominal value of $\alpha_s$ used in the PDF sets is 0.118. This value is varied up to 0.119 and down to 0.117, and the average fluctuation between these two variations is taken as the uncertainty. The uncertainties due to the choices of PDF and $\alpha_s$ are added in quadrature and result in an uncertainty of 2% on the integrated fiducial cross-section prediction for the Sherpa LO sample and 1% for the Sherpa NLO sample. The combined PDF and $\alpha_s$ uncertainties are also shown in Figure 6.7 for the electron channel.

The statistical uncertainty due to the number of MC events is also considered. For the integrated fiducial cross-section prediction, the statistical uncertainty is 1.4% for the Sherpa LO sample and 0.4% for the Sherpa NLO sample.

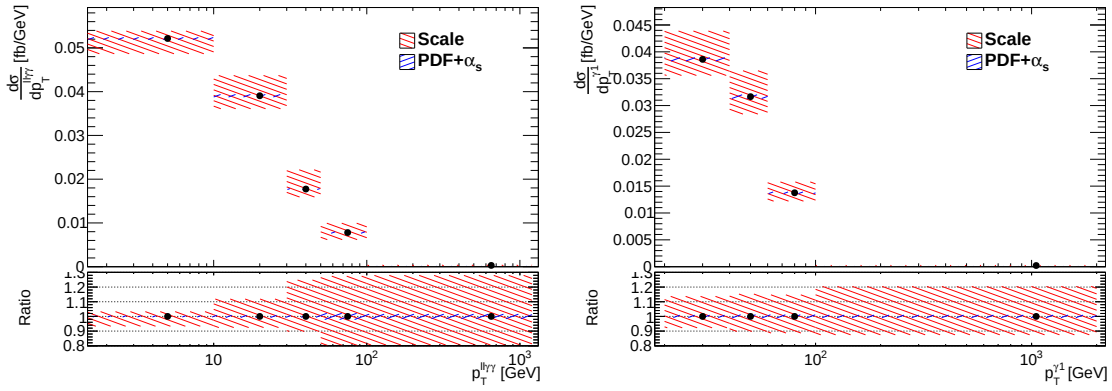


(a) (b)

Figure 6.7: The $ee\gamma\gamma$ differential fiducial cross-sections as a function of $p_T^{\ell\ell\gamma\gamma}$ and $p_T^{\gamma 1}$ as predicted by the Sherpa 2.2.10 NLO signal MC. The red uncertainty band represents the scale uncertainty and the blue uncertainty band represents the combined PDF and $\alpha_s$ uncertainty on the fiducial cross-section in each bin. The bottom panel shows the ratio of the uncertainties to the predicted cross-section value in each bin.

## 6.7 Results

### 6.7.1 Integrated fiducial cross-section measurements

The numbers of signal events in data, in each channel, are used to calculate the cross-sections within the fiducial acceptance using the correction factors calculated from the signal MC and the measured integrated luminosity, as described in Section 4.4. The measured fiducial cross-sections in the two channels are:

$$\sigma_{fid}^{Z(\to ee)\gamma\gamma} = 2.65 \pm 0.31(\text{stat}) \pm 0.23(\text{syst}) \pm 0.05(\text{lumi}) \text{ fb}\,,$$

$$\sigma_{fid}^{Z(\to \mu\mu)\gamma\gamma} = 2.29 \pm 0.25(\text{stat}) \pm 0.20(\text{syst}) \pm 0.04(\text{lumi}) \text{ fb}\,.$$

The measured cross-sections are consistent within uncertainties between the two channels which is expected due to lepton universality in $Z$ decays. The systematic uncertainty breakdown in each channel is given in Table 6.9. The dominant sources of uncertainty are the statistical uncertainty of the data, and the systematic uncertainty related to the fake photon background.

| Source | Relative uncertainty [%] | |
|---|---|---|
| | $e^+e^-\gamma\gamma$ | $\mu^+\mu^-\gamma\gamma$ |
| Photon identification efficiency* | 2.5 | 2.6 |
| Photon isolation efficiency* | 2.0 | 2.0 |
| Electron-photon energy resolution* | 0.2 | 0.1 |
| Electron-photon energy scale* | 0.8 | 0.6 |
| Electron reconstruction | 2.0 | - |
| Muon reconstruction | - | 0.7 |
| Pile-up reweighting* | 2.8 | 2.9 |
| Monte Carlo signal statistics | 1.1 | 1.0 |
| Fake photon background* | 7.0 | 7.1 |
| Other backgrounds* | 1.4 | 1.7 |
| Data statistical uncertainty | 11.5 | 10.9 |
| Systematic uncertainty | 8.7 | 8.6 |
| Integrated luminosity uncertainty | 1.7 | 1.7 |
| Total uncertainty | 14.5 | 14.0 |

Table 6.9: Relative systematic uncertainties on the integrated $Z(\to \ell\ell)\gamma\gamma$ fiducial cross-section in each channel using 139 fb$^{-1}$of data. Uncertainties marked with a * are fully or partially correlated between the two channels.

The cross-section measurements in the two channels are combined according to the procedure outlined in Section 4.4.2.1. The resulting integrated fiducial $Z(\to \ell\ell)\gamma\gamma$ cross-section is measured to be

$$\sigma_{fid}^{Z(\to\ell\ell)\gamma\gamma} = 2.45 \pm 0.20(\text{stat}) \pm 0.21(\text{syst}) \pm 0.04(\text{lumi})\ \text{fb}\,.$$

The integrated cross-section is measured with a precision of 12% and is compared to predictions (detailed in Section 1.7.2) from Sherpa, at NLO and LO, in Figure 6.8. The measured value is 6% higher than the NLO prediction and 17% higher than the LO prediction. The agreement of the LO prediction with the measured value is within $1.4\sigma$. The NLO prediction agrees marginally better, within $0.5\sigma$.

### 6.7.2 Differential cross-section measurements

The data are binned as described in Section 6.5.1. The background estimate is subtracted in each bin and the resulting yields are unfolded to the fiducial volume,

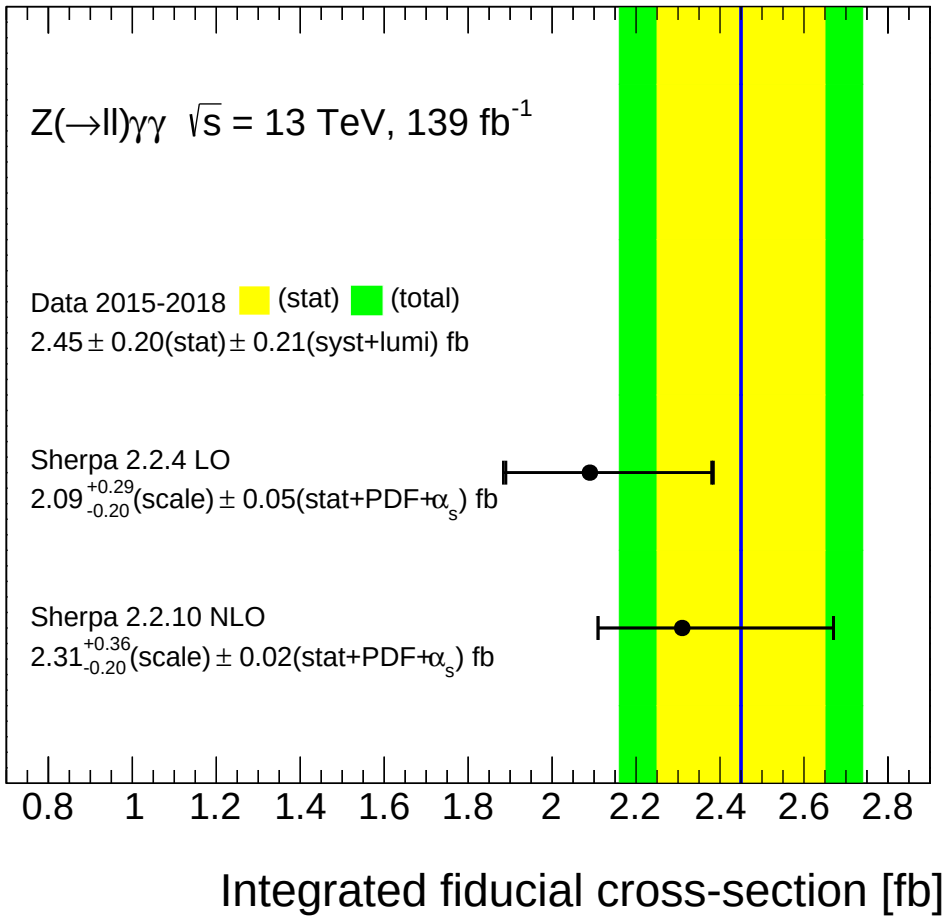


Figure 6.8: The measured integrated fiducial $\ell\ell\gamma\gamma$ cross-section, compared to predictions from Sherpa.

separately in each channel. The $Z(\to ee)\gamma\gamma$ and $Z(\to \mu\mu)\gamma\gamma$ cross-section measurements in each bin are combined, accounting for correlated uncertainties, using the procedure outlined in Section 4.4.2.1. The resulting distributions are shown and compared to the predictions from Sherpa in Figures 6.9, 6.10 and 6.11. In these figures the final bin in each distribution is truncated for aesthetic purposes, but still contains all the data up to the bin edge defined in Section 6.5.1. The data in this bin are normalised to the displayed bin width and the data point is plotted at the average value of the data in that bin before unfolding.

The precision of the data ranges between 20-30% in each bin of the distributions, dominated by the statistical uncertainty. Within this precision, the predictions

provide a reasonable description of the data. The normalisation difference again results in a slightly better agreement with the NLO prediction, but the shape is similar for both predictions.

The transverse energy distributions displayed in Figure 6.9 are reasonably well described by the predictions. The $p_T^{\ell\ell}$ distribution in Figure 6.10(a) describes the $Z$ which is typically recoiling against the two photons. This distribution is therefore sculpted by the transverse momentum of the two photons, which results in the peak around 40 GeV. Analogous to the $p_T^{\ell\ell\gamma}$ distribution in the $Z\gamma$ analysis, the $p_T^{\ell\ell\gamma\gamma}$ distribution probes the QCD modelling of the predictions. The comparison is shown in Figure 6.10(b) where it is seen that the agreement is quite poor in the low and high $p_{\mathrm{T}}$ regions, which exposes weaknesses of the QCD modelling by Sherpa in these regions. The $m_{\gamma\gamma}$ distribution is shown in Figure 6.11(a) and is reasonably well described by the predictions. The $m_{\ell\ell\gamma\gamma}$ distribution provides a measure of the hard scale of the system. The measurement is shown in Figure 6.11(b) and is described well by the predictions. This distribution shows that this process starts to be probed up to the TeV scale which is promising for future studies involving anomalous couplings, as the sensitivity typically grows with the scale of the system.

### 6.7.3 Summary and outlook

The results presented in this chapter are from the first study of the $Z(\to \ell\ell)\gamma\gamma + X$ process in isolation. The leptonic decay channels of the $Z$ are used which, despite having lower branching fractions than the $\nu\bar{\nu}$ or $q\bar{q}$ channels, result in clean signals that do not contribute significant uncertainties to the final measurements. The dominant uncertainties arise due to the limited data statistics and the uncertainty of the fake photon background estimation. The measurements are performed in a fiducial phase space which is dominated by the ISR production of the two photons. Compared to the most recent $\ell\ell\gamma\gamma$ measurement at $\sqrt{s} = 13$ TeV [49], the precision is improved by 4% despite using a more restricted region of phase space which does not include FSR photons. The measured cross-sections are described well by MC

predictions at NLO and LO, although the limited precision of the measurement does not allow for the two predictions to be well distinguished. However, the differential cross-sections do reveal some limitations in the QCD modelling of the calculations.

Now that the feasibility to measure the $Z(\to \ell\ell)\gamma\gamma$ process has been demonstrated, further studies can be performed to expand the scope of the research with this process. More specifically, this involves constraining limits on anomalous quartic couplings. As the measurements presented here are statistically limited, no further improvements are expected using solely the Run-2 dataset. However, as the results are fully unfolded to a well-defined fiducial region, this means the results are readily available to be compared to any new SM predictions if and when they become available. The addition of the LHC Run-3 dataset will result in more precise measurements that could be used to test the SM predictions more rigorously.

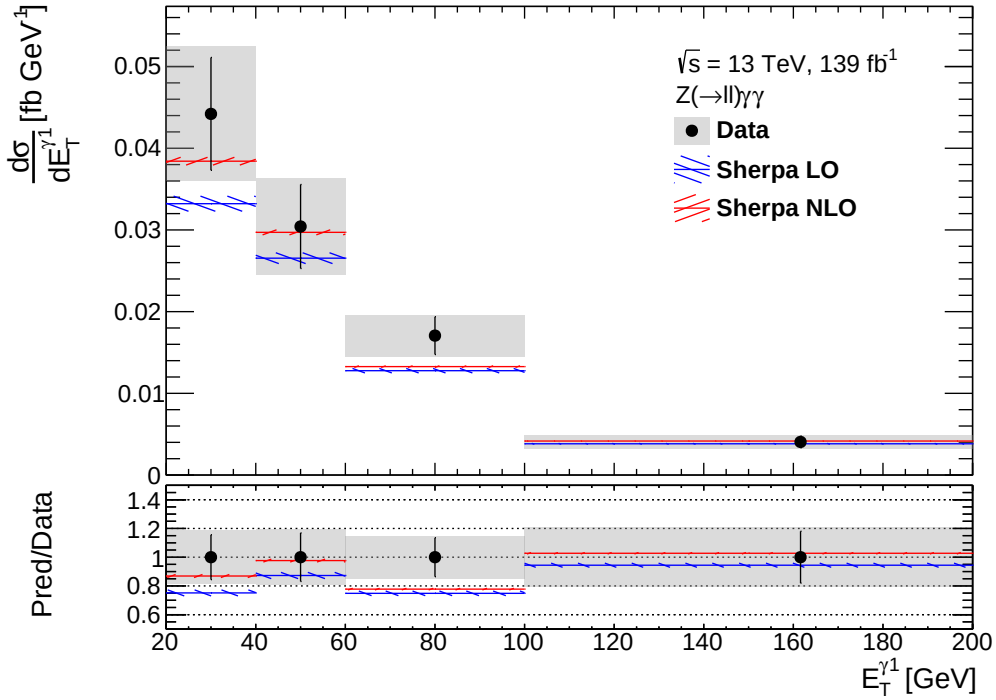


(a)

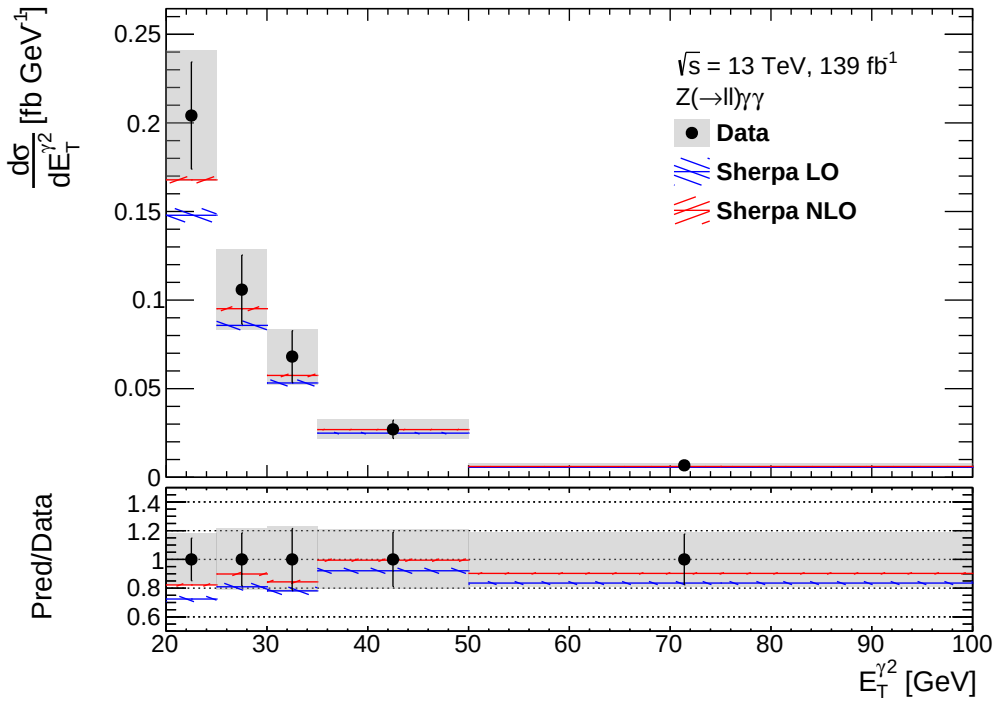


(b)

Figure 6.9: The differential fiducial cross-section measurements as a function of (a) the leading photon transverse energy (b) the subleading photon transverse energy. The error bars for each data point represent the statistical uncertainty, whereas the grey error bands also include the systematic uncertainties. The uncertainties shown for the predictions from Sherpa are statistical only.

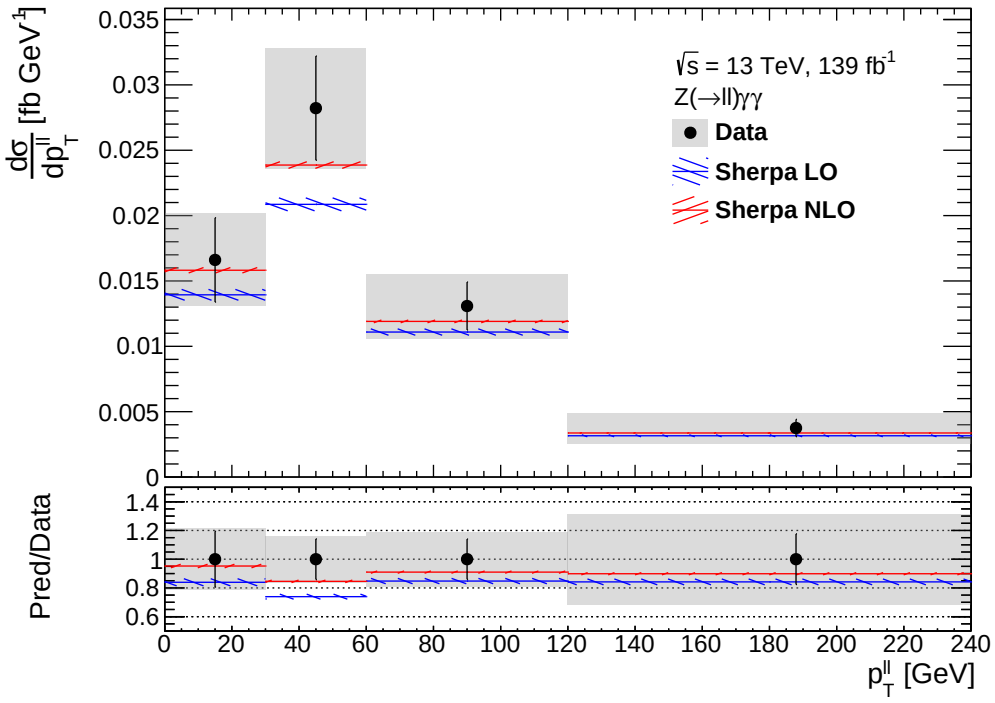


(a)

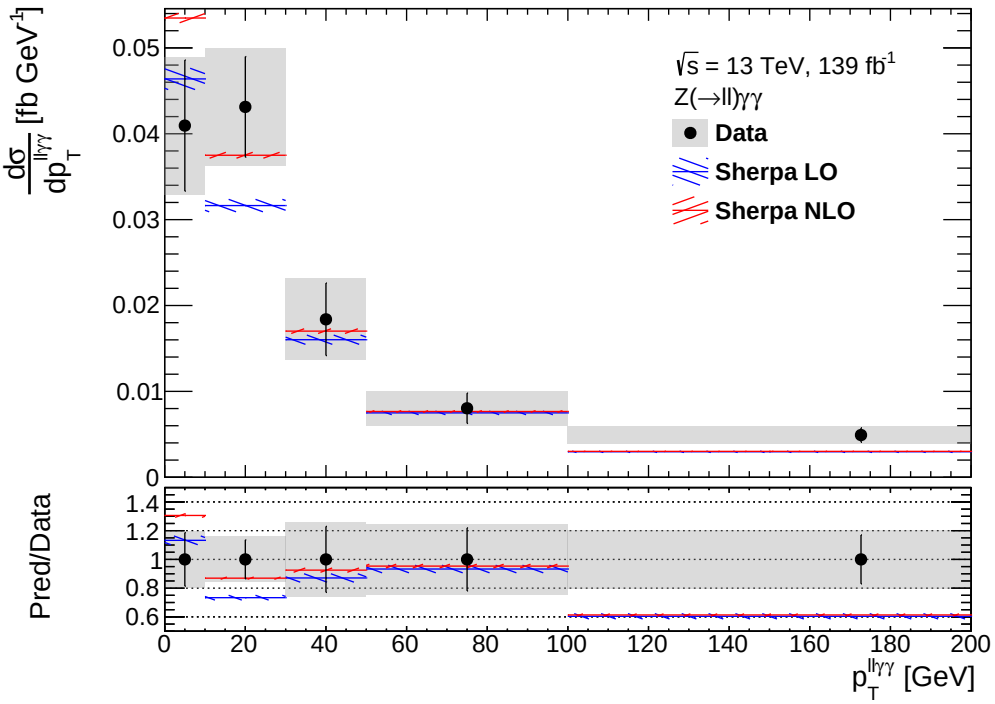


(b)

Figure 6.10: The differential fiducial cross-section measurements as a function of (a) the transverse momentum of the dilepton system (b) the transverse momentum of the four-body system. The error bars for each data point represent the statistical uncertainty, whereas the grey error bands also include the systematic uncertainties. The uncertainties shown for the predictions from Sherpa are statistical only.

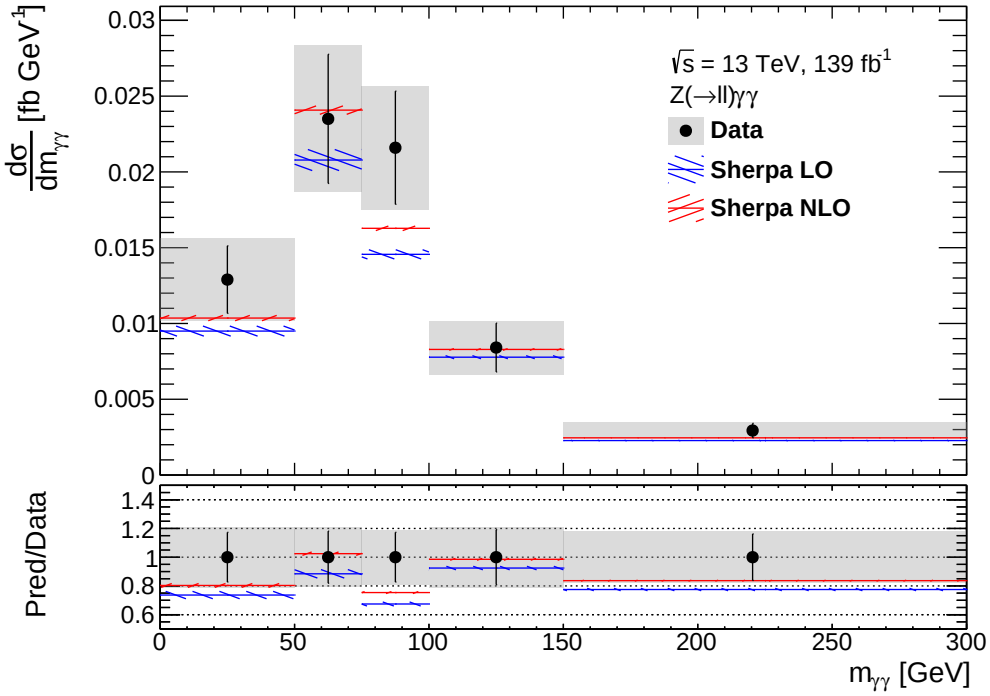


(a)

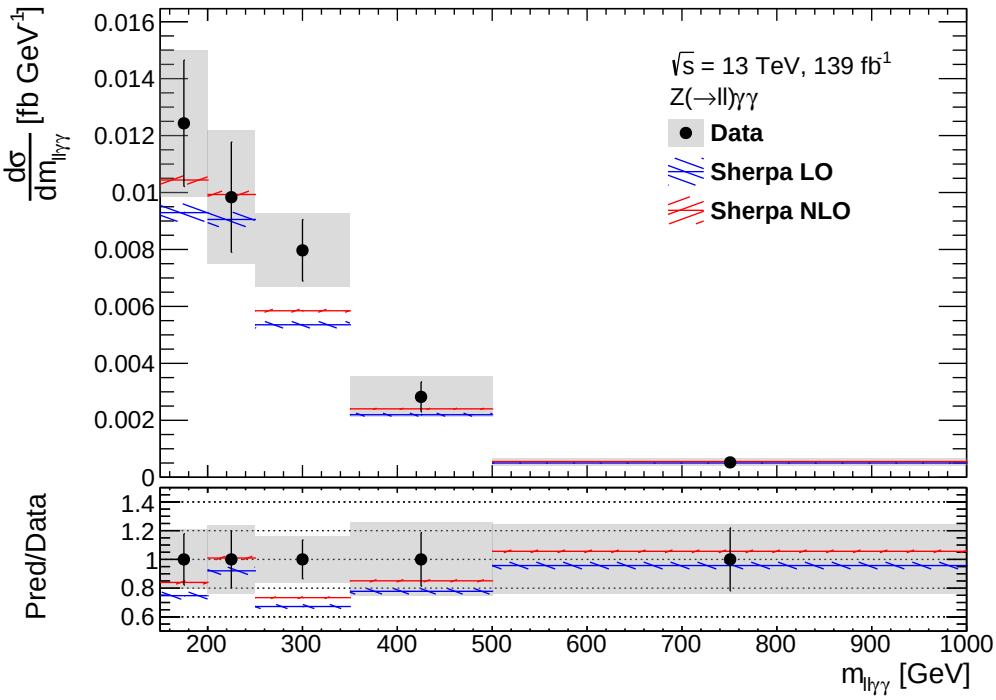


(b)

Figure 6.11: The differential fiducial cross-section measurements as a function of (a) the invariant mass of the diphoton system (b) the invariant mass of the four-body system. The error bars for each data point represent the statistical uncertainty, whereas the grey error bands also include the systematic uncertainties. The uncertainties shown for the predictions from Sherpa are statistical only.

# Conclusions

Run-2 of the LHC provided the highest centre-of-mass energy and largest number of proton-proton collisions to date. A highly efficient operation of the ATLAS detector over the period 2015-2018 allowed the collection of a huge dataset spanning a wide scope of physics signatures, corresponding to an integrated luminosity of 139 $\text{fb}^{-1}$. Due to the high rate of collisions during this period, the detector was subject to a significant amount of radiation, often exceeding the expectation set by the design values. The monitoring of the detector condition and recorded data quality was therefore paramount in achieving an optimal performance. Two examples of tools implemented for this purpose were presented in Chapter 3, for the ATLAS semiconductor tracker. The first is used to investigate defects which are identified in the calibration procedure. The second is primarily used to identify the cause of inefficient modules and whether this can be attributed to radiation damage. Both displays were part of a larger programme in the SCT operations team to ensure excellent data quality, and this programme will be continued into Run-3 of the LHC.

The vast dataset recorded by the ATLAS detector in Run-2 has allowed the measurements of many processes predicted by the SM. For processes with relatively

large cross-sections, the dataset provides the possibility for precision measurement, which can be used to rigorously test the most accurate predictions. This has positive ramifications for improving the calculations and also potentially identifying contributions from new physics. An example of such a measurement, for the process $pp \to Z(\to \ell\ell)\gamma + X$, was presented in Chapter 5. For processes with relatively low cross-sections, the large dataset allows some of these to be measured for the first time. The observation of such processes further demonstrates the predictability of the SM and can be used to test calculations and constrain new physics. The $pp \to Z(\to \ell\ell)\gamma\gamma + X$ analysis presented in Chapter 6 is an example of such a measurement.

The $Z(\to \ell\ell)\gamma + X$ analysis constitutes the first measurements of this process in isolation and is also the first for this process at $\sqrt{s} = 13$ TeV. The integrated fiducial $Z(\to \ell\ell)\gamma$ cross-section was measured to a total precision of 3%, resulting in the most precise measurement of this process to date, and of similar precision to the available theoretical predictions. The precision highlights the importance of NNLO QCD corrections to the cross-section calculation. The fiducial cross-section is also measured differentially which provides further sensitivity to NNLO QCD as well as to NLO EW corrections. These measurements provide a benchmark for tests of future predictions, which are expected to have even higher accuracy than those currently available.

The $Z(\to \ell\ell)\gamma\gamma + X$ process was measured in isolation for the first time, and also constitutes the first measurement of this process with the ATLAS detector at $\sqrt{s} = 13$ TeV. The first differential cross-section measurements for this process were also presented. The integrated fiducial $Z(\to \ell\ell)\gamma\gamma$ cross-section was measured to a precision of 12%, with approximately equal contributions from statistical and systematic uncertainties. The largest systematic uncertainty arises from the estimation of the fake photon backgrounds, which was the most challenging aspect of the analysis. The measurements are used to test predictions up to NLO in QCD. They agree within uncertainties, however the precision of future measurements will need to be improved in order to test higher order corrections rigorously.

Both of these processes have further scope to be studied using the Run-2 dataset, particularly with respect to anomalous couplings. As the $Z\gamma$ and $Z\gamma\gamma$ processes are measured in the ISR-dominated phase space, the limits set on aTGCs and aQGCs are expected to be competitive with previous limits. Run-3 of the LHC, scheduled to start in 2022, will provide an additional, slightly larger, dataset and at a slightly higher centre-of-mass energy. The precision of measurements of these processes can be improved by a corresponding factor, resulting in a more thorough test of the predictions and stronger constraints on anomalous couplings. Looking even further ahead to the HL-LHC era [52], a predicted dataset of around 3000 $\text{fb}^{-1}$ could allow for more scrutiny of the $Z\gamma$ process, for example double-differential cross-section measurements. For the $Z\gamma\gamma$ process, precision measurements could be performed with this dataset. These analyses will form part of a wider programme of electroweak measurements at the HL-LHC, which will continue to test the Standard Model and search for new physics.

# REFERENCES


[1] M. Thomson, *Modern Particle Physics*. Cambridge University Press, 2013.

[2] Particle Data Group, "Review of Particle Physics", *Progress of Theoretical and Experimental Physics 2020*, 083C01, 2020.

[3] ATLAS Collaboration, "Observation of a new particle in the search for the Standard Model Higgs boson with the ATLAS detector at the LHC", *Physics Letters B*, vol. 716, p. 1–29, 2012.

[4] CMS Collaboration, "Observation of a new boson at a mass of 125 GeV with the CMS experiment at the LHC", *Physics Letters B*, vol. 716, p. 30–61, 2012.

[5] Dissertori, G, "The Determination of the Strong Coupling Constant", 2015. A contribution to: The Standard Theory up to the Higgs discovery - 60 years of CERN, L. Maiani and G. Rolandi, eds.

[6] H.-W. Lin, E. R. Nocera, F. Olness, K. Orginos, J. Rojo, A. Accardi, C. Alexandrou, A. Bacchetta, G. Bozzi, J.-W. Chen, *et al.*, "Parton distributions and lattice QCD calculations: A community white paper", *Progress in Particle and Nuclear Physics*, vol. 100, p. 107–160, 2018.

[7] A. Deur, S. J. Brodsky, and G. F. de Téramond, "The QCD running coupling", *Progress in Particle and Nuclear Physics*, vol. 90, p. 1–74, 2016.

[8] R. D. Ball, V. Bertone, S. Carrazza, C. S. Deans, L. Del Debbio, S. Forte, A. Guffanti, N. P. Hartland, J. I. Latorre, *et al.*, "Parton distributions for the LHC run II", *Journal of High Energy Physics*, 04, 040, 2015.

[9] Y. L. Dokshitzer, "Calculation of the Structure Functions for Deep Inelastic Scattering and $e^+$ $e^-$ Annihilation by Perturbation Theory in Quantum Chro-

modynamics", *Soviet Journal of Experimental and Theoretical Physics*, vol. 46, p. 641–653, 1977.

[10] V. N. Gribov and L. N. Lipatov, "Deep inelastic ep scattering in perturbation theory", *Soviet Journal of Nuclear Physics*, vol. 15, p. 438–450, 1972.

[11] G. Altarelli and G. Parisi, "Asymptotic Freedom in Parton Language", *Nuclear Physics B*, vol. 126, p. 298–318, 1977.

[12] S. Höche, "Introduction to parton-shower event generators", *Theoretical Advanced Study Institute in Elementary Particle Physics: Journeys Through the Precision Frontier: Amplitudes for Colliders*, p. 235–295, 2015. arXiv: 1411.4085.

[13] D. Amati and G. Veneziano, "Preconfinement as a Property of Perturbative QCD", *Physics Letters B*, vol. 83, p. 87–92, 1979.

[14] B. Andersson, G. Gustafson, G. Ingelman, and T. Sjostrand, "Parton Fragmentation and String Dynamics", *Physics Reports*, vol. 97, p. 31–145, 1983.

[15] S. Agostinelli *et al.*, "GEANT4: A Simulation toolkit", *Nuclear Instruments and Methods in Physics Research Section A*, vol. 506, p. 250–303, 2003.

[16] E. Bothmann, G. Singh Chahal, S. Höche, J. Krause, F. Krauss, S. Kuttimalai, S. Liebschner, D. Napoletano, M. Schönherr, H. Schulz, *et al.*, "Event generation with Sherpa 2.2", *SciPost Physics*, 7, 034, 2019.

[17] J. Alwall, R. Frederix, S. Frixione, V. Hirschi, F. Maltoni, O. Mattelaer, H.-S. Shao, T. Stelzer, P. Torrielli, and M. Zaro, "The automated computation of tree-level and next-to-leading order differential cross sections, and their matching to parton shower simulations", *Journal of High Energy Physics*, 07, 079, 2014.

[18] S. Alioli, P. Nason, C. Oleari, and E. Re, "A general framework for implementing NLO calculations in shower Monte Carlo programs: the POWHEG BOX", *Journal of High Energy Physics*, 06, 043, 2010.

[19] S. Schumann and F. Krauss, "A parton shower algorithm based on Catani-Seymour dipole factorisation", *Journal of High Energy Physics*, 03, 038, 2008.

[20] T. Sjöstrand, S. Mrenna, and P. Skands, "A brief introduction to PYTHIA 8.1", *Computer Physics Communications*, vol. 178, p. 852–867, 2008.

[21] M. Grazzini, S. Kallweit, and M. Wiesemann, "Fully differential NNLO computations with MATRIX", *The European Physical Journal C*, vol. 78, 537, 2018.

[22] J. Campbell and T. Neumann, "Precision phenomenology with MCFM", *Journal of High Energy Physics*, 12, 034, 2019.

[23] A. Denner, S. Dittmaier, M. Hecht, and C. Pasold, "NLO QCD and electroweak corrections to $Z+\gamma$ production with leptonic Z-boson decays", *Journal of High Energy Physics*, 02, 057, 2016.

[24] ATLAS Collaboration, "Standard Model Summary Plots March 2021", *https://atlas.web.cern.ch/Atlas/GROUPS/PHYSICS/PUBNOTES/ATL-PHYS-PUB-2021-005*, 2021. Accessed 27/10/2021.

[25] C. Degrande, N. Greiner, W. Kilian, O. Mattelaer, H. Mebane, T. Stelzer, S. Willenbrock, and C. Zhang, "Effective field theory: A modern approach to anomalous couplings", *Annals of Physics*, vol. 335, p. 21–32, 2013.

[26] ATLAS Collaboration, "Measurement of the $Z \to (\ell^+\ell^-)\gamma$ production cross-section in $pp$ collisions at $\sqrt{s} = 13$ TeV with the ATLAS detector", *Journal of High Energy Physics*, 03, 054, 2020.

[27] ATLAS Collaboration, "Evidence for electroweak production of two jets in association with a $Z\gamma$ pair in $pp$ collisions at $\sqrt{s} = 13$ TeV with the ATLAS detector", *Physics Letters B*, vol. 803, 135341, 2020.

[28] CMS Collaboration, "Measurement of the cross section for electroweak production of a Z boson, a photon and two jets in proton-proton collisions at $\sqrt{s} = 13$ TeV and constraints on anomalous quartic couplings", *Journal of High Energy Physics*, 06, 076, 2020.

[29] CMS Collaboration, "Measurement of the electroweak production of Z$\gamma$ and two jets in proton-proton collisions at $\sqrt{s} = 13$ TeV and constraints on anomalous quartic gauge couplings", *Physical Review D*, vol. 104, 072001, 2021.

[30] R. D. Ball, V. Bertone, S. Carrazza, C. S. Deans, L. Del Debbio, S. Forte, A. Guffanti, N. P. Hartland, J. I. Latorre, *et al.*, "Parton distributions for the LHC run II", *Journal of High Energy Physics*, 04, 040, 2015.

[31] S. Dulat, T.-J. Hou, J. Gao, M. Guzzi, J. Huston, P. Nadolsky, J. Pumplin, C. Schmidt, D. Stump, and C.-P. Yuan, "New parton distribution functions from a global analysis of quantum chromodynamics", *Physical Review D*, vol. 93, 033006, 2016.

[32] W. Hollik and C. Meier, "Electroweak corrections to $\gamma Z$ production at hadron colliders", *Physics Letters B*, vol. 590, p. 69–75, 2004.

[33] E. Accomando, A. Denner, and C. Meier, "Electroweak corrections to $W\gamma$ and $Z\gamma$ production at the LHC", *The European Physical Journal C*, vol. 47, p. 125–146, 2006.

[34] L3 Collaboration, "Study of the $e^+e^- \to Z\gamma$ process at LEP and limits on triple neutral-gauge-boson couplings", *Physics Letters B*, vol. 597, p. 119–130, 2004.

[35] DELPHI Collaboration, "Study of triple-gauge-boson couplings $ZZZ$, $ZZ\gamma$ and $Z\gamma\gamma$ at LEP", *The European Physical Journal C*, vol. 51, p. 525–542, 2007.

[36] OPAL Collaboration, "Search for trilinear neutral gauge boson couplings in $Z\gamma$ production at $\sqrt{s} = 189$ GeV at LEP", *The European Physical Journal C*, vol. 17, p. 553–566, 2000.

[37] D0 Collaboration, "$Z\gamma$ production and limits on anomalous $ZZ\gamma$ and $Z\gamma\gamma$ couplings in $p\bar{p}$ collisions at $\sqrt{s} = 1.96$ TeV", *Physical Review D*, vol. 85, 052001, 2012.

[38] D0 Collaboration, "Measurement of the $Z\gamma \to \nu\bar{\nu}\gamma$ Cross Section and Limits on Anomalous $ZZ\gamma$ and $Z\gamma\gamma$ Couplings in $p\bar{p}$ Collisions at $\sqrt{s} = 1.96$ TeV", *Physical Review Letters*, vol. 102, 201802, 2009.

[39] CDF Collaboration, "Limits on Anomalous Trilinear Gauge Couplings in $Z\gamma$ Events from $p\bar{p}$ Collisions at $\sqrt{s} = 1.96$ TeV", *Physical Review Letters*, vol. 107, 051802, 2011.

[40] ATLAS Collaboration, "Measurement of $W\gamma$ and $Z\gamma$ production cross sections in $pp$ collisions at $\sqrt{s} = 7$ TeV and limits on anomalous triple gauge couplings with the ATLAS detector", *Physics Letters B*, 717, p. 49–69, 2012.

[41] ATLAS Collaboration, "Measurements of $Z\gamma$ and $Z\gamma\gamma$ production in $pp$ collisions at $\sqrt{s} = 8$ TeV with the ATLAS detector", *Physical Review D*, vol. 93, 112002, 2016.

[42] T. Gleisberg, S. Hoeche, F. Krauss, M. Schonherr, S. Schumann, F. Siegert, and J. Winter, "Event generation with SHERPA 1.1", *Journal of High Energy Physics*, 02, 007, 2009.

[43] J. M. Campbell, R. K. Ellis, W. Giele, and C. Williams, "MCFM v7.0: A Monte Carlo for FeMtobarn processes at Hadron Colliders, Users Guide", 2015. http://mcfm.fnal.gov/mcfm.pdf.

[44] M. Grazzini, S. Kallweit, and D. Rathlev, "$W\gamma$ and $Z\gamma$ production at the LHC in NNLO QCD", *Journal of High Energy Physics*, 07, 085, 2015.

[45] CMS Collaboration, "Measurement of the production cross section for $Z\gamma \to \nu\bar{\nu}\gamma$ in $pp$ collisions at $\sqrt{s} = 7$ TeV and limits on $ZZ\gamma$ and $Z\gamma\gamma$ triple gauge boson couplings", *Journal of High Energy Physics*, 10, 164, 2013.

[46] CMS Collaboration, "Measurement of the $W\gamma$ and $Z\gamma$ inclusive cross sections in $pp$ collisions at $\sqrt{s} = 7$ TeV and limits on anomalous triple gauge boson couplings", *Physical Review D*, vol. 89, 092005, 2014.

[47] CMS Collaboration, "Measurement of the $Z\gamma$ production cross-section in $pp$ collisions at 8 TeV and search for anomalous triple gauge boson couplings", *Journal of High Energy Physics*, 04, 164, 2015.

[48] CMS Collaboration, "Measurements of the $pp \to W\gamma\gamma$ and $pp \to Z\gamma$ cross sections and limits on anomalous quartic gauge couplings at $\sqrt{s} = 8$ TeV", *Journal of High Energy Physics*, 10, 072, 2017.

[49] CMS Collaboration, "Measurements of the $pp \to W^{\pm}\gamma\gamma$ and $pp \to Z\gamma\gamma$ cross sections at $\sqrt{s} = 13$ TeV and limits on anomalous quartic gauge couplings", 2021. arXiv: 2105.12780.

[50] O. S. Brüning, P. Collier, P. Lebrun, S. Myers, R. Ostojic, J. Poole, and P. Proudlock, *LHC Design Report*. CERN Yellow Reports: Monographs, Geneva: CERN, 2004.

[51] STFC, "CERN Accelerator Complex", *https://stfc.ukri.org/research/particle-physics-and-particle-astrophysics/large-hadron-collider/cern-accelerator-complex/*. Accessed 16/04/2021.

[52] I. Bejar Alonso and L. Rossi, "HiLumi LHC Technical Design Report: Deliverable: D1.10", CERN-ACC-2015-0140, 2015. URL: https://cds.cern.ch/record/2069130.

[53] ATLAS Collaboration, "ATLAS Luminosity Public Results Run 2", *https://twiki.cern.ch/twiki/bin/view/AtlasPublic/LuminosityPublicResultsRun2*. Accessed 27/01/2021.

[54] ATLAS Collaboration, "The ATLAS Experiment at the CERN Large Hadron Collider", *Journal of Instrumentation*, vol. 3, S08003, 2008.

[55] ATLAS Collaboration, "ATLAS Inner Detector: Technical Design Report, 2", CERN-LHCC-97-017, Geneva, 1997. URL: https://cds.cern.ch/record/331064.

[56] ATLAS Collaboration, "Performance of the ATLAS track reconstruction algorithms in dense environments in LHC Run 2", *The European Physical Journal C*, vol. 77, 673, 2017.

[57] ATLAS Collaboration, "ATLAS Insertable B-Layer Technical Design Report", CERN-LHCC-2010-013, 2010. URL: https://cds.cern.ch/record/1291633.

[58] ATLAS Collaboration, "ATLAS Liquid-Argon Calorimeter: Technical Design Report", CERN-LHCC-96-041, Geneva, 1996. URL: https://cds.cern.ch/record/331061.

[59] ATLAS Collaboration, "Measurement of the photon identification efficiencies with the ATLAS detector using LHC Run 2 data collected in 2015 and 2016", *The European Physical Journal C*, vol. 79, 205, 2019.

[60] ATLAS Collaboration, "ATLAS Tile Calorimeter: Technical Design Report", CERN-LHCC-96-042, Geneva, 1996. URL: https://cds.cern.ch/record/331062.

[61] ATLAS Collaboration, "ATLAS Muon Spectrometer: Technical Design Report", CERN-LHCC-97-022, Geneva, 1997. URL: https://cds.cern.ch/record/331068.

[62] ATLAS Collaboration, "ATLAS Forward Detectors for Measurement of Elastic Scattering and Luminosity", CERN-LHCC-2008-004, Geneva, 2008. URL: https://cds.cern.ch/record/1095847.

[63] ATLAS Collaboration, "Luminosity determination in $pp$ collisions at $\sqrt{s}$ = 13 TeV using the ATLAS detector at the LHC", ATLAS-CONF-2019-021, CERN, Geneva, 2019. URL: https://cds.cern.ch/record/2677054.

[64] ATLAS Collaboration, "ATLAS High-Level Trigger, Data-Acquisition and Controls: Technical Design Report", CERN-LHCC-2003-022, Geneva, 2003. URL: http://cds.cern.ch/record/616089.

[65] ATLAS Collaboration, "ATLAS Level-1 Trigger: Technical Design Report", CERN-LHCC-98-014, Geneva, 1998. URL: https://cds.cern.ch/record/381429.

[66] "Worldwide LHC Computing Grid", *https://wlcg-public.web.cern.ch/*. Accessed 12/10/2021.

[67] ATLAS Collaboration, "Operation and performance of the ATLAS semiconductor tracker", *Journal of Instrumentation*, vol. 9, P08009, 2014.

[68] ATLAS Collaboration, "Operation and performance of the ATLAS semiconductor tracker in LHC Run 2", 2021. arXiv: 2109.02591.

[69] SCT Collaboration, "SCT Photo gallery", *https://atlas.web.cern.ch/Atlas/GROUPS/INNER_DETECTOR/SCT/gallery/*. Accessed 27/04/2021.

[70] A. Valassi, M. Clemencic, D. Dykstra, M. Frank, D. Front, G. Govi, A. Kalkhof, A. Loth, M. Nowak, W. Pokorski, A. Salnikov, S. Schmidt, R. Trentadue, M. Wache, and Z. Xie, "LCG Persistency Framework (CORAL, COOL, POOL): Status and Outlook in 2012", *Journal of Physics: Conference Series*, vol. 331, 042043, 2011.

[71] A. Abdesselam *et al.*, "The Data Acquisition and calibration system for the ATLAS semiconductor tracker", *Journal of Instrumentation*, vol. 3, P01003, 2008.

[72] ATLAS Collaboration, "Performance of electron and photon triggers in ATLAS during LHC Run 2", *The European Physical Journal C*, vol. 80, 47, 2020.

[73] ATLAS Collaboration, "Electron efficiency measurements with the ATLAS detector using 2012 LHC proton–proton collision data", *The European Physical Journal C*, vol. 77, 195, 2017.

[74] ATLAS Collaboration, "Performance of the ATLAS muon triggers in Run 2", *Journal Of Instrumentation*, vol. 15, P09015, 2020.

[75] R. Frühwirth, "Application of Kalman filtering to track and vertex fitting", *Nuclear Instruments and Methods in Physics Research Section A*, vol. 262, p. 444–450, 1987.

[76] T. Cornelissen, M. Elsing, I. Gavrilenko, W. Liebig, E. Moyse, and A. Salzburger, "The new ATLAS track reconstruction (NEWT)", *Journal of Physics: Conference Series*, vol. 119, 032014, 2008.

[77] ATLAS Collaboration, "Performance of the ATLAS Inner Detector Track and Vertex Reconstruction in the High Pile-Up LHC Environment", 2012. URL: https://cds.cern.ch/record/1435196.

[78] ATLAS Collaboration, "Electron and photon performance measurements with the ATLAS detector using the 2015–2017 LHC proton-proton collision data", *Journal of Instrumentation*, vol. 14, P12006, 2019.

[79] E. Hines, "Performance of Particle Identification with the ATLAS Transition Radiation Tracker", in *Meeting of the APS Division of Particles and Fields*, 2011. arXiv: 1109.5925.

[80] ATLAS Collaboration, "Electron and photon energy calibration with the ATLAS detector using 2015–2016 LHC proton-proton collision data", *Journal of Instrumentation*, vol. 14, P03017, 2019.

[81] ATLAS Collaboration, "Electron reconstruction and identification in the ATLAS experiment using the 2015 and 2016 LHC proton–proton collision data at $\sqrt{s} = 13$ TeV", *The European Physical Journal C*, vol. 79, 639, 2019.

[82] ATLAS Collaboration, "Measurement of the muon reconstruction performance of the ATLAS detector using 2011 and 2012 LHC proton–proton collision data", *The European Physical Journal C*, vol. 74, 3130, 2014.

[83] ATLAS Collaboration, "Muon reconstruction performance of the ATLAS detector in proton–proton collision data at $\sqrt{s} = 13$ TeV", *The European Physical Journal C*, vol. 76, 292, 2016.

[84] G. D'Agostini, "A Multidimensional unfolding method based on Bayes' theorem", *Nuclear Instruments and Methods in Physics Research Section A*, vol. 362, p. 487–498, 1995.

[85] S. Schmitt, "Data Unfolding Methods in High Energy Physics", *EPJ Web of Conferences*, vol. 137, 11008, 2017.

[86] F. Spanò, "Unfolding in particle physics: a window on solving inverse problems", *EPJ Web of Conferences*, vol. 55, 03002, 2013.

[87] A. Glazov, "Averaging of DIS Cross Section Data", *AIP Conference Proceedings*, vol. 792, p. 237–240, 2005.

[88] S. Höche, F. Krauss, M. Schönherr, and F. Siegert, "A critical appraisal of NLO+PS matching methods", *Journal of High Energy Physics*, 09, 049, 2012.

[89] S. Höche, F. Krauss, M. Schönherr, and F. Siegert, "QCD matrix elements + parton showers. The NLO case", *Journal of High Energy Physics*, 04, 027, 2013.

[90] S. Catani, F. Krauss, B. R. Webber, and R. Kuhn, "QCD Matrix Elements + Parton Showers", *Journal of High Energy Physics*, 11, 063, 2001.

[91] S. Höche, F. Krauss, S. Schumann, and F. Siegert, "QCD matrix elements and truncated showers", *Journal of High Energy Physics*, 05, 053, 2009.

[92] J. Krause and F. Siegert, "NLO QCD predictions for $Z + \gamma+$ jets production with Sherpa", *The European Physical Journal C*, vol. 78, 161, 2018.

[93] ATLAS Collaboration, "Measurement of the Inelastic Proton–Proton Cross Section at $\sqrt{s} = 13\,\text{TeV}$ with the ATLAS Detector at the LHC", *Physical Review Letters*, vol. 117, 182002, 2016.

[94] ATLAS Collaboration, "Measurements of inclusive and differential fiducial cross-sections of $t\bar{t}\gamma$ production in leptonic final states at $\sqrt{s} = 13$ TeV in ATLAS", *The European Physical Journal C*, vol. 79, 382, 2019.

[95] S. Frixione, "Isolated photons in perturbative QCD", *Physics Letters B*, vol. 429, p. 369–374, 1998.

[96] TOTEM Collaboration, "First measurement of elastic, inelastic and total cross-section at $\sqrt{s} = 13$ TeV by TOTEM and overview of cross-section data at LHC energies", *The European Physical Journal C*, vol. 79, 103, 2019.

[97] J. Butterworth, S. Carrazza, A. Cooper-Sarkar, A. D. Roeck, J. Feltesse, S. Forte, J. Gao, S. Glazov, J. Huston, Z. Kassabov, *et al.*, "PDF4LHC recommendations for LHC Run II", *Journal of Physics G: Nuclear and Particle Physics*, vol. 43, 023001, 2016.

# APPENDIX A

## List of SCT Calibration Defects

The N-point gain defects are defined as follows:

- UNKNOWN
- DEAD - occupancy is always less than 1%
- STUCKON - occupancy is always more than 98%
- UNDER - occupancy never reaches maximum, always less than 95%
- OVER - occupancy greater than 100%
- BADFIT - poor fit to response curve (large $\chi^2$)
- UNBONDED - noise less than 750 ENC
- PARTBONDED - noise less than 1100 ENC
- NOISY - noise greater than 1.15 times the average chip noise
- V_NOISY - noise greater than 1.25 times the average chip noise
- VLO_GAIN - gain lower than 0.3 times the chip average
- LO_GAIN - gain lower than 0.75 times the chip average
- HI_GAIN - gain higher than 1.25 the chip average
- LO_OFFSET - offset lower than -100 mV

- HI_OFFSET - offset higher than 200 mV

The noise occupancy defects are defined as follows:

- NO_HI - noise occupancy greater than 0.05%
- DOUBTR_HI - high double trigger noise occupancy

# APPENDIX B

## $Z\gamma\gamma$ Unfolding Inputs

The inputs to the unfolding, calculated from the Sherpa 2.2.10 NLO signal sample, are given on the following pages. Figures B.1 and B.4 give the reconstruction efficiency correction which accounts for signal events generated in the fiducial phase space which do not pass the detector-level selection, for the electron and muon channels respectively. Figures B.2 and B.5 give the fiducial efficiency correction which accounts for signal events which pass the detector-level selection but fail the fiducial-level selection, for the electron and muon channels respectively. Figures B.3 and B.6 show the fiducial-to-detector-level bin migrations, for the electron and muon channels respectively.

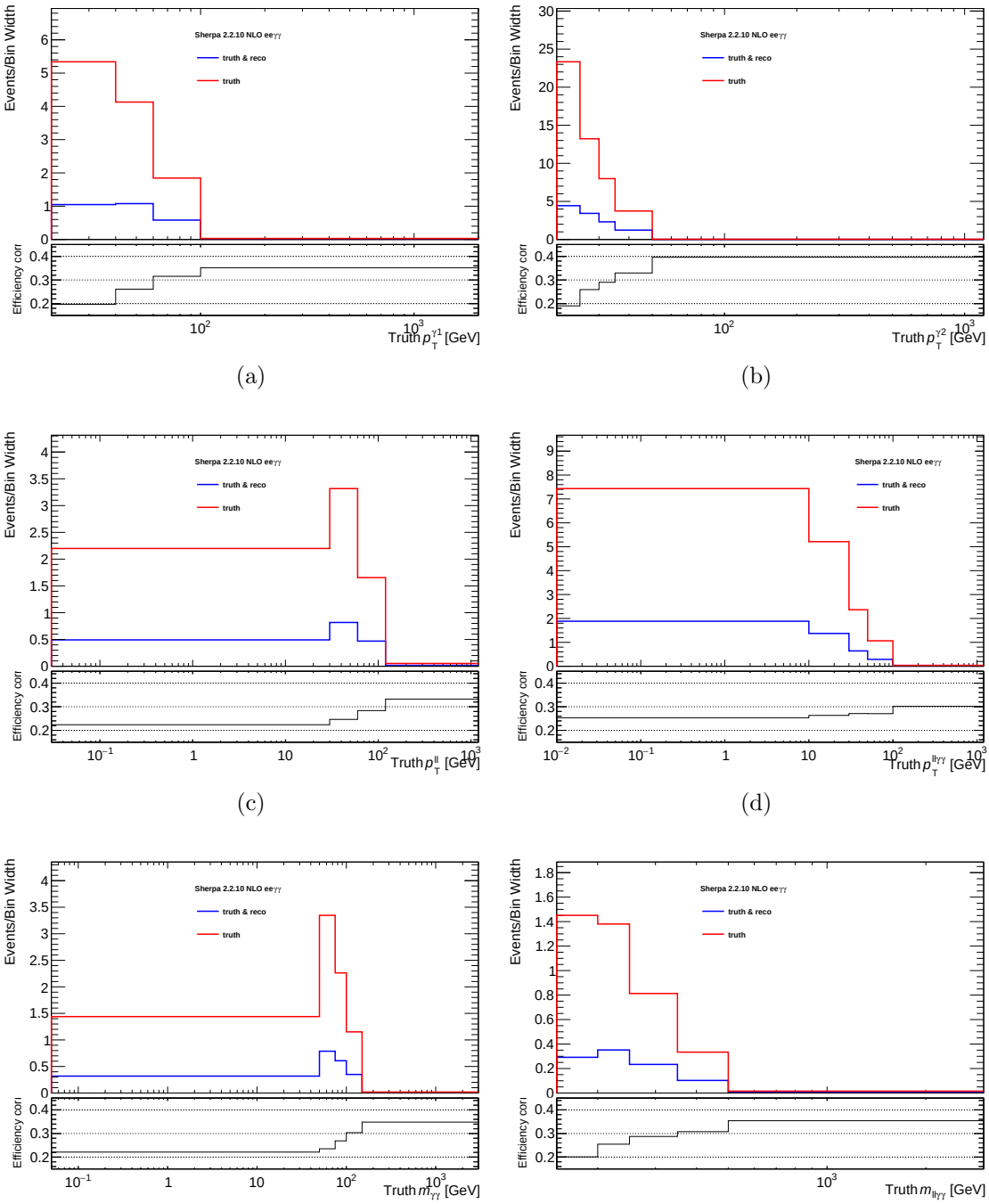


Figure B.1: Efficiency corrections for the $ee\gamma\gamma$ channel.

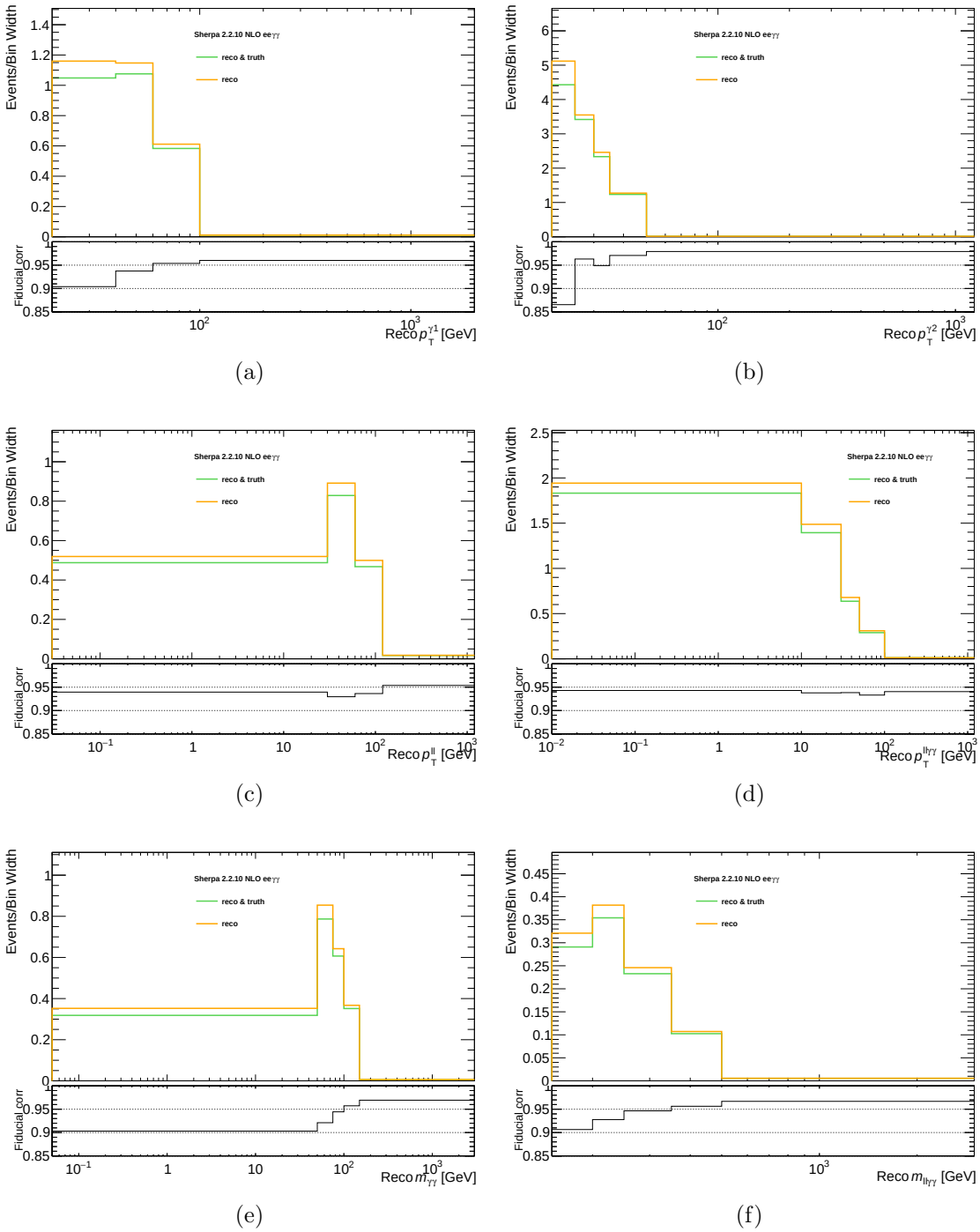


(a) (b)

(c) (d)

(e) (f)

Figure B.2: Fiducial corrections for the $ee\gamma\gamma$ channel.

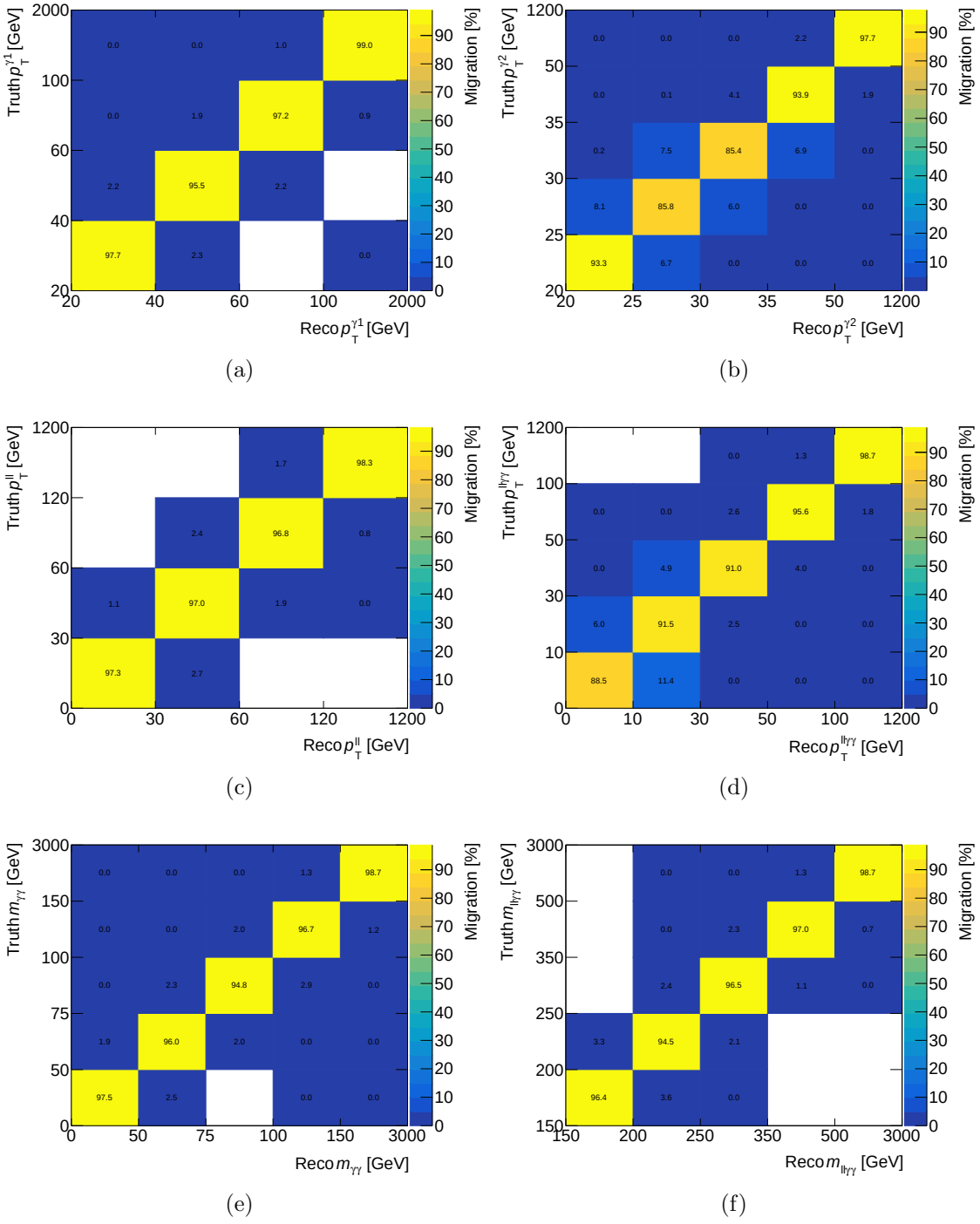


Figure B.3: Migration matrices for the $ee\gamma\gamma$ channel.

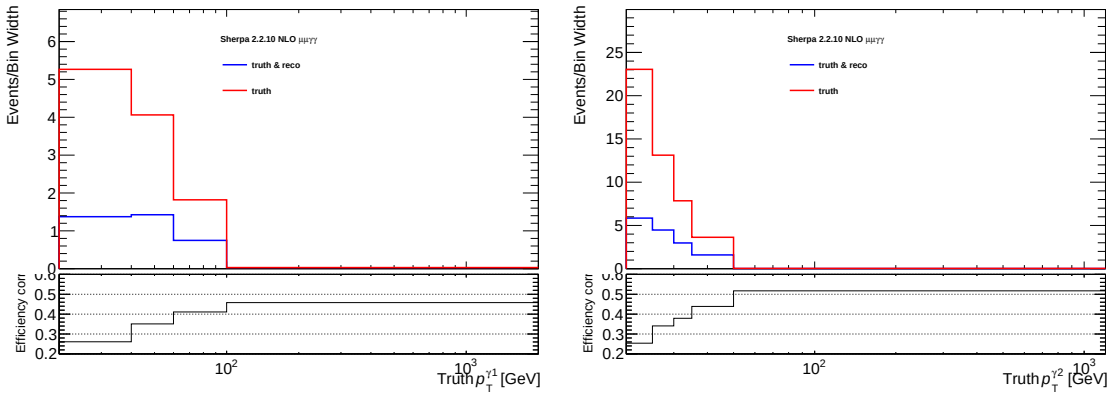


(a)




(b)

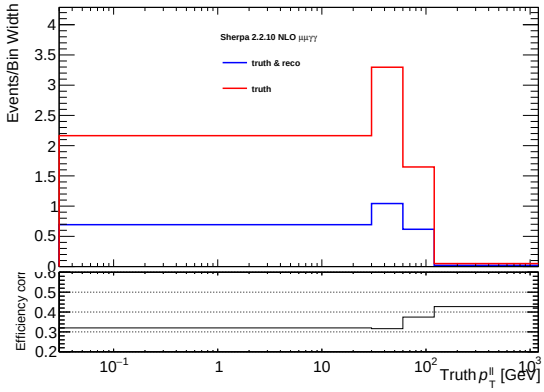


(c)

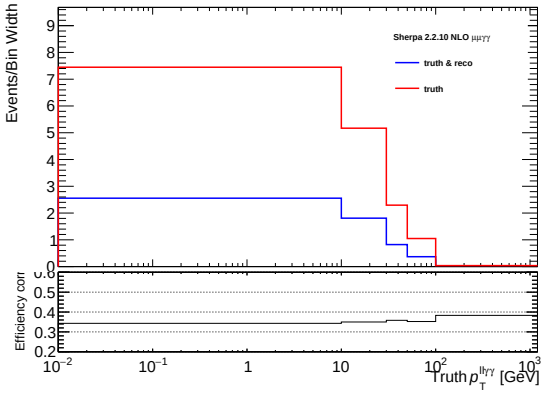


(d)

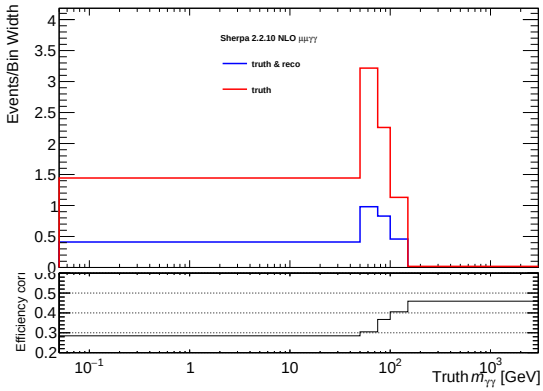


(e)

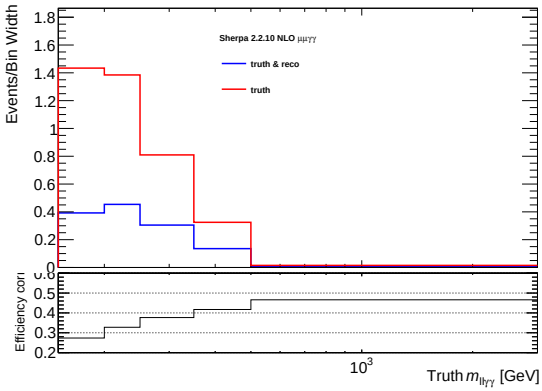


(f)

Figure B.4: Efficiency corrections for the $\mu\mu\gamma\gamma$ channel.

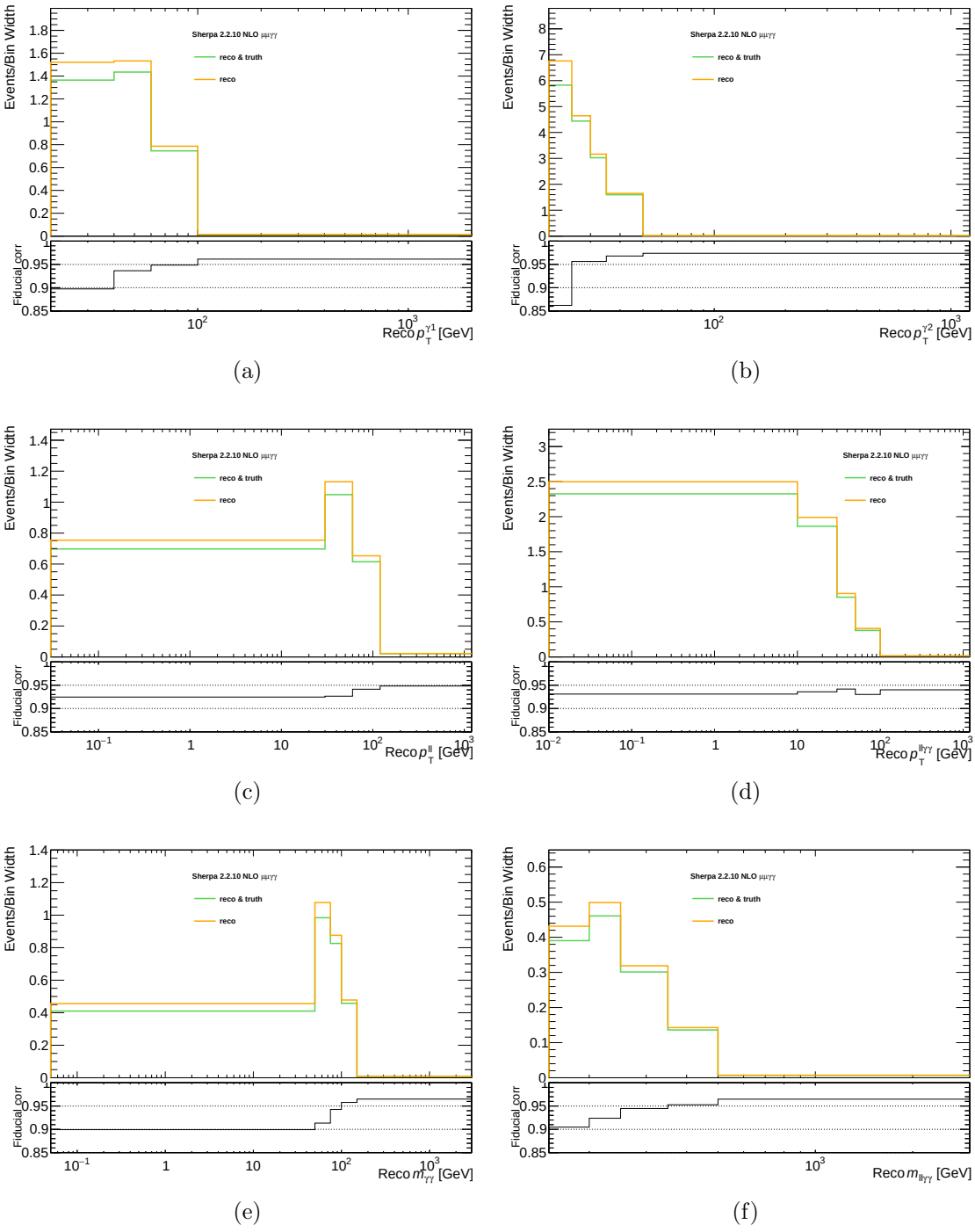


Figure B.5: Fiducial corrections for the $\mu\mu\gamma\gamma$ channel.

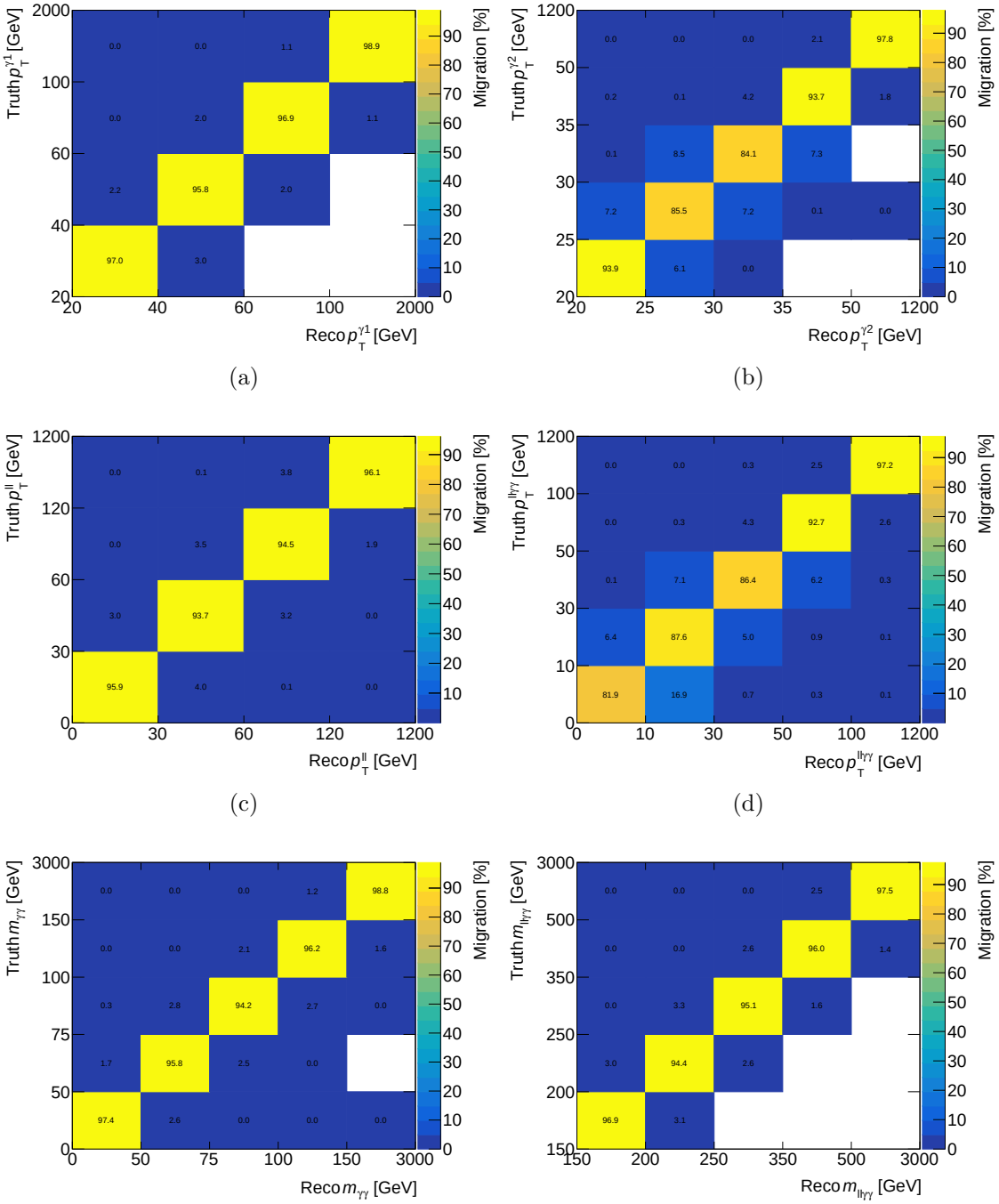


Figure B.6: Migration matrices for the $\mu\mu\gamma\gamma$ channel.